MIXING OF A PASSIVE SCALAR IN ISOTROPIC AND SHEARED HOMOGENEOUS TURBULENCE

by
E. Shirani,
J. H. Ferziger,
and
W. C. Reynolds

Prepared from work done under Grant
NSF-17619

Computational facilities were supplied by
NASA-Ames Research Center

Report No. TF-15

Thermosciences Division
Department of Mechanical Engineering
Stanford University
Stanford, California

May 1981

Inserted
7-30-90
MPP

ERRATA

Report TF-15

Page	
4	Second paragraph, sixth line, insert "and Patterson" after "Schumann."
5	Second paragraph, first line, "Venkataramani" is misspelled.
36	Line 4, change "flows" to "quantities."
38	First paragraph, first line, change "in" to "on."
41	First line, read "... functions of the Reynolds, shear, and Prandtl ..."
45	Eq. (4.57), numerator should be $< u_{i,k} u_{j,k} >$.
77	Last paragraph, first line, insert "the" before "Reynolds."
80	Last paragraph, at end of third line, insert "and Launder (1972)".
81	Second paragraph, eighth line, "parameters" misspelled.
86	Below Eq. (6.29), begin new paragraph with "The values of ..."
87	Second paragraph, line 6, delete "..in Figs. 6-70 to 6-71 and also . . "
154	Reference 20 - last author is "Huang."

MIXING OF A PASSIVE SCALAR IN ISOTROPIC AND SHEARED HOMOGENEOUS TURBULENCE

by

E. Shirani, J. H. Ferziger, and W. C. Reynolds

Prepared from work done under Grant

NSF-17619

Computational facilities were supplied by

NASA-Ames Research Center

Technical Report TF-15

Thermosciences Division
Department of Mechanical Engineering
Stanford University
Stanford, California 94305

May 1981

This Page Intentionally Left Blank

Acknowledgments

The authors gratefully acknowledge the useful comments and discussions of Prof. P. Moin and Drs. W. J. Feiereisen, and A. Cain. Special thanks are due to Dr. R. Rogallo for his suggestions in developing the computer code and for other helpful comments and discussions.

We would like to express our gratitude also to Mr. M. Rubesin and Mr. J. Bardina for their contributions to and discussions of this work and also to Prof. Dean Chapman for his critical reading of the manuscript.

This work was supported by the National Science Foundation under Grant NSF-17619, and computer time was provided by NASA-Ames Research Center under Grant NASA-NCC-2-15. One of the authors (ES-C) acknowledges the support of the Government of Iran during 1976-80.

The authors acknowledge the excellent job of typing done by Ms. Ruth Korb.

Abstract

In order to calculate the velocity and passive scalar fields in homogeneous turbulent flows, the three-dimensional, time-dependent equations of motion and the diffusion equation have been solved numerically. The following cases have been treated:

1. isotropic, homogeneous turbulence with decay of a passive scalar,
2. homogeneous turbulent shear flow with a passive scalar whose mean varies linearly in the spanwise direction.

The solutions have been obtained at relatively low Reynolds numbers so that all of the turbulent scales could be resolved without modeling.

The numerical simulations were carried out on the ILLIAC-IV. The computer program used $16 \times 16 \times 16$, $32 \times 32 \times 32$, or $64 \times 64 \times 64$ uniformly spaced mesh points. The pseudo-spectral method was used for space differencing and the second-order Adams-Bashforth method for time differencing.

Turbulent statistics such as integral length scales, Taylor microscales, Kolmogorov length scale, one- and two-point correlations of velocity-velocity and velocity-scalar, turbulent Prandtl/Schmidt number, r.m.s. values of velocities, the scalar quantity and pressure, skewness, decay rates, and decay exponents have been calculated. Also, one- and three-dimensional spectra of velocity components and scalar quantity, three-dimensional spectra of production, dissipation and transfer terms, pressure, Reynolds stress, and heat flux terms have been calculated. Some of the results are compared with the available experimental results, and good agreement is obtained.

The behavior of the Reynolds stress and the turbulent heat flux have been carefully studied. The conventional models for the turbulent Reynolds stress and heat flux, turbulent Prandtl number, and pressure-strain and pressure-scalar covariances have been tested, and constants for the models have been obtained.

Table of Contents

List of Figures

List of Tables

Nomenclature

English Letters

A_o Model constant, Eqs. (4-69) through (4-71).

A_1 Model constant, Eqs. (4-49) and (4-78).

A_2 Model constant, Eqs. (4-55) and (4-78).

A_3 Model constant, Eq. (4-56).

b_{ij} Reynolds stress anisotropy tensor, Eq. (4-23).

B_{ij} Tensor similar to b_{ij} for the scalar field, Eq. (4-77).

C Mean scalar quantity.

C Model constant, Eqs. (4-23), (6-11), and (6-18).

C_o Model constant, Eq. (2-2).

C_1 Model constant, Eqs. (4-25), (4-35), and (4-37)-(4-39).

C_2 Model constant, Eqs. (4-35) and (4-38)-(4-39).

C_3 Model constant, Eqs. (4-35) and (4-38)-(4-40).

C_4 Model constant, Eqs. (4-37) and (4-40).

D Molecular diffusion coefficient.

D_{ij} Turbulent diffusion coefficient tensor, Eq. (4-26).

d_{ij} Dissipation anisotropy tensor, Eq. (4-57).

E(k) Three-dimensional energy spectra.

$E_{ij}(k_\ell)$ One-dimensional spectrum in ℓ-direction.

$E_{\theta\theta}(k_\ell)$ One-dimensional spectrum of the scalar in ℓ-direction.

e Turbulent kinetic energy.

G Part of Poisson equation, Eq. (2-22).

G_{ijpq} Fourth-rank tensor, Eq. (4-48).

g_{qij} Third-rank tensor, Eq. (4-66).

H_i Part of right-hand side of the momentum equation, Eq. (2-21).

h Height of the experimental channel.

h	Mesh size.
k	Wave number, $k^2 = k_i k_i$.
k_i	Components of the wave vector.
L	Integral length scale obtained from $R_{11}(x_1)$.
L_b	Length of the computational box.
L_d	Dissipation length scale, Eq. (4-24).
$L_{ij}(r_\ell)$	Length scales in ℓ-direction.
L_m	Mixing length, Eq. (6-6).
L_{tr}	Transfer length scale ($\equiv q^3/\varepsilon$).
m	Decay exponent of scalar intensity, Eq. (5-4).
N	Number of mesh points in each direction.
N_c	Courant number, Eq. (A-20).
N_D	Diffusion stability parameter, Eq. (A-19).
N_ν	Viscous stability parameter, Eq. (A-18).
n	Number of time steps.
P	Total pressure.
p	Pressure fluctuations.
$p^{(1)}$	Part of pressure which is explicitly associated with the mean velocity, Eq. (4-42).
$p^{(2)}$	Part of pressure which is not explicitly associated with the mean velocity, Eq. (4-43).
Pe_T	Turbulent Peclet number, Eq. (4-39).
Pr	Molecular Prandtl number.
Pr_T	Turbulent Prandtl number, Eq. (4-36).
q	Turbulent velocity, Eq. (4-20).
R	Decay exponent ratio, Eq. (5-5).
Re_L	Turbulent Reynolds number based on q and L_d, Eq. (2-3).
Re_M	Reynolds number based on mean velocity and mesh size.

Re_λ Turbulent Reynolds number based on λ and q $\left(\equiv \frac{q\lambda}{\nu}\right)$.

$R_{ij}(r_\ell)$ Two-point correlations, Eq. (3-3).

$R_{\theta\theta}(r_\ell)$ Two-point correlatins of the scalar fluctuations.

R_l A parameter which indicates degree of numerical stability and accuracy, Eq. (A-12).

R_L A parameter which indicates degree of numerical stability and accuracy, Eq. (A-12).

S Shear rate $\left(\equiv \frac{\partial \overline{U}_1}{\partial x_2}\right)$.

S_i Mean scalar gradient $\left(\equiv \frac{\partial \overline{C}}{\partial x_i}\right)$.

S_{ij} Mean strain, Eq. (4-19).

S_k Velocity skewness, Eq. (3-2).

$\mathscr{S}$ Shear number $\left(\equiv \frac{SL}{q}\right)$.

$\mathscr{S}_{\theta i}$ Nondimensional scalar fluctuations $\left(\equiv \frac{\theta'}{S_2 L}\right)$.

T, t Time

T_{ij} Transfer term, Eq. (6-9).

U_i Total velocity in i-direction.

$\overline{U}_i$ Mean velocity in i-direction.

u_i Velocity fluctuations in i-direction.

u_i' r.m.s. u_i $\left(\equiv < u_i^2 >^{1/2}\right)$.

$U_i^{(R)}$ Random-generated velocity components, Eq. (2-13).

X_i Laboratory coordinate in the i-direction.

x_i Computational (sheared) coordinate the in i-direction.

Greek Letters

α The exponent of Reynolds number in the fitting function, Eqs. (6-11) and (6-18).

α Model constant, Eq. (4-39).

α_i Angle of the principal axis, Eq. (4-17).

β The exponent of the shear number in the fitting function, Eqs. (6-11) and (6-18).

Δt Time step.

δ_{ij} Kronecker delta $\equiv \begin{cases} 1 , & i = j, \\ 0 , & i \neq j. \end{cases}$

ϵ Dissipation of turbulent kinetic energy, Eq. (4-58).

ϵ_i Dissipation of turbulent heat flux, Eq. (4-14).

ϵ_{ij} Dissipation of the Reynolds stress tensor, Eq. (4-7).

ϵ_θ Dissipation of scalar fluctuations, Eq. (5-7).

η Kolmogorov length scale, Eq. (2-1).

γ The exponent of Prandtl number in the fitting function, Eq. (6-18).

λ Taylor microscale for the velocity field $\equiv \lambda_{11}(x_1)$.

$\lambda_{ij}(x_\ell)$ Taylor microscale for the velocity field in x_ℓ-direction.

λ_u Taylor microscale for the velocity field $\equiv \lambda_{11}(x_1)$.

λ_θ Taylor microscale for the scalar field in the x_1-direction.

ν Molecular viscosity.

ν_T Turbulent eddy viscosity, Eq. (4-21).

Ω_{ij} Mean rotation, Eq. (4-34).

σ_i Magnitude of the principal stresses.

θ Scalar fluctuations.

θ' r.m.s. scalar fluctuations $\left(\equiv < \theta^2 >^{1/2}\right)$.

ϕ Potential function, Eq. (2-13).

ϕ_i Pressure-scalar covariance, Eq. (4-13).

ϕ_{ij} Pressure-strain, Eq. (4-6).

ψ_{ij} Function of pressure-scalar covariance, Eq. (4-76).

Other Symbols

$\langle\ \rangle$ Volume average.

$(')$ Root mean square value (r.m.s.).

$(\hat{\ })$ Fourier transfer

$(\vec{\ })$ Vector.

$(\bar{\ })$ Mean value (ensembled average).

Chapter I

INTRODUCTION

1.1 General Background

For a century, turbulence has been the subject of intensive research, both theoretically and experimentally. Due to its complexity and despite strong efforts, turbulence remains one of the most challenging unsolved problems of the physical sciences. History suggests that the road to the general solution of the problem is very long, if not endless.

Turbulence originates in instabilities of laminar flow. Generally, the instabilities produce wave-like structures which can absorb energy from the mean flow. As they grow, nonlinear effects cause energy transfer to other modes, and eventually the noisy patterns that are generally regarded as "turbulence" results. Energy obtained from the mean flow is eventually transferred to smaller-scale structures, where it will be dissipated.

Turbulence contains structures with a wide range of scales. The large-scale turbulent structures differ markedly from one flow type to another, while the small scales tend to be more universal. Since neither experimentalists nor computors have been able to resolve all of the turbulent structures for high Reynolds number flows, approximations have had to be made.

Almost all approaches to the prediction of turbulent flows are based on Osborne Reynolds' idea of averaging the Navier-Stokes equations over an ensemble of identical flows, or some equivalent (time or span averaging) to obtain equations for the mean velocities. Due to the nonlinearity of the Navier-Stokes equations, the averaged equations are not closed. Therefore, turbulence models are needed to bridge the gap between the difficulty of the equations and our limited computational capability to handle the equations.

Turbulence modeling has made considerable strides in the past two decades. The testing of the models has, until recently, been a highly empirical affair. It is currently impossible to measure all of the

factors needed to test the models experimentally. However, it is possible to use exact numerical solutions of the equations of motion for turbulent flows as the basis for testing models. The difficulty here is that, with the available computers, one can compute only relatively low Reynolds number flows. In addition, only a few simple turbulent flows can be computed with sufficient accuracy. Due to the large range of scales of turbulent structures, we cannot expect to compute high Reynolds number turbulent flows directly with the next few generations of computers. Despite these limitations, one might compute relatively simple flows at moderate Reynolds numbers and extrapolate the results to higher Reynolds numbers.

The simplest type of turbulence is homogeneous isotropic turbulence. This is defined as a flow whose statistical features have no preference for any specific direction or location. Thus a minimum number of quantities and relations are required to describe its structure and behavior. Although it is an idealized flow, its characteristics form a basis for the study of more complex non-isotropic turbulent flows. Moreover, in actual turbulent flows at high Reynolds numbers, the fine structures seem to be nearly isotropic, so the results of isotropic turbulence may be useful for characterizing the small scales of turbulence. Because of its simplicity and importance, extensive theoretical work has been done on this subject and a number of experiments have been carried out.

A somewhat more complex type of turbulent flow is homogeneous shear flow. The role of shear in most turbulent flows is to couple the mean velocity field with the turbulent velocity field. Homogeneous shear flow is a problem of complexity intermediate between unsheared homogeneous and inhomogeneous turbulent shear flows. It has been generated both experimentally and computationally. Its study can provide better understanding of turbulence and can be used in testing the validity of turbulence theories and statistical turbulence models.

It is useful to consider the case in which a scalar quantity is present in a turbulent flow. The scalar may be temperature or enthalpy, or, in a mixture of fluids, species concentration. The study of the scalar field has attracted less attention than the study of the

hydrodynamics itself. However, the investigation of turbulent mixing is an area of great importance. It is required in any situation that includes mass or heat transfer, for example, in the atmosphere. Turbulent mixing is also important in reacting flows and combustion. Prediction of most turbulent reacting and combusting flows is essentially impossible without accurate treatment of mixing. Study of a passive scalar in turbulent flows will help us understand the turbulent mixing processes that occur in these flows.

One of the objectives of the present report is to compute three-dimensional, time-dependent solutions for isotropic turbulence and homogeneous shear turbulent flows by numerical methods, and to study the scalar field as well as the velocity field. The results will be used in a number of ways.

1.2 Survey of Literature

The mathematical development of hydrodynamics was started in the eighteenth century. The dynamic equations for inviscid flows were formulated mainly by Euler (1752). The equations of motion for a viscous flow were derived by Navier (1827), Poisson (1831), Saint-Venant (1843), and Stokes (1845). O. Reynolds (1883) introduced the non-dimensional Reynolds number and used it as a criterion to distinguish laminar flows from turbulent flows. Boussinesq (1877) introduced the concept of eddy viscosity. Mixing-length theory was introduced by Prandtl (1925) and von Karman (1930).

A. Homogeneous Isotropic Turbulence

The concept of isotropic turbulence was introduced by Taylor (1935). Von Karman (1937) introduced the use of tensors in isotropic turbulence, while von Karman and Howarth (1938) studied the statistical theory of turbulence. In 1941, Kolmogoroff suggested that the small-scale components of turbulence are approximately isotropic, while Batchelor and Stewart (1949) showed that large scales of the turbulence generated behind a grid are anisotropic.

Almost all experiments on isotropic turbulence use rigid, uniform grids to generate the turbulence. The first successful attempt to

generate nearly isotropic turbulence was that of Simmon and Salter (1934). They found that at high Reynolds numbers the turbulence far behind a grid is a good laboratory realization of isotropic turbulence. Several other experiments have been carried out for this case, among which that of Comte-Bellot and Corrsin (1971) provides rather complete statistical information. Frenkiel, Klebanoff, and Huang (1979) carried out the experiment in both water and air.

The final stage of isotropic turbulence was studied experimentally by Batchelor and Townsend (1950), Tan and Ling (1963), Lee (1965), and Bennett and Corrsin (1978). Also Tavoularis, Bennett, and Corrsin (1979) studied the velocity skewness of isotropic turbulence at small Reynolds numbers.

Isotropic homogeneous turbulence has been studied by computors. Numerical simulation of the decay of two-dimensional, isotropic, homogeneous turbulent flows was carried out by Herring, Orszag, Kraichnan, and Fox (1974), and turbulence theories were tested. The first simulation of three-dimensional, homogeneous, isotropic turbulence was made by Orszag and Patterson (1971). Schumann and Patterson (1975) also simulated isotropic turbulence numerically and studied the velocity and pressure fluctuations. Three-dimensional, homogeneous, isotropic, incompressible turbulence has been studied at Stanford University using the large eddy simulation technique. Kwak, Reynolds, and Ferziger (1975), and Shaanan, Ferziger, and Reynolds (1975) simulated isotropic turbulence and obtained very good agreement with the experimental results of Comte-Bellot and Corrsin. Clark, Ferziger, and Reynolds (1977) carried out a direct calculation for the isotropic, homogeneous turbulent flows at low Reynolds number and used it to study subgrid scale modeling.

There is also a series of experiments in heated isotropic turbulence. In all cases the heating was small enough that the temperature could be assumed a passive scalar and density variations neglected. The diffusion of heat from a fixed line source in grid-generated, nearly isotropic turbulence was studied experimentally by Schubauer (1935), Collis (1948), Frenkiel (1950), Townsend (1951), Uberoi and Corrsin (1952), Shlien and Corrsin (1974), and Libby (1975). These experiments studied the downstream development of temperature fluctuations and

measured statistical properties such as length scales, decay rates, velocity-velocity and velocity-temperature correlations, and spectra.

The fluctuating temperature field in isotropic turbulence generated by uniformly heated grids was studied by Kistler, O'Brien, and Corrsin (1956), Mills and Corrsin (1959), Yeh and van Atta (1973), Sepri (1976), and Warhaft and Lumley (1979). They have presented various correlations, length scales, and spectra of the scalar and velocity fields. Table 1-1 summarizes the basic parameters of the above experiments. Yeh et al. (1974) carried out their experiment at relatively low Reynolds number and studied the spectral transfer of the scalar and velocity fields. Table 1-1 shows that, unlike the decay exponent of the turbulent kinetic energy, the decay exponent of the fluctuating scalar intensity varies considerably from one experiment to another. Domis (1979) simulated the flow by large eddy simulation and studied the effects of the initial length scales on the decay exponent of the scalar. He concluded that the decay exponent of the scalar is a linear function of the initial length scale ratio. We shall study the effects of Reynolds number and Prandtl number on the decay exponents.

Non-uniformly heated grids were used by Wiskind (1962) and ~~Venkataramani~~ Venkataramani and Chevray (1978) to generate a uniform temperature gradient in isotropic turbulence. Measurements of probability and joint probability densities of velocity and temperature as well as spectra and the other turbulence statistics were obtained in the latter experiment. Cornelius and Foss (1978) measured the diffusion of particles in isotropic turbulence by a unique method.

B. Homogeneous Shear Flows

Reis (1952) studied homogeneous shear flows mathematically. Rose (1966) experimentally generated this flow and studied the behavior of the turbulence intensities. Champagne, Harris, and Corrsin (CHC) (1970), Harris, Graham, and Corrsin (HGC) (1976), Rose (1970), Hwang (1971), and Mulhearn and Luxton (1975) studied this flow at higher Reynolds numbers. These experiments measured the shear stress correlations, various length scales, one- and two-point velocity correlations, spectra, and the kinetic energy of turbulence. Table 1-2 summarizes

some of the basic parameters of these flows. Rose's experiment was carried out at lower Reynolds number and the Harris et al. experiment at higher shear rate.

Numerical simulations of homogeneous shear flows were made by Shannan, Ferziger, and Reynolds (1975) using large eddy simulation. Later, R. S. Rogallo (1977) made direct simulations of Reynolds number homogeneous turbulent shear flows. Similar calculations were done for the compressible case by Feiereisen, Reynolds, and Ferziger (1981).

Temperature as a passive scalar in homogeneous shear flows was studied by Tavoularis (1978). He generated a turbulent homogeneous shear flow with a uniform mean temperature gradient and studied the statistics of the scalar field, as well as the velocity field. The basic parameters of this experiment are similar to those of the Harris et al. experiment and are shown in Table 1-2. He used air (Prandtl number 0.7) and the mean-temperature gradient was 9.5 C/m. We shall compare our computed scalar field results with this experiment. Fox (1964) simulated the heat transfer in a two-dimensional, homogeneous shear flow numerically, and studied the effect of molecular Prandtl number on the turbulent heat flux and the turbulent Prandtl number.

1.3 Motivations and Objectives

Homogeneous shear flow is a flow of complexity between that of unsheared isotropic homogeneous turbulence and inhomogeneous shear flows. Although simple (it does not contain rigid boundaries, laminar-turbulent interfaces, or other inhomogeneities), it retains many basic features of sheared turbulence, such as production of turbulent kinetic energy from mean shear and non-zero Reynolds shear stress. This flow has been generated experimentally by several investigators mentioned in the previous section. From this flow, many turbulent statistics can be calculated and turbulence theories and models tested.

The investigation of mixing of a scalar in turbulent flows is of great importance. Turbulent mixing occurs in any flow which includes mass or heat transfer. There are many applications in meteorology and oceanography, as well as engineering. The last includes reacting flows as well as flows in which heat transfer is important.

We shall study mixing of a passive scalar in homogeneous turbulent shear flows and compare the scalar field with the velocity field. This helps us to understand some basic phenomena of turbulence. By means of analogy between the velocity field and the scalar field, we shall study various aspects of turbulent mixing. We shall also test some turbulence models.

Our specific objectives are these:

1. To compute the mixing of a passive scalar in isotropic turbulent flow at relatively low Reynolds number by solving the Navier-Stokes and concentration equations numerically. We shall calculate r.m.s. values of velocity components and the scalar quantity, various length scales, spectra, and the decay exponent ratio between the scalar field and the velocity field. We shall study the effects of the Reynolds and Prandtl numbers on the decay rate of turbulent kinetic energy and the r.m.s. value of the scalar quantity. All of these results will be compared with experiment.

2. To compute the behavior of a passive scalar in a turbulent homogeneous shear flow, with uniform scalar gradient. In this flow we shall calculate one- and two-point correlations, turbulent Prandtl/Schmidt number, r.m.s. values of velocity, scalar, and pressure, skewness, various length scales, and spectra. We shall study the effects of Reynolds number, Prandtl number, and shear number (a non-dimensional shear rate) on the turbulence statistics. We shall present correlations for many of the turbulence statistics. Special attention will be given to the turbulent Reynolds stresses and the turbulent heat flux. Finally, energy and heat transfer between the various sizes of eddies will be discussed by calculating the spectra of the transfer terms.

3. To test various models for heat/mass flux, Reynolds stress, pressure-strain and pressure-scalar covariences. The validity of the models as well as the constants for each models will be studied.

Table 1-1

Descriptions and Results of Various Experiments and Numerical Simulations on Decay of Temperature Fluctuations in Grid-Generated Homogeneous Isotropic Flows

	Re_λ*	Re_M**	Pr	n	m	λ_u/λ_θ
Yeh & Van Atta (1973)	60.97	10550	0.725	1.37	1.33	0.718
Sepri (1976)	60.62	10484	0.72	1.39	1.4	?
Warhaft and Lumley (1978)	130	10000	0.72	1.34	.858-1.407	.216-0.316
Domis (1979)	80.97	10550	0.72	0.885	0.91-2.03	0.71-0.93

*Re_λ is the Reynolds number based on the Taylor microscale and turbulent velocity.

**Re_M is the Reynolds number based on the mesh size and streamwise velocity.

Table 1-2

Description of Various Experiments
on Homogeneous Shear Flows

Experiment	Shear Rate S (sec^{-1})	Reynolds No. Re_λ*	Shear No. $\mathcal{S}$**	Total Shear St
Rose (1966)	13.68	133.0	9.53	3.2
Champagne et al. (1970)	12.90	204.8	7.79	3.2
Harris et al. (1977)	44.0	396.4	8.28	10.81
Tavoularis (1979)	46.8	397.9	14.76	12.65

*The values of Re_λ and $\mathcal{S}$ are given at $x_1/h = 7.5$ for Rose and Harris et al., at $x_1/h = 8.5$ for Champagne et al., and at $x_1/h = 11$ for Tavoularis.

**The shear number is defined as $\mathcal{S} = SL/q$, where L is integral length scale and $q = \langle u_i u_i \rangle^{1/2}$.

Chapter II

COMPUTATIONAL METHODS

One of the major difficulties in numerical calculations of turbulent flows is the wide range of length scales in the flow. To capture the large scales of turbulence, the computational box has to be bigger than the largest scale. On the other hand, to resolve the smallest scale of turbulence in a grid-based calculation, the mesh size has to be smaller than the smallest length scale, which is the Kolmogoroff microscale defined as:

$$\eta = \left(\nu^3/\varepsilon\right)^{1/4} \tag{2-1}$$

where ν is the kinematic viscosity and ε is the dissipation rate, i.e., the rate of destruction of turbulent kinetic energy by viscosity. The dissipation is also related to the large scale by the relation:

$$\varepsilon = C_o q^3/L_d \tag{2-2}$$

where q is the r.m.s. velocity $(q^2 = < u_1^2 > + < u_2^2 > + < u_3^2 >)$, L_d is a large eddy length scale, and C_o is a proportionality constant.

One can find the number of mesh points required to resolve both the large and small scales in a three-dimensional computation by combining the above relations. The number of mesh points required for accurate resolution is approximately

$$\left(\frac{L_d}{\eta}\right)^3 = \left(\frac{qL_d}{\nu}\right)^{9/4} = Re_L^{9/4} \tag{2-3}$$

and depends strongly on Reynolds number. Since, from a practical point of view, the number of mesh points is limited by the computational speed and size of the computer memory, computations are currently limited to low turbulent Reynolds numbers. In our case, with 64^3 cubed mesh points, the Reynolds number has to be less than about 100.

2.1 Governing Equations

The equations of motion for an incompressible fluid are:

$$\frac{\partial U_i}{\partial T} = -\frac{\partial U_i U_j}{\partial X_j} - \frac{\partial P}{\partial X_i} + \nu \frac{\partial^2 U_i}{\partial X_j \partial X_j} \tag{2-4}$$

$$\frac{\partial U_i}{\partial X_i} = 0 \tag{2-5}$$

$$\frac{\partial C}{\partial T} = -\frac{\partial C U_i}{\partial X_i} + D \frac{\partial^2 C}{\partial X_j X_j} \tag{2-6}$$

where U, P, ν, C, and D are velocity, ratio of pressure to density, kinematic viscosity, scalar concentration, and diffusion coefficient, respectively. The summation convention is implied. Note that the scalar quantity can be temperature or concentration of a species.

Instead of satisfying the incompressible continuity equation, we use the Poisson equation. This equation is derived by taking the divergence of Eq. (2-4) and using Eq. (2-5) to eliminate some of the terms. The result is

$$\nabla^2 P = -\frac{\partial^2 U_i U_j}{\partial X_i \partial X_j} \tag{2-7}$$

2.2 Numerical Approximations

The governing equations given above do not have analytical solutions for turbulent flows, and numerical approximations must be made. Since the data will be discretized onto mesh points, we must approximate partial derivatives in terms of the data at these points. We use the pseudo-spectral method for this purpose. This method, which is good for problems with periodic boundary conditions, has been analyzed by Lanczos (1956) and has been proposed by Orszag and Patterson (1971) and Kreiss and Oliger (1973) as an approximation method and used by many computors since then. Mansour et al. (1977) used the pseudo-spectral method and compared it with some second-order and fourth-order finite-difference schemes. They showed that use of the pseudo-spectral method improved accuracy considerably. The method is briefly explained below.

Suppose a function of one variable $F(X)$ is periodic with period L. For equally spaced mesh points such a function can be approximated at the mesh points as follows:

$$F(X_j) = \sum_{n=-N/2}^{N/2-1} \hat{F}(k_n)\, e^{ik_n X_j} \qquad (2\text{-}8)$$

where

N = number of mesh points,

$X_j = hj$, $j = 0, 1, 2, 3, \ldots , N-1$,

h = mesh size,

$k_n = \frac{2\pi}{Nh} n$, $n = -\frac{N}{2} \ldots , 0 , \ldots , \frac{N}{2} - 1$, and

$$\hat{F}(k_n) = \frac{1}{N} \sum_j F(X_j)\, e^{-ik_n X_j} \qquad (2\text{-}9)$$

To compute $\hat{F}(k)$, we use the Fast Fourier Transform (FFT), originally developed by Cooley and Tukey (1963). This algorithm is good for $N = 2^n$, where n is an integer (see, for example, Bracewell (1965). Newer methods are efficient for other numbers of points but are not needed for our purposes.

If we regard the expansion (2-8) as an interpolation formula and replace X_j by a continuous variable X, the derivative of $F(X)$ with respect to X can be approximated by

$$\frac{dF(X)}{dX} = \sum_n \hat{F}(k_n)\, ik_n\, e^{ik_n X} \qquad (2\text{-}10)$$

Therefore, to compute $dF(X)/dX$, we calculate the Fourier transform of $F(X)$, multiply it by ik, and take its inverse Fourier transform.

To advance in time, a second-order Adams-Bashforth (AB) method was used. It has been shown by Billy (1965) that this method is weakly unstable, but its spurious computational production of kinetic energy is small. A fourth-order Runge-Kutta method would be more stable; however, it is more expensive and requires larger computer memory.

The AB method of advancing the solution of $\partial U/\partial t = H$ from the time step n to time step $n+1$ is

$$U^{n+1} = U^n + \frac{1}{2}\Delta t(3H^n - H^{n-1}) \qquad (2\text{-}11)$$

where Δt is the time step.

As we see, it is a two-step explicit method and needs a starting method; we use the Euler method to start the calculation. The Euler formula is

$$U^{n+1} = U^n + \Delta t H^n \qquad (2\text{-}12)$$

2.3 Initial Conditions

We start with an initial velocity field that is randomly chosen, but which satisfies continuity and has a given three-dimensional spectrum. To obtain such an initial field, we first use computer-generated random numbers for each component of velocity at each mesh point, $U_i^{(R)}$. To this we add the gradient of a potential which will be chosen to make the field divergence-free:

$$U_i^{(S)} = U_i^{(R)} + \frac{\partial \phi}{\partial X_i} \qquad (2\text{-}13)$$

To make $U_i^{(S)}$ divergence-free, we take the divergence of the above equation and set $\partial U_i^{(S)}/\partial X_i = 0$ to find

$$\frac{\partial^2 \phi}{\partial X_i \partial X_i} = -\frac{\partial U_i^{(R)}}{\partial X_i} \qquad (2\text{-}14)$$

This is a Poisson equation for the potential and is solved by a Fourier transform method. The Fourier transform of Eq. (2-14) is:

$$k^2 \hat{\phi} = -ik_i \hat{U}_i^{(R)} \qquad (2\text{-}15)$$

From this equation, we calculate $\hat{\phi}$, invert the Fourier transform to get ϕ, and substitute into Eq. (2-13) to get the desired divergence-free field.

Now we take the Fourier transform of the resulting field and multiply each mode by a factor such that the desired three-dimensional

spectrum is obtained. The resulting field is nearly isotropic, divergence-free, and has the desired spectrum.

We use a similar procedure to calculate the initial scalar field. We start with a field of random numbers and take its Fourier transform. Then we multiply each mode by a factor which yields the desired spectrum for the passive scalar.

The initial three-dimensional spectra of the velocity and scalar fields are step functions. The width, location, and height of the spectra determine the initial Taylor microscales, integral length scale, and the r.m.s. values of turbulent velocity components and scalar concentration. All the initial values are non-dimensionalized (the computational box length is 2π) and must be scaled to obtain the dimensional values. The problem contains three dimensional units: length, time, and temperature (or mass in the case where the scalar is concentration). To dimensionalize the results, we need a length, a time, and a temperature or mass, or three independent combinations of these parameters.

2.4 Computation of Homogeneous Isotropic Turbulent Flows with Decay of a Passive Scalar

In this section we consider a method of computation for simulating a grid-generated isotropic homogeneous flow. The computational box is shown in Fig. 2-1.

The governing equations for this case are Eqs. (2-4), (2-6), and (2-7). The mean values of velocity, pressure, and scalar quantity are set to zero. The initial spectra of velocity and the scalar are given in Fig. 2-2. For all cases we use $32 \times 32 \times 32$ equally spaced mesh points. The accuracy and stability of the numerical method are discussed in Appendix A and will be explained later in Section 3D of this chapter.

The computing time per time step is approximately 3.2 seconds of CPU time on the ILLIAC IV.

2.5 Computation of Homogeneous Turbulent Shear Flow with Decay of a Passive Scalar

In this section we derive governing equations numerically to simulate turbulent homogeneous shear flow with a passive scalar. We also describe the computational details.

A. Mean Values of Velocities and Scalar Quantity

In homogeneous flows, the mean values of the velocity components and scalar concentration may vary with time and/or space. We are interested in mixing a passive scalar in a homogeneous shear flow with the following mean values of velocity, pressure, and concentration:

$$\begin{aligned} \overline{U_1} &= SX_2 \\ \overline{U_2} &= 0 \\ \overline{U_3} &= 0 \\ \overline{P} &= 0 \\ \overline{C} &= S_2X_2 \end{aligned} \tag{2-16}$$

where an overbar denotes an ensemble average and S and S_2 are shear rate and mean concentration gradient, respectively. The mean values, as shown above, remain unchanged throughout the simulation.

The fluctuating quantities are defined as follows:

$$\begin{aligned} u &= U - \overline{U} \\ v &= V - \overline{V} \\ w &= W - \overline{W} \end{aligned} \tag{2-17}$$

or

$$\begin{aligned} u_i &= U_i - \overline{U_i} \\ p &= P - \overline{P} \end{aligned}$$

and (2-18)

$$\theta = C - \overline{C}$$

B. Coordinate Transformations

If we substitute Eqs. (2-15) and (2-16) into Eqs. (2-4), (2-5), and (2-6), we get the set of equations

$$\frac{\partial u_i}{\partial X_i} = 0$$

$$\frac{\partial u_i}{\partial t} = -\frac{\partial u_i u_j}{\partial X_j} - SX_2 \frac{\partial u_i}{\partial X_1} - Su_2\delta_{ij} - \frac{\partial p}{\partial X_i} + \nu \frac{\partial^2 u_i}{\partial X_j \partial X_j} \qquad (2\text{-}19)$$

$$\frac{\partial \theta}{\partial t} = -\frac{\partial \theta u_j}{\partial X_j} - SX_2 \frac{\partial \theta}{\partial X_1} - S_2 u_2 + D \frac{\partial^2 \theta}{\partial X_j \partial X_j}$$

Periodic boundary conditions cannot be applied to these equations. They are prohibited by the presence of SX_2 as a coefficient in one term of each of the last two equations. These terms are different at the top and bottom of the computational box, and application of periodic boundary conditions to them would result in numerical errors similar to the Gibbs phenomenon at these two boundaries. We therefore introduce a coordinate transformation which eliminates the non-periodic terms. The new coordinates are

$$\begin{aligned} x_1 &= X_1 - SX_2 t \\ x_2 &= X_2 \\ x_3 &= X_3 \end{aligned} \qquad (2\text{-}20)$$

The new coordinate system moves with the mean flow, as shown in Fig. 2-3.

Transforming the equations to the new coordinate is a little complicated and is done by using the chain rule. Details are given in Appendix B. The resulting equations will be given below.

C. The Governing Equations

The governing equations are obtained by applying the transformation (2-20) to equations (2-19). The transformed continuity equation is

$$u_{i,i} - St\, u_{2,1} = 0 \qquad (2\text{-}21)$$

The momentum equations become

$$\frac{\partial u_i}{\partial t} = -(u_i u_j)_{,j} + St\, u_i u_2 - S u_2 \delta_{i1} - p_{,i} + \nu(u_{i,jj} - 2St u_{i,12} + S^2 t^2 u_{i,11}) \tag{2-22}$$

The Poisson equation for the pressure is

$$P_{,ii} - 2St\, p_{,12} + St^2 p_{,11} = H_{i,i} - St\, H_{2,1} \tag{2-23}$$

Finally, the scalar equation becomes

$$\frac{\partial \theta}{\partial t} = -(\theta u_j)_{,j} + St(\theta u_2)_{,1} - S_2 u_2 + D\left[\theta_{,jj} - 2St\theta_{,12} + S^2 t^2 \theta_{,11}\right] \tag{2-24}$$

In Eq. (2-22)

$$H_i = -(u_i u_j)_{,j} + St(u_i u_2)_{,1} - S u_2 \delta_{i2} + \nu(u_{i,jj} - 2St\, u_{i,12} + S^2 t^2 u_{i,11}) \tag{2-25}$$

The governing equations for turbulent homogeneous shear flow with mixing of a passive scalar are (2-22) through (2-24). The transformed equations admit periodic boundary conditions, which in turn permit the use of spectral methods of computing derivatives.

The Poisson equation for the pressure must be derived such that the continuity equation is satisfied at the following time. The discretized equation for pressure which has this property when we use the Adams-Bashforth method for the time differencing has the following form:

$$\left[\frac{\partial}{\partial x_j}\frac{\partial}{\partial x_j} - S(2n+1)\,\Delta t\,\frac{\partial^2}{\partial x_1 \partial x_2} + S^2 n(n+1)\Delta^2 \frac{\partial^2}{\partial x_1^2}\right] p^n = H^n_{i,i} - S(n+1)\Delta t H^n_{2,1} - \frac{1}{3} G^n \tag{2-26}$$

$$G^n = H^{n-1}_{i,i} - p^{n-1}_{,ii} + S(n-1)\,\Delta t\, p^{n-1}_{,12} - S(n+1)\left[H^{n-1}_{2,1} - p^{n-1}_{,12} + S(n-1)\,\Delta t p^{n-1}_{,11}\right]\Delta t \tag{2-27}$$

D. Remeshing

There are terms in Eqs. (2-21) through (2-24) which contain St as a coefficient. As time increases, these terms become large and cause numerical problems. In other words, the x_1 and x_2 axes become more nearly parallel as time increases and the equations become stiff. To avoid this problem we use a procedure which was first used by Rogallo (1978). We start the calculation with coordinates orthogonal (Fig. 2-3a). Then, after a number of time steps (see Fig. 2-3b) we stop the calculation and rotate the $x_1 = 0$ line to the other side of the normal, as shown in Fig. 2-3c, and continue the calculations. This procedure is called remeshing and is exact only if it is done at St = 0.5, 1.0, or 1.5, etc. for these times, there is no need to interpolate the data to get the information at the new mesh points after remeshing. However, there is an aliasing problem associated with this. To show this, let us assume that the velocity, u, at St = 0.5, has the form:

$$u(x_1,x_2) = u(k_1,k_2)\, e^{ik_1x_1}\, e^{-ik_2x_2} \tag{2-28}$$

If remeshing is done at St = 0.5, then, after remeshing, St = -0.5 and the new coordinate is

$$\begin{aligned} x_1' &= x_1 + x_2 \\ x_2' &= x_2 \end{aligned} \tag{2-29}$$

Substituting (2-29) into (2-28), we find the velocity after remeshing has the following form:

$$u(x_1',x_2') = \hat{u}(k_1,k_2)\, e^{ik_1x}\, e^{-i(k_1+k_2)x_2} \tag{2-30}$$

If $k_1 + k_2$ falls outside the available wavenumber range, the information will appear in lower wave numbers. This problem is called aliasing and can be eliminated by setting the amplitudes of wavenumbers at and above two-thirds of the maximum wavenumber to zero both before and after remeshing.

E. Computational Details

In homogeneous shear flows, the length scales grow indefinitely. Therefore, the assumption of periodic boundary conditions with finite period becomes invalid after some time. However, if we use a relatively large computational box, we are able to study the flow for a limited time, i.e., until the large scales become comparable to the box length. The number of mesh points is limited by the size of the computer memory. The maximum number of mesh points one can use on available computers is $64 \times 64 \times 64$. In most of our computer runs, we were able to carry the computation up to $St = 7.0$, at which time the length scales become too large. The number of time steps for each run depends on the time step and the shear rate, and varies between 182 and 900. The computing time per computational time step is about 68.49 seconds of CPU time on ILLIAC IV.

The acccuracy and stability of the numerical method are discussed in Appendix A and briefly explained below. A two-step method has two roots when applied to the equation:

$$\frac{df}{dt} = (N_\nu + iN_c)\, f \tag{2-31}$$

For the method of Eq. (2-11), these roots are

$$R_{1,2} = \frac{1}{2} - \frac{3}{4}(N_\nu + iN_c) \pm \sqrt{\frac{1}{4} - \frac{9}{16}(N_\nu + iN_c)^2 - (N_\nu + iN_c)} \tag{2-32}$$

R_2 is a parasitic root. For the case when f in Eq. (2-31) is u_i, using linear stability analysis (see Appendix A), the Courant number, N_c, and the viscous stability parameter, N_ν, are defined as

$$N_c = \frac{N-1}{2}\left[|u_{1max}| + (1 + St)|u_{2max}|\right]\Delta t \tag{2-33}$$

$$N_\nu = \left[\left(\frac{N-1}{2}\right)^2 \left(-3 + 2St - S^2t^2\right) + \frac{1}{2} S \left|\frac{u_{2max}}{u_{1max}}\right| \delta_{i1}\right] \nu\Delta t \tag{2-34}$$

The values of R_1 and R_2 as a function of C_c and N_ν are given in Table 2-1. We chose Δt such that N_c and N_ν and therefore R_1 and R_2 lie in the range where the solution is stable and more accurate. For the isotropic case, $S = 0$, we chose the time step, $\Delta t = 0.21$, so that both N_c and N_ν are less than 0.3. For the homogeneous shear flow, the time step is also chosen to give a Courant number of less than 0.3.

The initial three-dimensional spectra of energy and scalar quantity are similar to those used for the isotropic homogeneous case, and are given in Fig. 2-4.

Table 2-1

Accuracy and Stability Limits

N_ν	N_c	R_1	R_2
0.0	0.0	1.00	0.00
0.0	0.1	1.00^+	0.050
0.0	0.2	1.00^+	0.010
0.0	0.3	1.00^+	0.150
0.0	0.4	1.01	0.198
0.1	0.0	0.905	0.552
0.1	0.1	0.904	0.0782
0.1	0.2	0.900	0.124
0.1	0.3	0.895	0.177
0.1	0.4	0.888	0.232
0.2	0.0	0.822	0.122
0.2	0.1	0.819	0.136
0.2	0.2	0.812	0.174
0.2	0.3	0.800	0.225
0.2	0.4	0.780	0.287
0.3	0.0	0.750	0.200
0.3	0.1	0.747	0.211
0.3	0.2	0.738	0.244
0.3	0.3	0.721	0.294
0.3	0.4	0.694	0.360

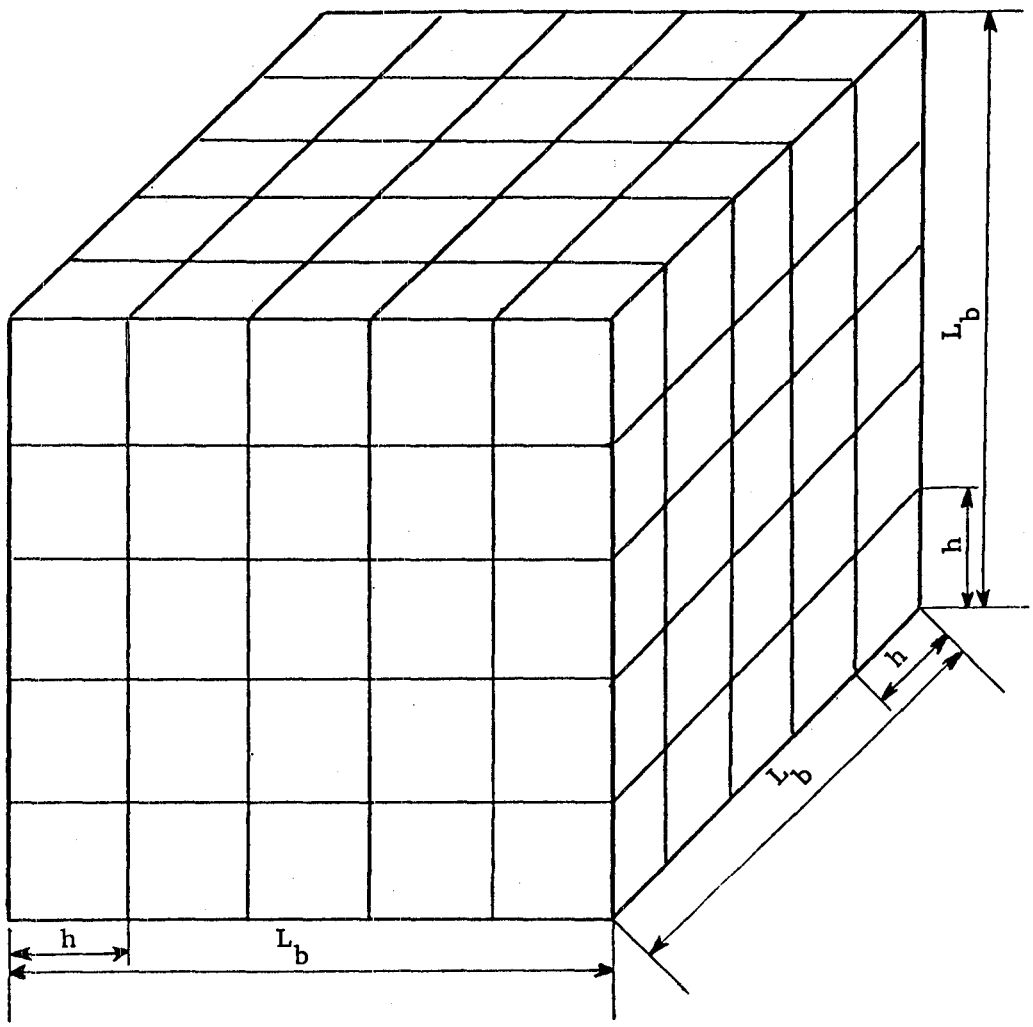

Fig. 2-1. The computational box. L_b is the box length and h is the mesh size.

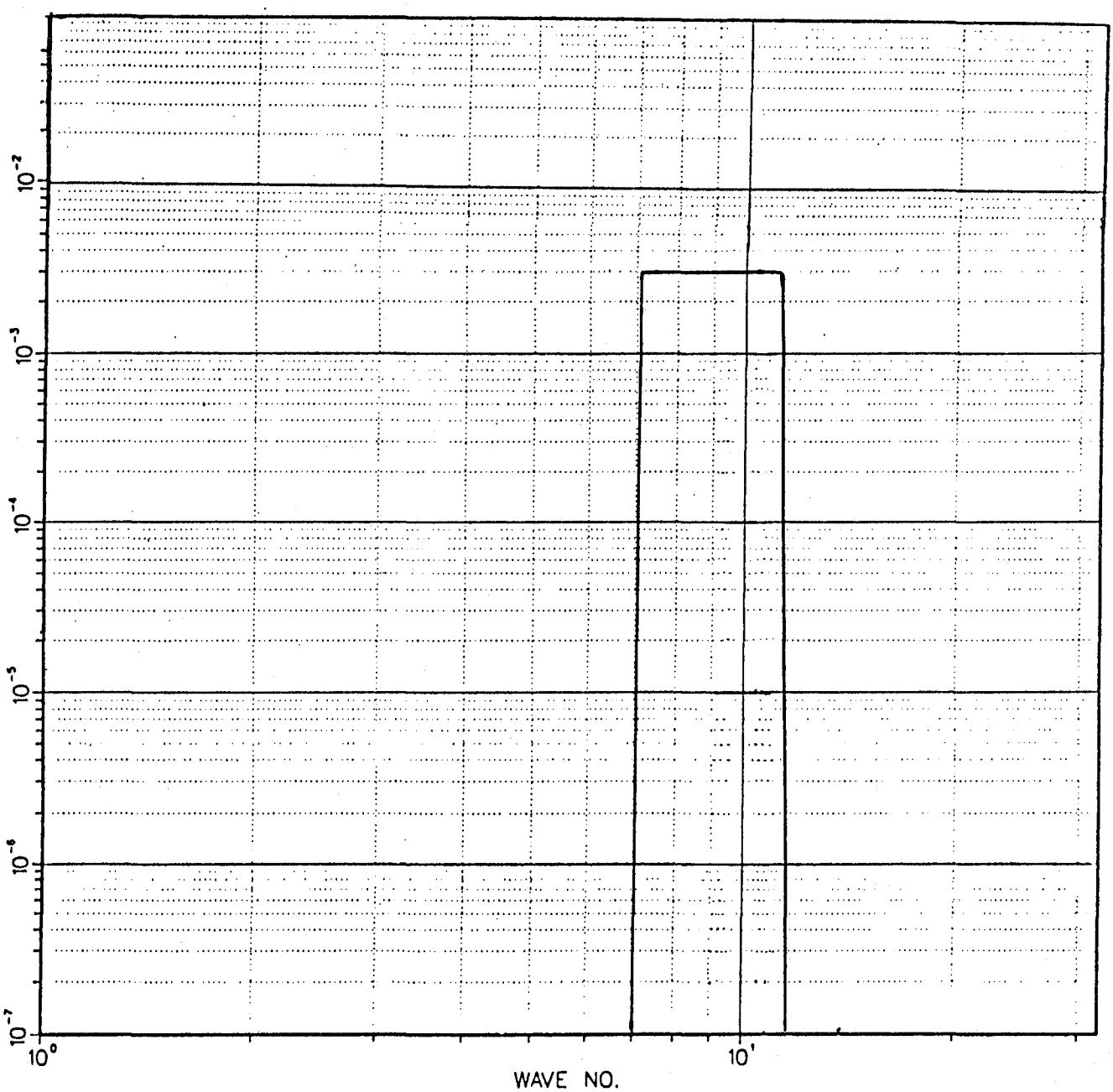

Fig. 2-2. Three-dimensional initial energy (or scalar) spectrum (32^3 mesh points).

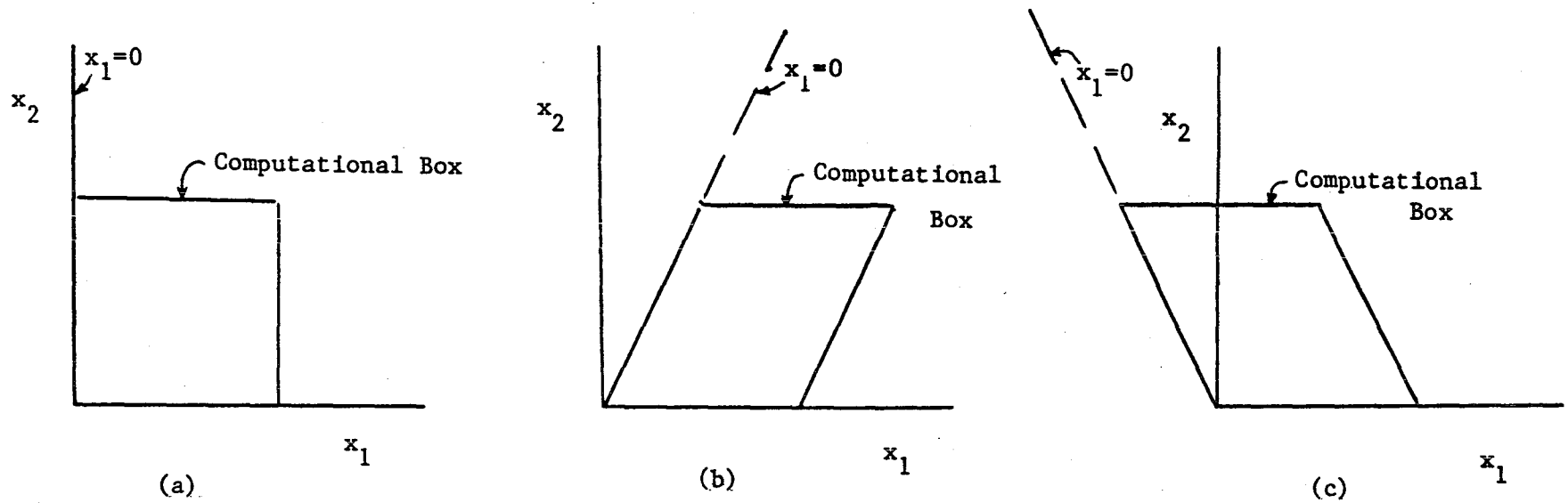

Fig. 2-3. Coordinate transformation and remeshing.
(a) Coordinate at St = 0.
(b) Coordinate at St = 0.5 (before remeshing).
(c) Coordinate at St = -0.5 (after remeshing).

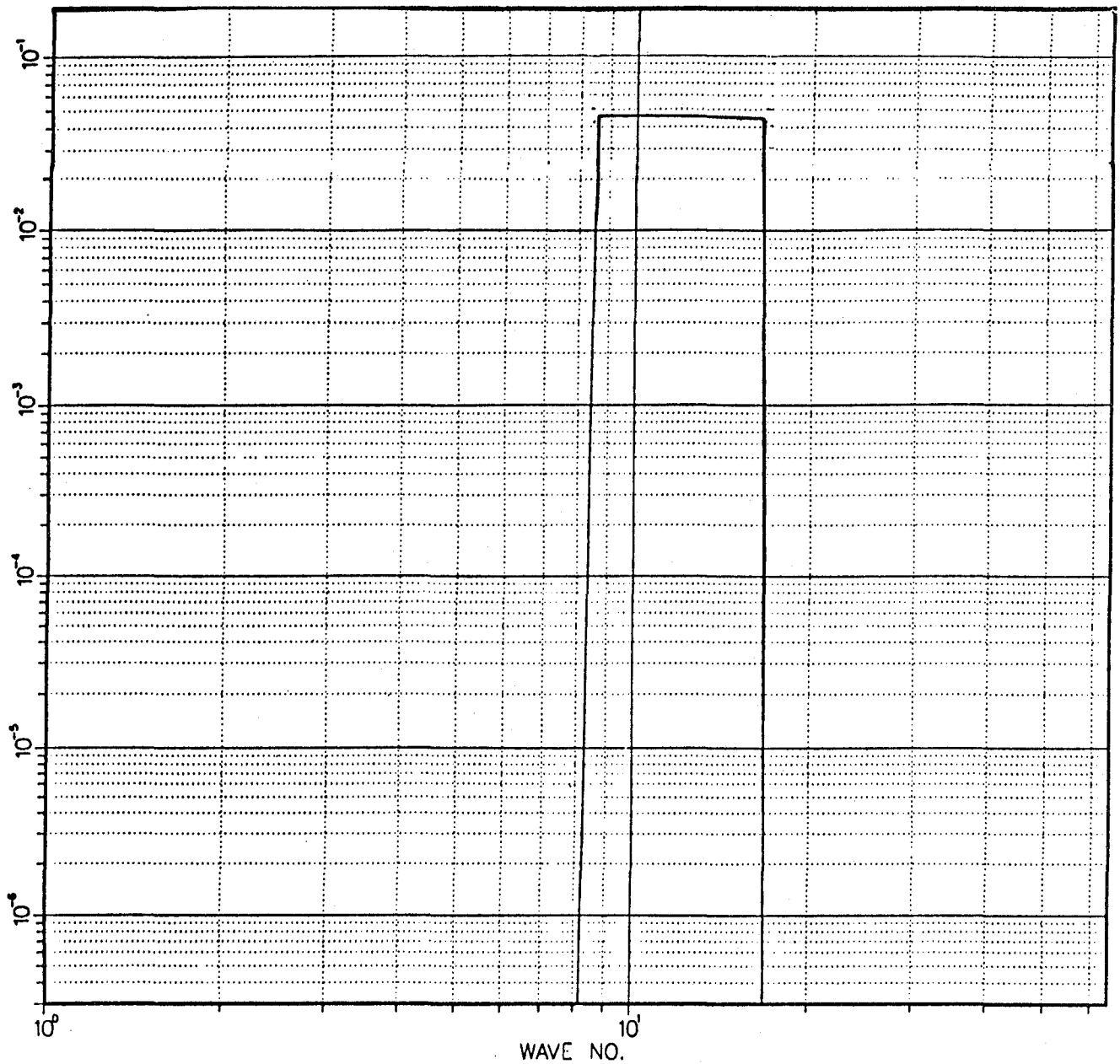

Fig. 2-4. Three-dimensional initial energy (or scalar) spectrum (64^3 mesh points).

Chapter III

COMPUTER PROGRAMMING AND CODE TESTING

In this chapter we describe the construction and testing of the computer code and list the parameters of the flow fields simulated by the code.

3.1. ILLIAC-IV Computer

The computations are done on the ILLIAC-IV computer. The ILLIAC contains 64 processors which operate in parallel and are controlled by a central managing computer. Each processor has a rather small memory. The array of processors has access to a large rotating disk on which most of the flow field data reside. Portions of the data are transferred to the computer memory for the actual processing. The computer program and data management must be constructed carefully so that (a) the time spent transferring the data from the disk to the computer memory and vice-versa is minimized, (b) modification of the code and analyzing the results are easily done. We chose the data-management system developed by Lomax (1967). In that system, called the "pencil system," we move a column of data containing $8 \times 16 \times N$ words, where N is the number of mesh points in a given direction, at a time (see Fig. 3-1). All derivatives in one direction are computed while the appropriate column of data is in the computer memory. To compute all the derivatives, it is necessary to go through the entire flow field three times. This involves a lot of data transfer. However, the time consumed in transferring the data from the disk to the computer memory or vice-versa is a rather small portion of the total time (8.8% for 64^3 mesh points).

3.2. The Code

The computer program contains three different codes:

A. A code which computes the initial conditions. This code generates and stores the initial fields for both hydrodynamic and the scalar fields (see Chapter II, Section 2.3, for details of this program).

B. The main code, which advances the velocity and scalar fields in time using the Poisson, Navier-Stokes, and diffusion equations, as discussed in Chapter II. This code also stores the velocity and scalar fields on tape at the time when the coordinates are orthogonal (St = 0); in the case of an isotropic homogeneous flow, the flow field is stored every 50 time steps.

C. A code which uses the flow fields to compute various turbulence statistics and one- and three-dimensional spectra of various terms.

We also used IBM 360 and CDC 7600 computers for final data reductions and for plotting the data.

The ILLIAC codes can operate with 16^3, 32^3, and 64^3 mesh points. The run time for each case is given in Chapter II.

3.3. Testing the Code

It is important to make sure that the code is properly constructed. To check the validity of the results, the following items were examined.

A. Conservation Laws

The simulated flow fields satisfy continuity and the energy balance throughout the computations. The relative error for continuity is

$$\frac{(u_{i,i})_{max}}{q/L} = 0.001\%$$

and, for the energy balance,

$$\frac{\frac{dq/2}{dt}}{\text{Production} - \text{Dissipation}} - 1 = \text{few percent}$$

where the production and dissipation terms are calculated directly, and a second-order approximation is used to calculate dq^2/dt. The errors in the energy balance are mainly due to the time differencing.

B. Comparison with Similar Computed Flow Fields.

The simulated hydrodynamic field is checked against the results obtained by Rogallo (1978) and Feiereisen et al. (1981), who independently developed similar codes to simulate homogeneous turbulent shear flows for incompressible and compressible flows, respectively. The overall behavior of turbulent statistics for the hydrodynamic field, as will be explained in Chapter VI, are similar in all three simulated flow fields.

C. Comparison with the Exact Solutions of the Navier-Stokes and Diffusion Equations

An exact analytical solution to the Navier-Stokes and diffusion equations for two-dimensional incompressible flow exists. This solution, which is known as the vortex-cell or two-dimensional Taylor-Green solution, represents a flow field consisting of two-dimensional vortices, arranged rectangularly, which decay in strength with time. The solution has the following form:

$$
\begin{aligned}
u &= -A \cos k_1 x_1 \sin k_2 x_2 \, e^{-(k_1^2+k_2^2)\nu t} \\
v &= A \frac{k_1}{k_2} \sin k_1 x_1 \cos k_2 x_2 \, e^{-(k_1^2+k_2^2)\nu t} \\
C &= B \cos k_1 x_1 \cos k_2 x_2 \, e^{-(k_1^2+k_2^2)Dt} \\
P &= -\frac{A^2}{4} \cos 2k_1 x_1 + \frac{k_1^2}{k_2^2} \cos 2k_2 x_2 \, e^{-2(k_1^2+k_2^2)\nu t}
\end{aligned}
\qquad (3\text{-}1)
$$

We set the initial conditions by putting $t = 0$ in Eqs (3-1). We obtain the results for several values of k_1 and k_2 and for both inviscid and viscous flows. Note that k_1 and k_2 must be small to avoid aliasing. The exact results were compared with results obtained from the computer code after 80 time steps. To check the coordinate transformation, we obtained the results for skewed coordinates when St = 0.5. For all cases the results were obtained using 16^3 mesh points, and the difference between the exact results and the computer results was less than 1.7×10^{-4}%.

D. Comparison with Experimental Data

As mentioned in the first chapter, homogeneous shear flow was generated experimentally by several people, we mainly check our results with the experiment by Tavoularis (1978), because they generated both hydrodynamic and scalar fields. As will be discussed in Chapter VI, our results are in very good agreement with the results obtained from this experiment. However, since the experimental results are obtained at higher Reynolds number than the simulated results, there are slight differences between the results.

3.4. Description and Details of the Computer Runs

We have simulated several flow fields for both isotropic homogeneous turbulence and homogeneous turbulent shear flow. For each run, the computed flow field can be divided into three parts.

A. The "Developing" Region

As described in the last chapter, we start the computations with artificial initial fields. Therefore, there is an initial period in which the simulated flow fields are not true turbulent fields. This is called the "developing" period. In the case of isotropic homogeneous flow, the development is considered complete when the velocity and the scalar derivative skewnesses reach asymptotic values. The skewness is defined as:

$$S_k = \left\langle \left(\frac{\partial u_i}{\partial x_i} \right)^3 \right\rangle \Big/ \left\langle \left(\frac{\partial u_i}{\partial x_i} \right)^2 \right\rangle^{3/2} \qquad \text{(no summation)} \qquad (3\text{-}2)$$

In the shear flow with mixing of a scalar whose mean is linear in space, the criteria by which the end of the development period is judged are:

(1) The shear stress correlation coefficient $\langle u_1 u_2 \rangle / u_1' u_2'$ and one point velocity scalar correlation coefficient $\langle \theta u_i \rangle / \theta' u_i'$ reach asymptotic values (see Fig. 6-17), where u_i' and θ' are the r.m.s. velocity and scalar fluctuations.

(2) The three-dimensional spectra of kinetic energy and the scalar reach asymptotic shapes.

(3) The ratio of production to dissipation in the turbulent kinetic energy and r.m.s. scalar fluctuation equations reach asymptotic values.

(4) The rate of change of Reynolds stress anisotropy tensor with time becomes small.

B. The "Developed" Region

After the initial period, there is a period in which the simulated flow fields can be regarded as true turbulent flows. In this period, the statistics are extracted from the flow fields. These will be discussed extensively in Chapters V and VI. For all computed runs, the developed region lies between $St = 4$ and $St = 7$, where St is non-dimensional time.

C. The "Anomalous" Region

In both isotropic and shear flows, the scales of motion grow with time, and there is a time at which the scales become too large for the computational box and the periodic boundary conditions are no longer accurate. Beyond this point, the flow fields do not accurately represent homogeneous shear flow (or isotropic flow). Therefore the simulation is stopped. This time is chosen by looking at the two-point correlations of the velocity and the scalar fields. The two-point velocity correlation is defined as

$$R_{ij}(\vec{r}) = \frac{< u_i(\vec{x})\, u_j(\vec{x}+\vec{r}) >}{< u_i(\vec{x})\, u_j(\vec{x}) >} \qquad (3\text{-}3)$$

For the isotropic flows, we used 32^3 mesh points and various values of Reynolds and Prandtl numbers. The results will be discussed in Chapter V.

For homogeneous shear flow, we used 64^3 mesh points and simulated fourteen scalar fields and six different flow fields. Table 3-1 gives some details of the runs.

Table 3-1

DETAILS FOR EACH SIMULATED FIELD

Run	Reynolds* Number	Shear Number* SL/q	Prandtl Number	Symbol
HS64A	44.56	18.55	1.00	□
HS64B	19.00	23.73	1.00	○
HS64C	19.00	23.73	5.00	▽
HS64D	44.56	18.55	5.00	⊠
HS64E	44.56	18.55	0.20	✳
HS64F	19.00	23.73	0.20	◇
HS64G	60.35	66.88	1.00	△
HS64H	60.35	66.88	5.00	◯
HS64I	60.35	66.88	0.20	⧓
HS64J	24.20	11.23	1.00	+
HS64M	29.16	8.94	1.00	×
HS64N	29.16	8.94	.20	⊞
HS64O	64.31	6.38	1.00	◇
HS64P	64.31	6.38	0.20	⊗

*All values are given at St = 4.00.

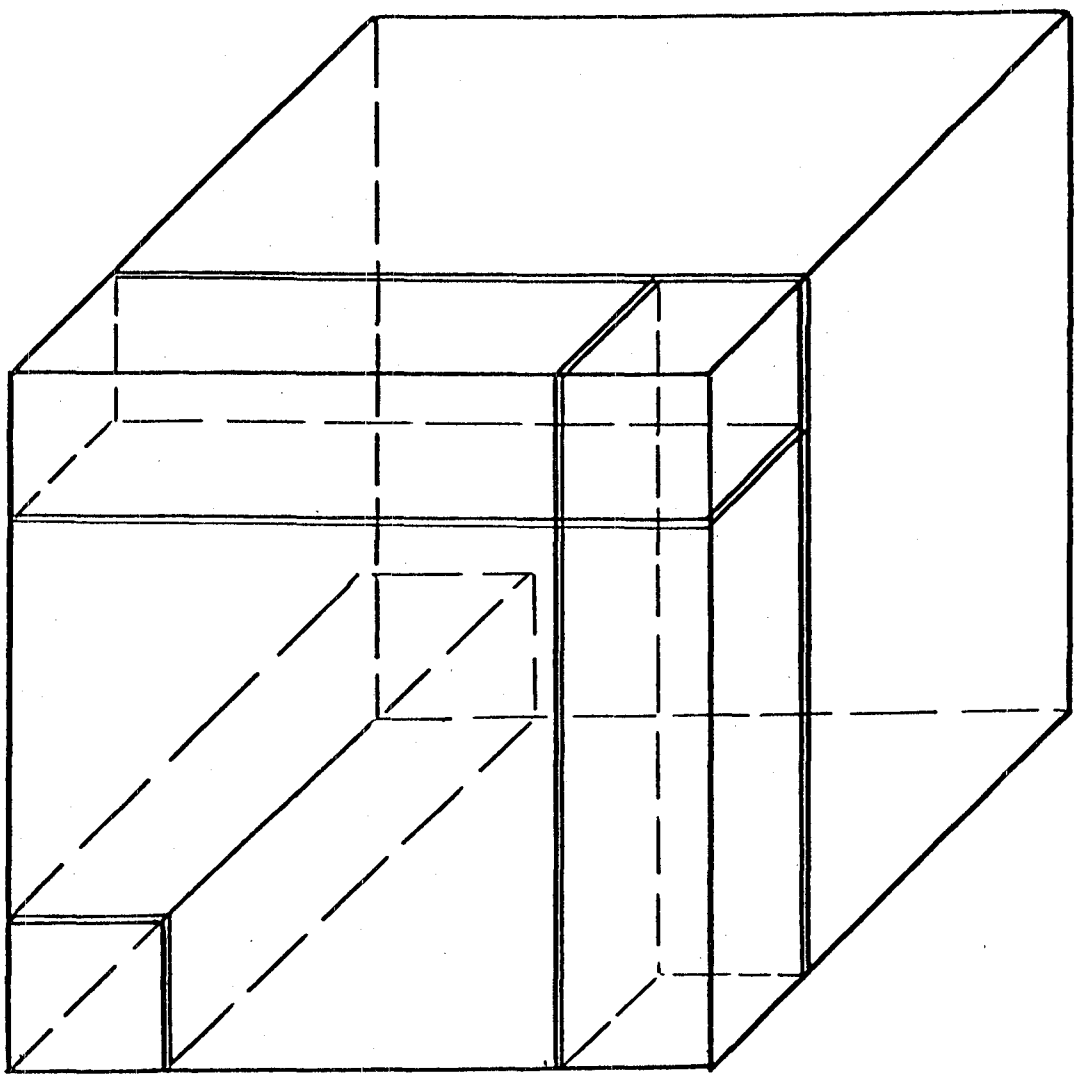

Fig. 3-1. The computational box with three columns of data in different directions.

Chapter IV

STATISTICAL MODELS OF TURBULENCE

In this chapter, we present averaged equations for both the hydrodynamic and scalar fields. We are interested in comparing and contrasting the behavior of terms in the equations for two fields. We also present some of the models which have been used for the various terms in these equations. The terms which are modeled can be calculated from the numerical results of the preceding chapter and will be discussed in the following chapters.

The equations are derived for homogeneous shear flow. They can be used for isotropic homogeneous flows by setting $S = S_2 = 0$. In order to avoid complexity, we derive the equations for the case when the coordinates are orthogonal, i.e., $St = 0$.

4.1 Equations for Turbulent Statistical Quantities

The equations of motion for homogeneous turbulent shear are Eqs. (2-22) through (2-24). The momentum equation and the convection-diffusion equation for a scalar quantity have the following forms (note that we set $St = 0$):

$$\frac{\partial u_i}{\partial t} = -(u_i u_j)_{,j} - S u_2 \delta_{i1} - p_{,i} + \nu u_{i,jj} \qquad (4\text{-}1)$$

and

$$\frac{\partial \theta}{\partial t} = -(\theta u_j)_{,j} - S_2 u_2 + D\theta_{,jj} \qquad (4\text{-}2)$$

where, as before,

$$S = \frac{\partial \overline{U}_1}{\partial x_2} \quad \text{and} \quad S_2 = \frac{\partial \overline{C}}{\partial x_2}$$

Assuming the boundary conditions for two fields are similar, one sees that there is a close analogy between x_1-momentum u_1 and the scalar θ if $Pr = \nu/D = 1$, $S = S_2$, and $\partial P/\partial x$ is small compared to the other terms. Similarly, if $\partial P/\partial x_2$ or $\partial P/\partial x_3$ and $S_2 u_2$ are small

(i.e., in the isotropic case), $Pr = 1$ and $S = S_2$, then an analogy exists between x_2 or x_3-momentum and the scalar.

The equations describing the three components of turbulent kinetic energy can be derived by taking the volume average of Eq. (4-2) multiplied by u_i (no summation):

$$\frac{\partial < u_1^2 >/2}{\partial t} = \frac{1}{2}\phi_{11} - \frac{1}{2}\varepsilon_{11} - < u_1 u_2 > S \qquad (4\text{-}3)$$

$$\frac{\partial < u_2^2 >/2}{\partial t} = \frac{1}{2}\phi_{22} - \frac{1}{2}\varepsilon_{22} \qquad (4\text{-}4)$$

$$\frac{\partial < u_3^2 >/2}{\partial t} = \frac{1}{2}\phi_{33} - \frac{1}{2}\varepsilon_{33} \qquad (4\text{-}5)$$

where

$$\phi_{ij} = < p(u_{i,j} + u_{j,i}) > \qquad (4\text{-}6)$$

$$\varepsilon_{ij} = 2\nu < u_{i,k} u_{j,k} > \qquad (4\text{-}7)$$

and $< >$ denotes the volume average. The third term on the right-hand side of Eq. (4-3) is the production term. Through the action of this term, energy is transferred from the mean flow to the fluctuating part of the flow. The pressure-velocity covariance terms, ϕ_{ij}, transfer energy from $< u_1^2 >$ to $< u_2^2 >$ and $< u_3^2 >$. Thus we expect $\phi_{11} < 0$, $\phi_{22} > 0$, and $\phi_{33} > 0$. Also, $\phi_{11} + \phi_{22} + \phi_{33} = 0$, so the sum of these terms neither produces nor destroys turbulent kinetic energy. Thus, these terms merely transfer energy from from one component to another. Since energy is transferred from the mean flow to the large scales of turbulence, we expect the production term and ϕ_{ij} to be most important at low wave numbers. ε_{ij} is the dissipation term. Its trace, $\varepsilon_{11} + \varepsilon_{22} + \varepsilon_{33}$, is positive-definite, and is important at relatively high wave numbers. We shall show direct evidence of the spectra of these terms in the following chapter.

The turbulent kinetic energy equation can be obtained by summing Eqs. (4-3), (4-4), and (4-5), and is

$$\frac{\partial q^2/2}{\partial t} = - \langle u_1 u_2 \rangle S - \nu \langle u_{i,j} u_{i,j} \rangle \qquad (4\text{-}8)$$

The first term represents production and the second, dissipation.

The equation for the r.m.s. scalar quantity can be derived from Eq. (4-2) and is:

$$\frac{\partial \langle \theta^2 \rangle/2}{\partial t} = - \langle u_2 \theta \rangle S_2 - D \langle \theta_{,j} \theta_{,j} \rangle \qquad (4\text{-}9)$$

The first term on the right-hand side of Eqs. (4-9) is the production term, and the second is the dissipation term.

The Reynolds stress $\langle u_1 u_2 \rangle$ and turbulent heat flux $\langle \theta u_j \rangle$ equations can be derived in a manner similar to those used in deriving the above equations, and have the following forms:

$$\frac{\partial}{\partial t} \langle -u_1 u_2 \rangle = \langle u_2^2 \rangle S - \phi_{12} + \varepsilon_{12} \qquad (4\text{-}10)$$

$$\frac{\partial}{\partial t} \langle -\theta u_2 \rangle = \langle u_2^2 \rangle S_2 - \phi_2 + \varepsilon_2 \qquad (4\text{-}11)$$

$$\frac{\partial}{\partial t} \langle \theta u_1 \rangle = - \langle u_2 \theta \rangle S - \langle u_1 u_2 \rangle S_2 + \phi_1 - \varepsilon_1 \qquad (4\text{-}12)$$

where ϕ_{12} is defined by Eq. (4.6) and

$$\phi_i = \langle p \theta_{,i} \rangle \qquad (4\text{-}13)$$

and

$$\varepsilon_i = (D+\nu) \langle \theta_{,k} u_{i,k} \rangle \qquad (4\text{-}14)$$

In the above equations, the terms $\langle u_2^2 \rangle S$, $\langle u_2^2 \rangle S_2$, and $- [\langle u_2 \theta \rangle S + \langle u_1 u_2 \rangle S_2]$ are production terms.

It is not obvious whether ε_{12}, ε_2, and ε_1 help or prevent the growth of the correlations. However, from our results, they are negative and are thus dissipative. The pressure-velocity and pressure-scalar covariances also tend to hinder the growth of the correlations. This can be shown by considering the return to isotropy at high Reynolds number. In this case the dissipation terms are negligible; thus the pressure-velocity and pressure-scalar covariance are responsible for destroying the correlations, and must therefore be negative.

The equations given above are exact, but they contain many more variables than there are equations, so the system is not closed. To close the system, it is necessary to make assumptions about the relationships among the various ~~flows~~ quantities. This is the issue of modeling that will be discussed next.

4.2 Statistical Models

In this section we further consider the production, dissipation, and pressure-velocity and pressure-scalar covariance terms which were discussed in the last section. We review a number of models.

A. Turbulent Reynolds Stress and Heat Flux

The Reynolds stresses $< u_i u_j >$ appear in the mean momentum equations, and the heat flux (mass flux if the scalar is concentration) $< \theta u_i >$ appears in the mean diffusion equation. If the only mean velocity gradient is $\partial \overline{U}_1 / \partial x_2$, the mean turbulent Reynolds stress tensor takes the following form:

$$< u_i u_j > = \begin{bmatrix} < u_1^2 > & < u_1 u_2 > & 0 \\ < u_1 u_2 > & < u_2^2 > & 0 \\ 0 & 0 & < u_3^2 > \end{bmatrix} \qquad (4\text{-}15)$$

The principal stresses are

$$-\sigma_1 = \frac{< u_1^2 > + < u_2^2 >}{2} + \left[\frac{(< u_1^2 > - < u_2^2 >)^2}{2} + < u_1 u_2 >^2 \right]^{1/2}$$

$$-\sigma_2 = \frac{< u_1^2 > + < u_2^2 >}{2} - \left[\frac{(< u_1^2 > - < u_2^2 >)^2}{2} + < u_1 u_2 >^2 \right]^{1/2} \qquad (4\text{-}16)$$

and

$$-\sigma_3 = - < u_3^2 >$$

The direction of the principal axis in the x_1, x_2 plane relative to the coordinate system is

$$\alpha_1 = \frac{1}{2} \tan^{-1} \frac{2 < u_1 u_2 >}{< u_1^2 > - < u_2^2 >} \tag{4-17}$$

To close the mean momentum and diffusion equations, the Reynolds stress tensor and the heat flux vector must be modeled. The most common models for those terms are Newtonian-like constitutive equations, which is the Boussinesq eddy-viscosity concept. In the most general form the Reynolds stress tensor can be modeled by

$$< u_i u_j > = - 2\nu_{Tijpq} S_{pq} + \frac{1}{3} q^2 \delta_{ij} \tag{4-18}$$

where

$$S_{pq} = \frac{1}{2} (\overline{U}_{p,q} + \overline{U}_{q,p}) \tag{4-19}$$

$$q^2 = < u_i u_i > \tag{4-20}$$

and ν_{Tijpq} is a fourth-rank eddy viscosity tensor which needs to be defined. We looked at models for ν_{Tijpq} which are linear and quadratic functions of S_{ij}, and δ_{ij}. For each case the model was reduced to a simple expression which can be obtained using the following form of the eddy viscosity model:

$$< u_i u_j > = - 2\nu_T S_{ij} + \frac{1}{3} \delta_{ij} q^2 \tag{4-21}$$

where ν_T is a scalar eddy viscosity. This model is not accurate for this flow because it requires $< u_1^2 > = < u_2^2 >$. A more complicated model for $< u_i u_j >$ was derived by Wilcox and Rubesin (1980). This model is especially good for the log region of the boundary layer when the magnitudes of production and dissipation are close. The model predicts the behavior of $< u_1^2 >$, $< u_2^2 >$, and $< u_3^2 >$. For Reynolds shear stress, $< u_1 u_2 >$, the model reduces to Eq. (4-21). Rodi (1976) also derived an algebraic model for $< u_i u_j >$ which is nonlinear in $< u_i u_j >$ and is based on the assumption that $< u_i u_j > / < u_i u_i >$ = constant and is

good for high Reynolds number flows. The model (4-21) is used by many people to calculate the Reynolds shear stress $< u_1 u_2 >$. We shall use this model for $< u_1 u_2 >$ and calculate the eddy viscosity. Modelers have used various forms for ν_T. We describe the ones applicable to our flow and specifically exclude models designed to apply only to boundary layers.

The simplest model for ν_T is based entirely on information from the mean flow.

$$\nu_T = C \sqrt{S_{ij} S_{ij}}\, L_m^2 \tag{4-22}$$

where C is a constant and L_m is a mixing length. Models of this kind are used in boundary layers (for which L_m is a function of the distance from the wall) and free shear layers (for which L_m is a given fraction of the shear layer thickness).

A more complex model for the eddy viscosity, which involves some information about the fluctuating field, has the following form:

$$\nu_T = C q L_m \tag{4-23}$$

where C is constant and the turbulence velocity, q, is obtained by solving the turbulent kinetic energy equation, in which the higher-order terms are modeled (see W. C. Reynolds, 1976, for more details). L_m is a mixing length which is prescribed as above. This is known as a one-equation model.

A still more complex model is obtained by using Eq. (4-23) with a length scale defined by

$$L_d = C_o \frac{q^3}{\varepsilon} \tag{4-24}$$

in place of L_m; here, ε is the dissipation or, more correctly, the energy transfer from the large scales to the small ones, and can be obtained from an equation for the dissipation (see W. C. Reynolds, 1976). This is a two-equation model. For the low Reynolds numbers, the dissipation length scale is modified as follows:

$$L_d = C_o \frac{q^3}{\varepsilon}\left[1 + \frac{C_1}{Re_\lambda}\right] \tag{4-25}$$

where Re is Reynolds number based on a Taylor microscale and q.

Similarly, the heat flux vector can be modeled as follows:

$$\langle \theta u_i \rangle = D_{ij} \frac{\partial \overline{C}}{\partial x_j} \tag{4-26}$$

where D_{ij} is turbulent eddy diffusivity and is a second-rank tensor. If $\partial \overline{U}_1 / \partial x_2$ is the only nonzero mean velocity gradient, D_{ij} has the following form:

$$D_{ij} = \begin{pmatrix} D_{11} & D_{12} & 0 \\ D_{21} & D_{22} & 0 \\ 0 & 0 & D_{33} \end{pmatrix} \tag{4-27}$$

D_{ij} is not necessarily symmetric. To model this term, we decompose it as follows:

$$D_{ij} = D_{ij}^{(1)} + D_{ij}^{(2)} + D_{ij}^{(3)} \tag{4-28}$$

where

$$D_{ij}^{(1)} = \frac{1}{2}(D_{ij} + D_{ji}) - \frac{1}{3} D_{kk} \delta_{ij} \tag{4-29}$$

is a symmetric trace-free tensor,

$$D_{ij}^{(2)} = \frac{1}{2}(D_{ij} - D_{ji}) \tag{4-30}$$

is an antisymmetric tensor, and

$$D_{ij}^{(3)} = \frac{1}{3} D_{kk} \delta_{ij} \tag{4-31}$$

is a diagonal tensor. The above three expressions for D_{ij} need to be modeled. In general, D_{ij} can be written as:

$$D_{ij} = D_{ij}(b_{ij}, S_{ij}, \Omega_{ij}, \text{scalars}) \tag{4-32}$$

where b_{ij} is the Reynolds stress anisotropy and is defined as

$$b_{ij} = \frac{\langle u_i u_j \rangle}{q^2} - \frac{1}{3}\delta_{ij} \tag{4-33}$$

S_{ij} is defined by Eq. (4-19), and Ω_{ij} is the mean tensor defined as

$$\Omega_{ij} = \frac{1}{2}(\overline{U}_{i,j} - \overline{U}_{j,i}) \tag{4-34}$$

Note that we do not include the dissipation anisotropy, d_{ij}, in the right side of Eq. (4-32), because d_{ij} results mainly from the small scale structures, while D_{ij} is dependent mainly on the large scales.

$D_{ij}^{(1)}$ and b_{ij} are both symmetric, trace-free, and have the same zero components. Since the scalar fluctuation is similar to the velocity fluctuations, $D_{ij}^{(1)}$ and b_{ij} are both quadratic functions of the velocity field. Therefore, we assumed $D_{ij}^{(1)}$ is a linear function of b_{ij}.

$$D_{ij}^{(1)} = C_1 \frac{q^2}{S} b_{ij}$$

where C_1 is a constant and L is a length scale. $D_{ij}^{(2)}$ is an antisymmetric tensor; therefore it must be modeled with the only antisymmetric tensor available, Ω_{ij}. Neglecting higher-order terms, $D_{ij}^{(2)}$ should have the following form:

$$D_{ij}^{(2)} = C_2 \frac{q^2}{S^2} \Omega_{ij}$$

where C_2 is a constant.

Finally, $D_{ij}^{(3)}$ can be written as follows:

$$D_{ij}^{(3)} = C_3 \frac{q^2}{S} \delta_{ij}$$

Therefore, Eq. (4-28) becomes

$$\frac{D_{ij}}{q^2/S} = C_1 b_{ij} + C_2 \frac{1}{S} \Omega_{ij} + C_3 \delta_{ij} \qquad (4\text{-}35)$$

where C_1, C_2, and C_3 may be functions of the Reynolds shear, and Prandtl numbers, and invariants of the above-mentioned tensors.

B. Turbulent Prandtl Number

The conventional turbulent Prandtl number (or turbulent Schmidt number if passive scalar is concentration) is defined as

$$Pr_T = \frac{\nu_T}{D_{22}} \qquad (4\text{-}36)$$

or

$$Pr_T = \frac{\langle u_1 u_2 \rangle \frac{\partial \bar{C}}{\partial x_2}}{\langle \theta u_2 \rangle \frac{\partial \bar{U}}{\partial x_2}}$$

The turbulent Prandtl number measures the degree of analogy between momentum and heat transport in turbulent flows and is required for heat transfer calculations. For flows involving mixing of chemical species, the important transport property is the diffusivity and the counterpart of the turbulent Prandtl number is turbulent Schmidt number. Reynolds (1885) proposed the Reynolds analogy, and Prandtl (1925) gave his mixing-length theory, both of which assume that $Pr_T = 1.0$. However, this assumption has been challenged by experimental results. Several models have been suggested (see, for example, A. J. Reynolds (1974)).

We shall consider models which are recommended by several authors or used by many people in this field. The models we shall look at are:

a) A. J. Reynolds proposed an empirical model based on experiments in wall flows, free turbulence, and core flows. Pr_T should depend on the molecular Prandtl number and a Reynolds number based on local turbulence intensity. The latter can be replaced by ν_T/ν, which is assumed to be a function of this Reynolds number. Based on these observations, he suggested that Pr_T be modeled as follows:

$$Pr_T = C_1 \exp\left[- C_2 Pr^{C_3} \left(\frac{\nu_T}{\nu} \right)^{C_4} \right] \qquad (4\text{-}37)$$

where C_1, C_2, C_3, and C_4 are positive constants.

b) Wassel and Catton (1973) used mixing-length theory and assumed that eddies are spheres which move normal to the mean flow and have a radius proportional to the mixing length. Their model, based on this assumption, is

$$Pr_T^{-1} = (C_1 Pr) \frac{1 - e^{-C_2/(Pr \frac{\nu_T}{\nu})}}{1 - e^{-C_3/(\nu_T/\nu)}} \qquad (4\text{-}38)$$

C_1, C_2, and C_3 are parameters, and they suggest the values $C_1 = 1.05$, $C_2 = 5.25$, and $C_3 = 5$.

c) A model which simulates the idea that an eddy tries to equilibrate with the surrounding fluid has the following form:

$$Pr_T = \left[\frac{\alpha^2}{2} + \alpha C_1 Pe_T - (C_1 Pe_T)^2 \left(1 - e^{-(\alpha/C_1 Pe_T)}\right) \right]^{-1} \qquad (4\text{-}39)$$

where Pe_T is the turbulent Peclet number,

$$Pe_T = \frac{\nu_T}{\nu} Pr$$

and α and C_1 are constants. Crawford (1976) suggested $\alpha = 1.08$ and $C = 0.2$.

d) Using the models for turbulent eddy diffusivity, Eq. (4-35), and turbulent eddy viscosity, Eq. (4-21), the turbulent Prandtl number becomes:

$$Pr_T = \frac{1}{C_3 \frac{< u_2^2 >}{q^2} + C_4} \qquad (4\text{-}40)$$

where C_3 and C_4 are constants. They may be functions of Reynolds number, shear number and Prandtl number, and invariants of various tensors.

C. Pressure-Strain Covariance

The pressure-strain covariance, ϕ_{ij}, is defined by (4-6). ϕ_{ij} is responsible for exchanging energy between the various Reynolds stresses.

The equation for the fluctuation pressure is obtained from the Navier-Stokes equation, as explained in Section 2-1. For the homogeneous shear flow, the equation has the following form:

$$p_{,ii} = -2u_{i,j}\overline{U}_{j,i} - u_{i,j}u_{i,j} \tag{4-41}$$

The right-hand side of this equation contains two parts. The first part is proportional to the mean strain, $\overline{U}_{i,j}$, and given a sudden change of $\overline{U}_{i,j}$, it changes rapidly. On the other hand, the second term on the right of Eq. (4-41) does not depend explicitly on the mean strain, and it takes some time to change after a sudden change of the mean strain. Therefore, the two terms behave differently and need to be considered separately. We let $p = p^{(1)} + p^{(2)}$, where

$$p^{(1)}_{,ii} = -2u_{i,j}\overline{U}_{j,i} \tag{4-42}$$

$$p^{(2)}_{,ii} = -u_{i,j}u_{j,i} \tag{4-43}$$

Following Lumley and Khajeh-Nouri (1974), for homogeneous flows $p^{(1)}$ can be defined in terms of the Fourier transform of the velocity field. By definition,

$$p^{(1)}(x) = \int \hat{p}^{(1)}(k)\, e^{ikx}\, dk \tag{4-44}$$

In homogeneous flows, the mean velocity gradient is constant, so Eq. (4-42) gives

$$\hat{p}^{(1)}(k) = i2\hat{u}_i U_{j,i} \frac{k_j}{k^2} \tag{4-45}$$

where $k^2 = k_i k_i$. The part of the pressure-strain covariance associated with $p^{(1)}$ is

$$\phi_{pq}^{(1)} = \langle p^{(1)}(u_{p,q} + u_{q,p}) \rangle \tag{4-46}$$

which can be reduced to (Lumley and Khajeh-Nouri, 1974):

$$\phi_{pq}^{(1)} = 2\overline{U}_{j,i} \iint \frac{k_j}{k^2} \hat{u}_i(k) \left[\hat{u}_p^*(k')k'_q + \hat{u}_q^*(k')k'_p \right] dk'dk \tag{4-47}$$

The double integral on the right-hand side of the above equation is a fourth-order tensor, so we can write

$$\phi_{pq}^{(1)} = 2\overline{U}_{j,i} G_{ijpq} \tag{4-48}$$

From continuity, $G_{iipq} = 0$; also $G_{ijjq} = \langle u_i u_q \rangle$. This tensor cannot be simplified and must be modeled. Following Lumley's argument, G_{ijpq} should be linear in the Reynolds stress, and it can also be a function of scalar invariants of the mean strain and Reynolds stress anisotropy tensor. The most general form of the pressure-strain term consistent with the above is:

$$\begin{aligned} \phi_{pq}^{(1)} = {} & \frac{2}{5}(1+A_1) S_{pq} q^2 - \frac{3}{2} A_1 \left[R_{pk}S_{kq} + R_{qk}S_{kp} - \frac{2}{3} \langle u_i u_j \rangle \overline{U}_{i,j} \delta_{pq} \right] \\ & - \frac{4}{5} \left[\frac{5}{3} + \frac{7}{12} A_1 \right] \left[R_{pk}\Omega_{kq} + R_{qk}\Omega_{kp} \right] \end{aligned} \tag{4-49}$$

where

$$\left.\begin{aligned} S_{pq} &= \frac{1}{2}\left(\overline{U}_{p,q} + \overline{U}_{q,p}\right) \text{ is the mean strain,} \\ R_{pq} &= \langle u_p u_q \rangle \text{ is the Reynolds stress,} \\ \Omega_{pq} &= \frac{1}{2}(\overline{U}_{p,q} - \overline{U}_{q,p}) \text{ is the mean rotation tensor,} \end{aligned}\right\} \tag{4-50}$$

and A_1 is constant. The value suggested for this constant by different workers varies between -1.23 and -2.5 (see W. C. Reynolds (1976) for more details).

The above model for our case, where $\overline{U}_{i,j} = 0$, except for $\overline{U}_{1,2} = S$, has the following form:

$$\phi_{11} = \langle p^{(1)} u_{1,1} \rangle = \frac{2}{3} + \frac{2}{15} A_1 \; S \langle u_1 u_2 \rangle$$

$$\phi_{22} = \langle p^{(1)} u_{2,2} \rangle = -\frac{2}{3} + \frac{1}{3} A_1 \; S \langle u_1 u_2 \rangle \qquad (4\text{-}51)$$

$$\phi_{33} = \langle p^{(1)} u_{3,3} \rangle = \frac{1}{5} A_1 \; S \langle u_1 u_2 \rangle$$

and

$$\phi_{12} = \langle p^{(1)} (u_{1,2}+u_{2,1}) \rangle = \frac{1}{5} (1+A_1) \; sq^2 - (\frac{2}{3} + \frac{8}{15} A_1) S \langle u_1^2 \rangle + (\frac{2}{2} - \frac{1}{15} A_1) \; S \langle u_2^2 \rangle \qquad (4\text{-}52)$$

The part of pressure-velocity covariance associated with $p^{(2)}$ is

$$\phi_{ij}^{(2)} = \langle p^{(2)} (u_{i,j} + u_{j,i}) \rangle \qquad (4\text{-}53)$$

and the total pressure-strain term is

$$\phi_{ij} = \phi_{ij}^{(1)} + \phi_{ij}^{(2)} \qquad (4\text{-}54)$$

Rotta (1951) proposed the following model for $\phi_{ij}^{(2)}$:

$$\phi_{ij}^{(2)} = - A_2 \varepsilon b_{ij} \qquad (4\text{-}55)$$

where b_{ij} is the anisotropis part of the Reynolds stress tensor and defined by Eq. (4-33), and A_2 is constant.

Lumley (1978) suggested including the dissipation anisotropy in the model, so

$$\phi_{ij}^{(2)} = 2\varepsilon d_{ij} - A_3 \varepsilon b_{ij} \qquad (4\text{-}56)$$

Here

$$d_{ij} = \frac{2\nu \langle u_{i,K} u_{j,K} \rangle}{\varepsilon} - \frac{1}{3} \delta_{ij} \qquad (4\text{-}57)$$

is the anisotropy of the dissipation tensor and

$$\varepsilon = 2\nu \langle u_{i,j} u_{i,j} \rangle \tag{4-58}$$

is the dissipation. Using the dynamical equation for b_{ij}, it can be shown that A_3 must be bigger than 2. The term εd_{ij} acts to interchange energy among components of turbulent kinetic energy, but neither creates nor destroys total energy. Lumley also included a second-order anisotropy tensor in the model; however, the model (4-56) seems to work quite well for homogeneous flows (see next chapter). Lumley (1978) also argues that the proportionality constant A_3 in the model (4-56) is a function of Reynolds number and first-, second-and third-order invariants of the anisotropy tensor.

D. Pressure-Scalar Covariance

The pressure-scalar covariance, ϕ_i, is defined by Eq. (4-13). This term, which appears in the $\langle \theta u_i \rangle$ equation, is responsible for destroying the velocity-scalar correlation. Following the procedure used in the last section, we divide ϕ_i into two terms. $\phi_i^{(1)}$ involves the mean shear explicitly, and $\phi_i^{(2)}$ is the remainder.

$$\phi_i = \phi_i^{(1)} + \phi_i^{(2)} \tag{4-59}$$

Let us first consider $\phi_i^{(1)}$. From Eq. (4-13), we get

$$\phi_i^{(1)} = \langle p^{(1)} \theta_{,i} \rangle \tag{4-60}$$

From Eq. (4-45), the Fourier transform of the pressure is

$$\hat{p}_{,i} = -2\overline{U}_{q,j} \frac{k_q k_i}{k^2} \hat{u}_j \tag{4-61}$$

Let us multiply both sides by $\hat{\theta}^*$ and add to the conjugate of Eq. (4-61) multiplied by θ and integrate over Fourier space.

$$\int (\hat{p}_{,i} \hat{\theta}^* + \hat{p}_{,i} \hat{\theta}^*) \, dk = -2\overline{U}_{q_{ij}} \int \frac{k_q k_j}{k^2} (\hat{u}_j^* \hat{\theta} + \hat{u}_j \hat{\theta}^*) \, dk \tag{4-62}$$

By definition, the integral on the left is the volume average of $p_{,i}\theta$. On the other hand, in a homogeneous flow,

$$< p_{,i}\theta > \; = \; - < p\theta_{,i} > \tag{4-63}$$

Using Eqs. (4-49) and (4-52), Eq. (4-51) becomes

$$\phi_i^{(1)} \; = \; - 2\overline{U}_{q,j} \int \frac{k_q k_i}{k^2} \hat{u}_j \hat{\theta}^* \, dk \tag{4-64}$$

The integral on the right-hand side of (4-64) is a third-rank tensor. It cannot be computed analytically and needs to be modeled. Let us define $\phi_i^{(1)}$ as follows:

$$\phi_i^{(1)} \; = \; - 2\overline{U}_{q,j} g_{qij} \tag{4-65}$$

where

$$g_{qij} \; = \int \frac{k_q k_i}{k^2} \hat{u}_j \hat{\theta}^* \, dk \tag{4-66}$$

A model for g_{qij} must satisfy the following conditions:

- From continuity, $g_{qiq} = 0$.
- From the definition of g_{qij}, $g_{qqj} = < \theta u_j >$.
- From symmetry, $g_{qij} = g_{iqj}$.

By analogy to the assumptions applied to the pressure-strain model, Eq. (4.49), we assume g_{qij} is a linear function of θu_i. The following model satisfies all of the above assumptions:

$$g_{qij} \; = \; \frac{2}{5}\left[\delta_{iq} < \theta u_j > - \frac{1}{4} \; \delta_{ij} < \theta u_q > + \delta_{qj} < \theta u_i > \right] \tag{4.67}$$

Thus the model for the fast term, $\phi_i^{(1)}$, is

$$\phi_i^{(1)} \; = \; - \frac{4}{5} < U_{q,j} > \left[\delta_{iq} < \theta u_j > - \frac{1}{4} \; \delta_{ij} < \theta u_q > + \delta_{qj} < \theta u_i > \right] \tag{4-68}$$

For our case, where $\overline{U}_{q,j} = 0$, except for $\overline{U}_{1,2} = S$, the model has the following form:

$$< p^{(1)}\theta_{,1} > = 2SA_o < \theta u_2 > \tag{4-69}$$

$$< p^{(1)}\theta_{,2} > = -\frac{SA_o}{2} < \theta u_1 > \tag{4-70}$$

where $A_o = 2/5$. Comparing the above equations with Eq. (4-40), we see great similarity between the models for the hydrodynamic field and the corresponding models for the scalar field.

Lumley (1978) argues that, as $< \theta u_i > \to 0$, $\phi_i \to 0$. He constructed an expression for $\phi_i^{(1)}$, which satisfies all the above conditions:

$$\phi_i^{(1)} = -2A_o \overline{U}_{q,j} \left[\delta_{qi} - \frac{< \theta u_q > < \theta u_i >}{< \theta u_k > < \theta u_k >} \right] < \theta u_j > \tag{4-71}$$

where $A_o = 1/2$.

For our case, this model becomes

$$< p^{(1)}\theta_{,1} > = 2A_o S \frac{< \theta u_2 >^2}{< \theta u_1 >^2 + < \theta u_2 >^2} < \theta u_1 > \tag{4-72}$$

$$< p^{(1)}\theta_{,2} > = -2A_o S \frac{< \theta u_1 > < \theta u_2 >}{< \theta u_1 >^2 + < \theta u_2 >^2} < \theta u_2 > \tag{4-73}$$

Now let us consider the second part of the pressure-scalar covariance,

$$\phi_i^{(2)} = < p^{(2)}\theta_{,i} > \tag{4-74}$$

This term appears in the heat flux equation and tends to destroy the velocity-scalar correlation. The average heat flux equation in the absence of a mean scalar gradient is:

$$\frac{\partial < u_i\theta >}{\partial t} = - < p^{(2)}\theta_{,i} > - (\nu+D) < \theta_{,j} u_{i,j} > \tag{4-75}$$

Both terms on the right side of the above equation tend to destroy the $< u_j\theta >$ correlation. To model these terms, let us define ψ_{ij} by

$$- \psi_{ij} < \theta u_j > \frac{\varepsilon}{q^2} = < p^{(1)}\theta_{,i} > - < (\nu+D)\ \theta_{,k} u_{i,k} > \qquad (4\text{-}76)$$

Lumley argues that the principal axes of ψ_{ij} are aligned with the principal axes of B_{ij}, where

$$B_{ij} = \frac{< u_i u_j >}{q^2} - \frac{< \theta u_i > < \theta u_j >}{\overline{\theta^2}\ q^2} \qquad (4\text{-}77)$$

Therefore, ψ_{ij} must be a function of B_{ij}.

Assuming a linear relation, we get

$$\psi_{ij} = A_1 \delta_{ij} + A_2 B_{ij} \qquad (4\text{-}78)$$

where A_1 and A_2 are functions of anisotropy invariance.

Assuming $A_2 = 0$, the model for our flow will have the following form:

$$< p^{(2)}\theta_{,1} > - < (\nu+D)\ \theta_{,k} u_{1,k} > = A_1 \frac{\varepsilon}{q^2} < \theta u_1 > \qquad (4\text{-}79)$$

and

$$< p^{(2)}\theta_{,2} > - < (\nu+D)\ \theta_{,k} u_{2,k} > = A_1 \frac{\varepsilon}{q^2} < \theta u_2 > \qquad (4\text{-}80)$$

The above model in fact is very similar to Lumley's model for the Rotta term, Eq. (4-56).

Chapter V

DECAY OF A PASSIVE SCALAR IN HOMOGENEOUS ISOTROPIC TURBULENT FLOWS

In this chapter we present results for decay of the velocity field and a passive scalar in isotropic homogeneous flows. The decay rates, various length scales, two-point correlations, and one- and three-dimensional spectra of various terms are presented and discussed for both the hydrodynamic and scalar fields. The effects of the Reynolds and Prandtl numbers on the decay rates, microscales, and skewness are also considered. All of the results presented in this chapter were obtained using $32 \times 32 \times 32$ mesh points, so the Reynolds number range is limited to $Re_\lambda < 25$.

5.1 Results from a Typical Run

In this section, we present the results obtained for a typical run (IH32-2). This run has the following initial values:

Reynolds number $Re_\lambda = \frac{q\lambda}{\nu} = 11.00.$

Integral length scale ratio $L/L_\theta = 1.30.$

Taylor micro-scale ratio $\lambda/\lambda_\theta = 1.23.$

Integral length scale $L = 0.82.$

Taylor micro-scale $\lambda = 0.23.$

Time step $\Delta t = 0.0210.$

Computational box length $L_b = 6.28.$

Initial turbulence velocity $q = 0.02.$

Molecular Prandtl/Schmidt number $Pr = \nu/D = 1.00.$

The results are shown in Figs. 5-1 through 5-13 and discussed below.

A. The Hydrodynamic Field

Figure 5-1 shows the evolution of the three-dimensional energy spectrum. The 3-D energy spectrum is obtained by summing the energy in spherical shells of inner radius k and outer radius $k + \Delta k$, where

k is the magnitude of the wavevector and Δk is the difference between the magnitudes of the two nearest wavenumbers. As stated in Chapter II, the initial 3-D spectrum is a square wave. The 3-D spectrum evolves from the artificial square wave inertial condition to a realistic low Reynolds number energy spectrum. Since the Reynolds number is small, there is no inertial subrange. At low wavenumbers, the slope becomes 4 at long times--an expected result. The energy at wave numbers higher than 2/3 of the maximum wavenumber is set to zero to avoid aliasing.

Figure 5-2 shows the 3-D spectra of the components of the turbulent kinetic energy at the final time step. As can be seen, the flow is slightly anisotropic at low wavenumbers and isotropic at high wavenumbers. This, too, is expected, especially as there are only a few low wavenumbers.

The lateral and longitudinal one-dimensional spectra of the velocity field are shown in Fig. 5-3. The 1-D spectrum of the velocity field in the k_1 direction is defined as

$$E_{ij}(k_1) = \iint \hat{u}_i(\vec{k})\ \hat{u}_j^*(\vec{k})\ dk_2\ dk_3 \qquad (5\text{-}1)$$

As shown, velocity field is isotropic, $E_{22}(k_1) = E_{33}(k_1)$, as expected.

Figure 5-4 shows the time evolution of the turbulent kinetic energy and its three components in log-log coordinates. As can be seen, neglecting the "developing" region (defined in Chapter II), the turbulent kinetic energy is a straight line. If $e(t)$ is the turbulent kinetic energy at time t, then

$$e(t) = A\ t^{-n} \qquad (5\text{-}2)$$

where n is the decay exponent. In this particular run, $n = 2.4$. The decay of the turbulent kinetic energy has been observed in many experiments. It has been shown analytically that the exponent, n, for very low Reynolds numbers is 2.5. It has been shown both experimentally and analytically that the decay exponent for high Reynolds numbers is 1.20.

Figures 5-5 show the lateral and longitudinal two-point correlations at initial time and the final time. The two-point correlations of the velocity are defined as

$$R_{ij}(\vec{r}) = \langle u_i(\vec{x}+\vec{r})\, u_j(\vec{x}) \rangle / \langle u_i(\vec{x})\, u_j(\vec{x}) \rangle \qquad (5\text{-}3)$$

As shown in Fig. 5-5a, the initial two-point correlations oscillate sinusoidally. This is due to the narrow band nature of the initial spectrum. This effect vanishes with time.

The integral length scale, $L_{ij}(r_\ell)$, is defined as twice the distance at which $R_{ij}(r_\ell)$ first reaches 0.1. This differs from the standard definition of the integral length scale, which is the integral of the two-point correlations. However, since the two-point correlation can have negative values at large r, the standard integral length scale may behave poorly. The time evolution of the integral length scales is shown in Fig. 5-6.

The Taylor micro-scales are shown in Fig. 5-7. The Taylor micro-scale, $\lambda_{ij}(r_\ell)$, is defined as the inverse of curvature of a two-point correlation at $r = 0$. Both the integral and Taylor micro-scales increase with time. However, the integral length scales increase faster.

B. The Scalar Field

Figure 5-8 shows the time evolution of the 3-D spectrum of the scalar quantity. It is very similar to the 3-D energy spectrum. However, the scalar fluctuation spectrum is slightly higher at high wavenumbers. This is also observed experimentally for the flows with Prandtl number close to 1. It suggests that the dissipation in the velocity field is lower than dissipation in the scalar field.

The one-dimensional spectrum, two-point correlations, integral- and micro-scales of the scalar quantity are also similar to those for the velocity field. They are shown in Figs. 5-4 through 5-7, along with corresponding values for the velocity fields.

The decay of the scalar intensity $< \theta^2 >$, with time is shown in Fig. 5-9. As can be seen, its behavior is similar to that of the turbulent kinetic energy history and can be fit by:

$$< \theta^2 > = B\, t^{-m} \qquad (5\text{-}4)$$

where m is the decay exponent of the scalar and B is a constant. In this particular run, $m = 2.25$, which is within the range obtained from the experimental results. The behavior of $< \theta^2 >$, Eq. (5-4), is also observed experimentally. The magnitude of m obtained from several experimental results (see Table 1-1, also Lumley and Warhaft (1978), and Domis (1979) for more details) varies between 0.87 to 3.0, depending on the initial length/scale ratio, λ/λ_θ, and scalar intensity; the Prandtl number was 0.7. There are no experimental results for m at low Reynolds numbers or other Prandtl numbers.

5.2 Description of the Simulations

Nine simulations of isotropic homogeneous flow were made. The simulations were obtained for various Prandtl numbers and a limited range of Reynolds numbers. The initial micro- and integral-length/scale ratios for all of the runs are fixed: $\lambda/\lambda_\theta = 1.23$ and $L/L_\theta = 1.30$. Table 5-1 shows some statistics for the various runs. In this table, Re_λ in the third column is the Reynolds number at the final time step. R is the ratio of the decay exponents:

$$R = m/n \qquad (5\text{-}5)$$

The decay exponent ratio, R, is an important parameter. It is the ratio of characteristic time scales of the velocity and scalar fields:

$$R = \frac{q^2/\varepsilon}{< \theta^2 >/\varepsilon_\theta} \qquad (5\text{-}6)$$

where ε is the rate of dissipation of kinetic energy and ε_θ is half the rate of the dissipation of the scalar intensity, and is defined as

$$\varepsilon_\theta = \frac{1}{2} D \langle \theta_{,j} \theta_{,j} \rangle \qquad (5\text{-}7)$$

In the following section we shall discuss the effects of Reynolds and Prandtl numbers on the decay-rate exponents.

5.3 Effects of Reynolds and Prandtl Numbers on Some Turbulence Statistics

As explained in the previous section, flow fields at various Reynolds and Prandtl numbers were generated. In this section we examine the behavior of the various turbulence statistics.

A. The Length Scale Ratio

Figure 5-10 shows the behavior of the microscale ratio, λ/λ_θ, as a function of Reynolds number for various Prandtl numbers. As can be seen, the microscale ratio increases with Re_λ when $Pr < 1$, and it decreases with Re_λ when $Pr > 1$. On the other hand, at high Reynolds numbers, the length scale ratio is independent of Prandtl numbers. Ironically, as $Re_\lambda \to 0$, the length scale ratio reaches a constant. This constant depends on the Prandtl number.

B. The Decay Rate

Figure 5-11 shows the decay exponent n vs. Reynolds number. As can be seen, at very low Reynolds numbers n reaches 2.5. This has been shown analytically (see Batchelor (1948)). As the Reynolds number increases, the decay exponent n decreases. At high Reynolds numbers, however, it reaches an asymptotic value. W. C. Reynolds (1976) argues that the asymptotic value is 1.2. The experimental values for n at high Reynolds numbers, obtained by Warhaft and Lumley (1978) and Comte-Bellot and Corrsin (1971), is 1.25 ± 0.06. As shown in Fig. 5-11, the experimental value for n obtained from Tavoularis et al. (1978) is very close to our simulated results. The Bennett and Corrsin (1978) result, however, does not agree with our results. This may be due to the difference in origin of the decay rate.

C. The Decay Rate Exponent Ratio

The decay exponent ratio, R, defined by Eq. (5-5), is shown in Fig. 5-12 as a function of Reynolds number for various Prandtl numbers. As can be seen from the figure, R increases with Reynolds number at $Pr < 1$, and it decreases with Reynolds number at $Pr > 1$. At high Reynolds number, R asymptotically reaches a constant. This constant depends on the Prandtl number. As $Re_\lambda \to 0$, however, it seems that the decay exponent ratio reaches a constant. This constant is independent of Prandtl number.

D. The Velocity Derivative of Skewness

Velocity derivative skewness is defined by Eq. (3-2). Figure 5-13 shows the skewness vs. Reynolds number. The results shown in this figure were obtained from a $16 \times 16 \times 16$ mesh point code and various numerical and experimental results. As can be seen, skewness has a maximum value of approximately 0.5 at $Re_\lambda = 20$. For $Re_\lambda > 20$, skewness decreases and it seems to reach a constant at about $Re_\lambda = 100$. At low Reynolds numbers ($Re_\lambda < 20$), the skewness decreases and $Sk \to 0$ as $Re_\lambda \to 0$.

Table 5-1

DESCRIPTION OF COMPUTER RUNS FOR DECAY OF A PASSIVE SCALAR IN ISOTROPIC HOMOGENEOUS TURBULENT FLOWS

Simulations	$(Re_\lambda)_o^*$	Re_λ	Pr	$\lambda_u/\lambda_\theta^{**}$	n	m	r
IH32-2A	11.00	3.00	0.20	0.634	2.40	3.00	1.25
IH32-3A	22.30	10.00	0.20	0.703	1.70	3.00	1.76
IH32-4A	44.40	22.00	0.20	0.830	1.50	2.90	1.93
IH32-2	11.00	3.00	1.00	1.27	2.40	2.25	0.94
IH32-3	22.30	10.00	1.00	1.23	1.70	1.70	1.00
IH32-4	44.40	22.00	1.00	1.19	1.50	1.61	1.07
IH42-2B	11.00	3.00	5.00	1.68	2.40	0.75	0.31
IH32-3B	22.30	10.00	5.00	1.40	1.70	0.50	0.29
IH32-4B	44.40	22.00	5.00	1.26	1.50	0.34	0.23

*$(Re_\lambda)_o$ is the initial turbulent Reynolds number.

**The initial microscale ratio for all of the flow fields is the same, and its value is $(\lambda_u/\lambda_\theta)_o = 1.23$. The initial lateral integral length scale ratio for all flow fields is $(Lu/L_\theta)_o = 1.30$.

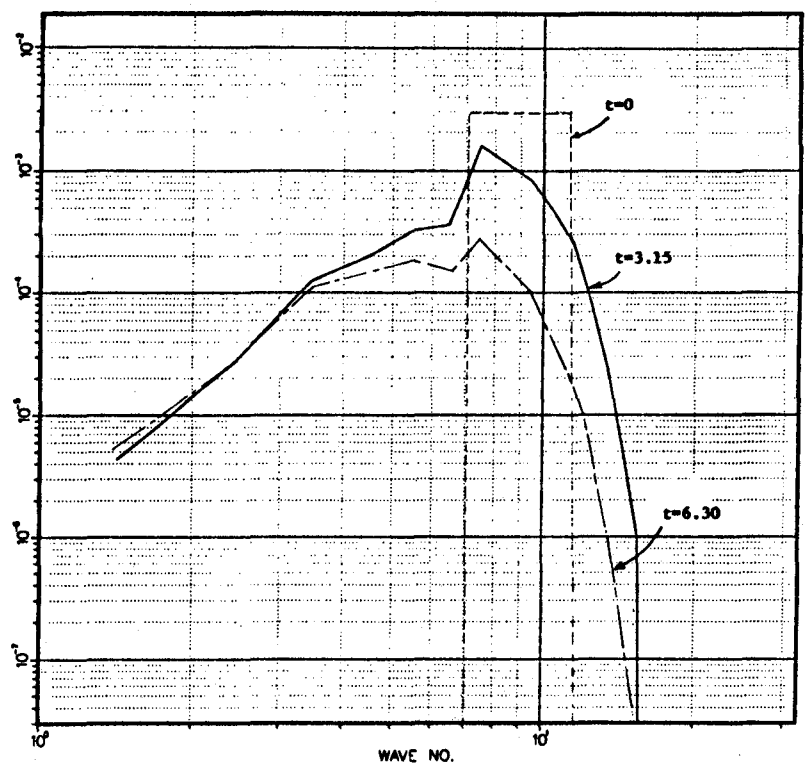

Fig. 5-1. Three-dimensional energy spectra at three different times.

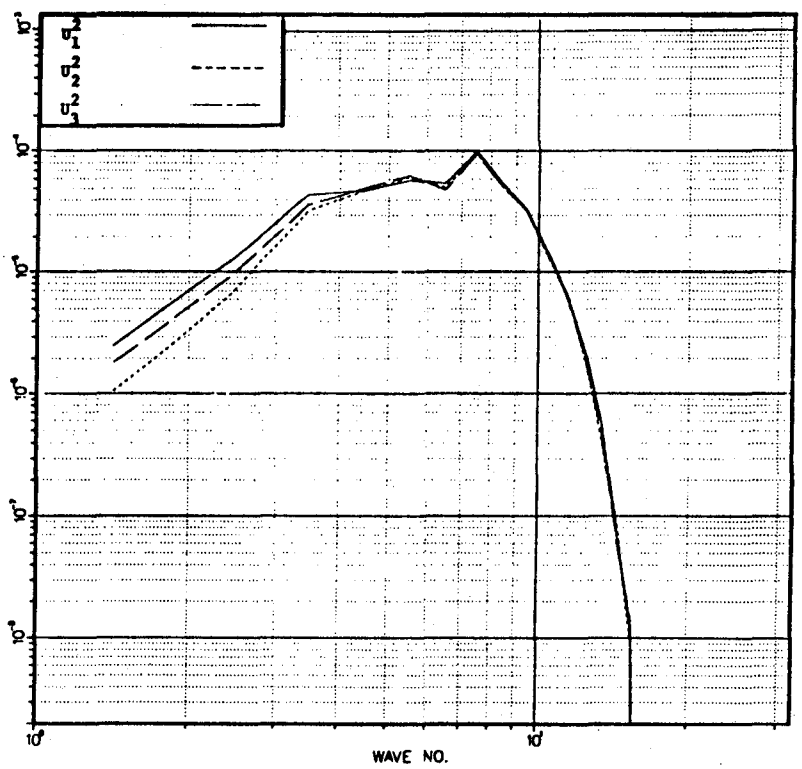

Fig. 5-2. Three-dimensional spectra of the turbulent kinetic energy components at St = 4.0.

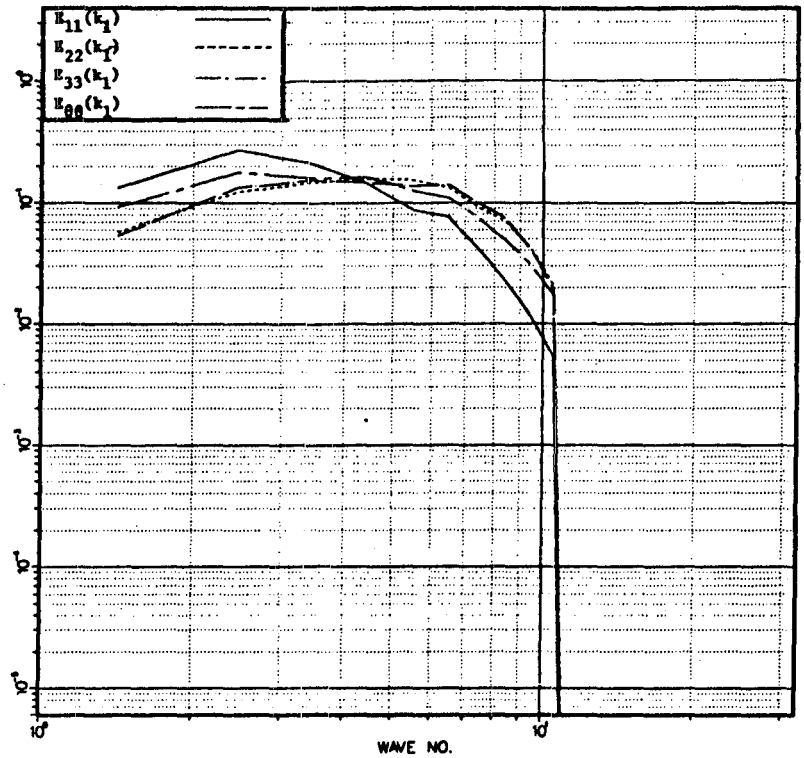

Fig. 5-3. One-dimensional spectra of the velocity components and scalar fluctuations at St = 4.0.

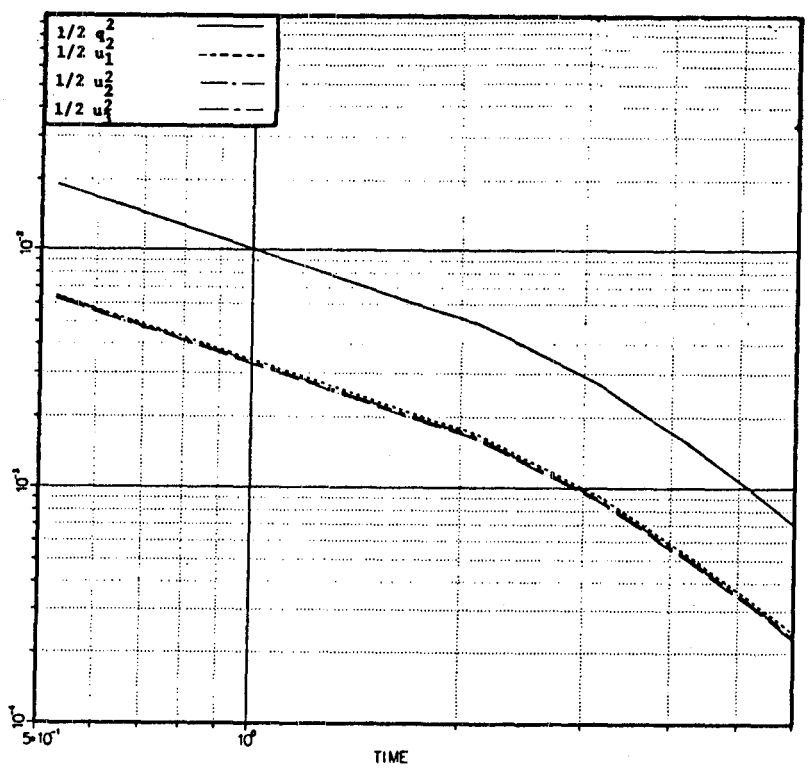

Fig. 5-4. Decay of the turbulent kinetic energy and its components with time.

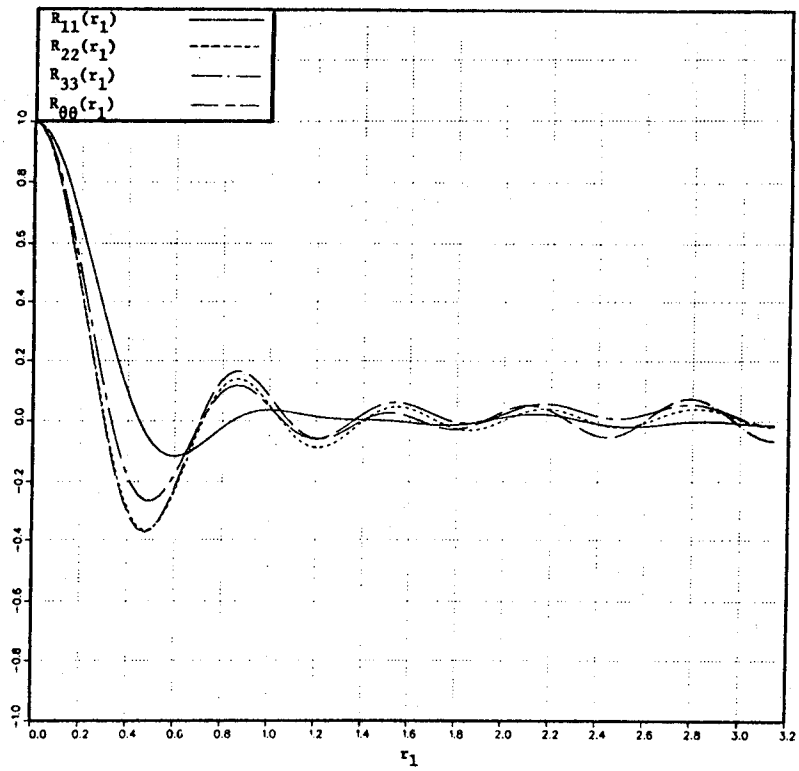

Fig. 5-5 (a) Two-point correlations of velocity components and the scalar fluctuations at St = 0.0.

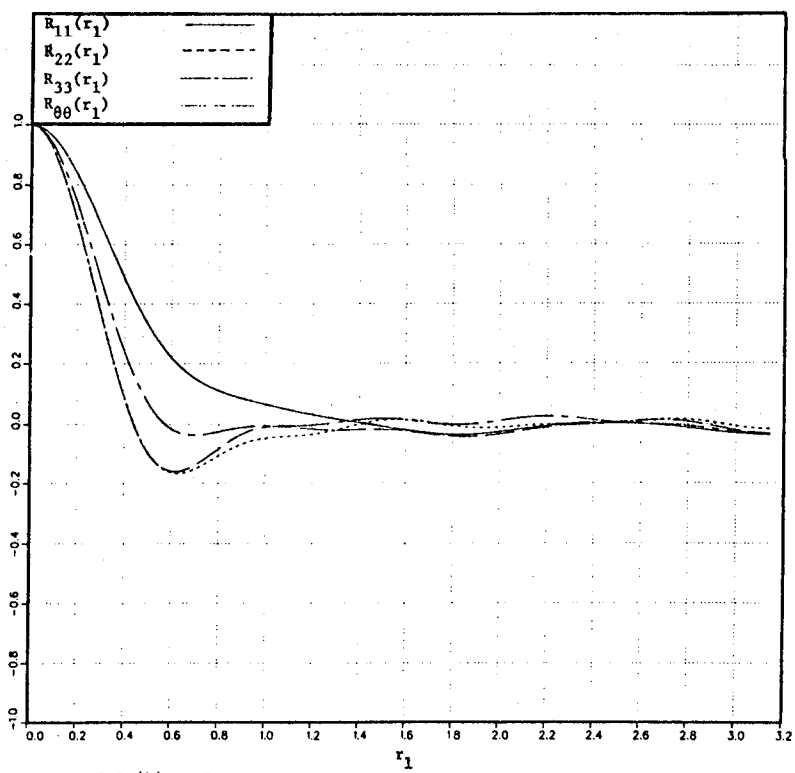

5-5 (b) Two-point correlations of velocity components and the scalar fluctuations at St = 4.0.

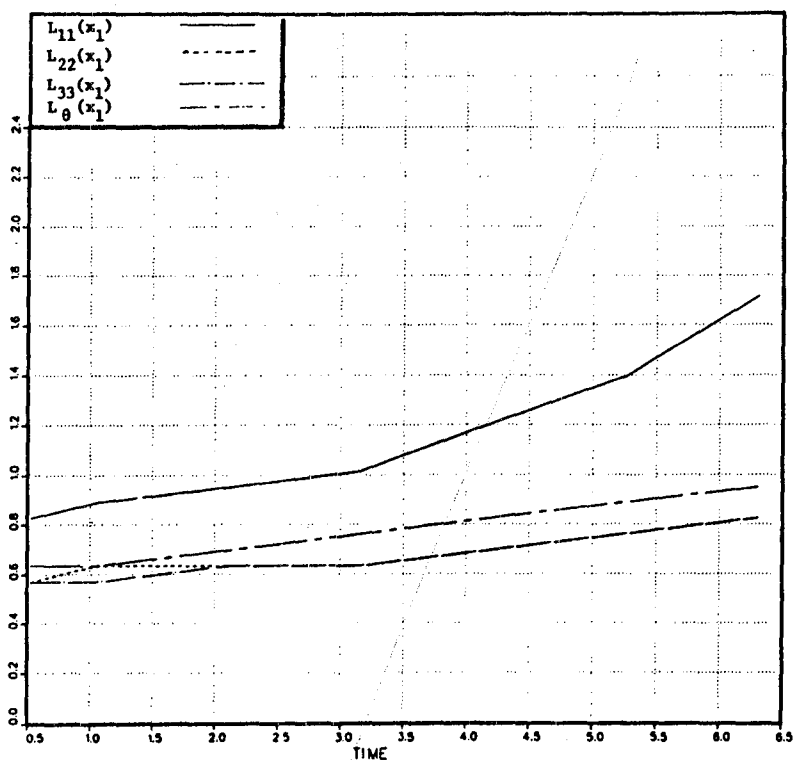

Fig. 5-6. Time evolution of the integral lenyth scales of velocity and scalar fields.

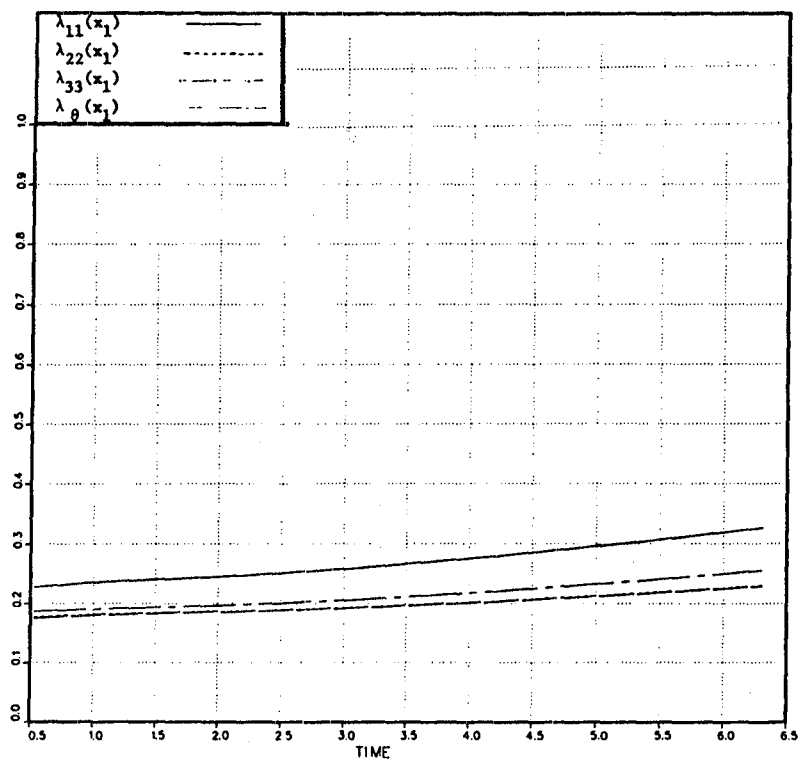

Fig. 5-7. Time evolution of the Taylor microscale of the velocity and scalar fields.

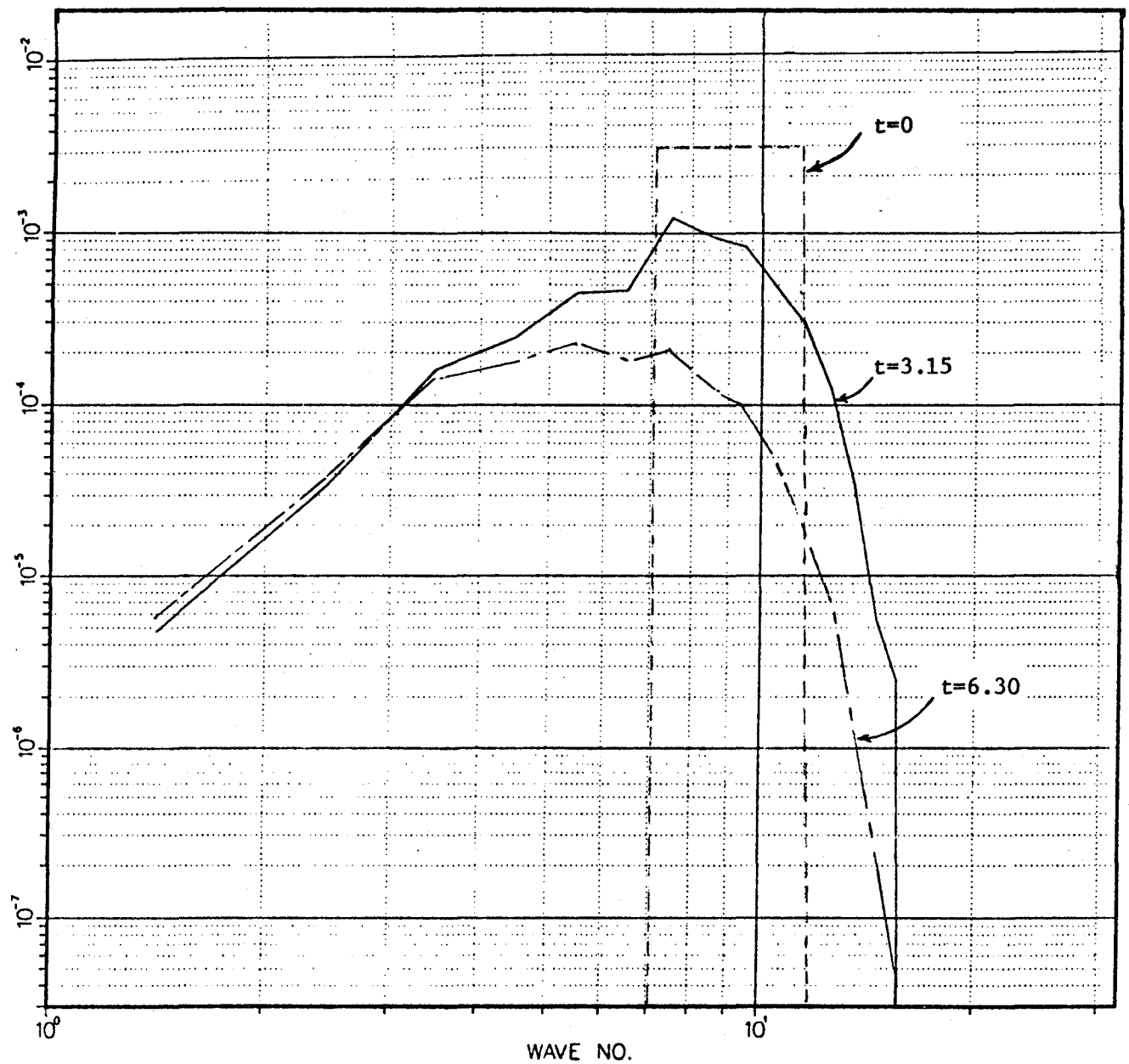

Fig. 5-8. The 3-D spectra of scalar quantity at various times.

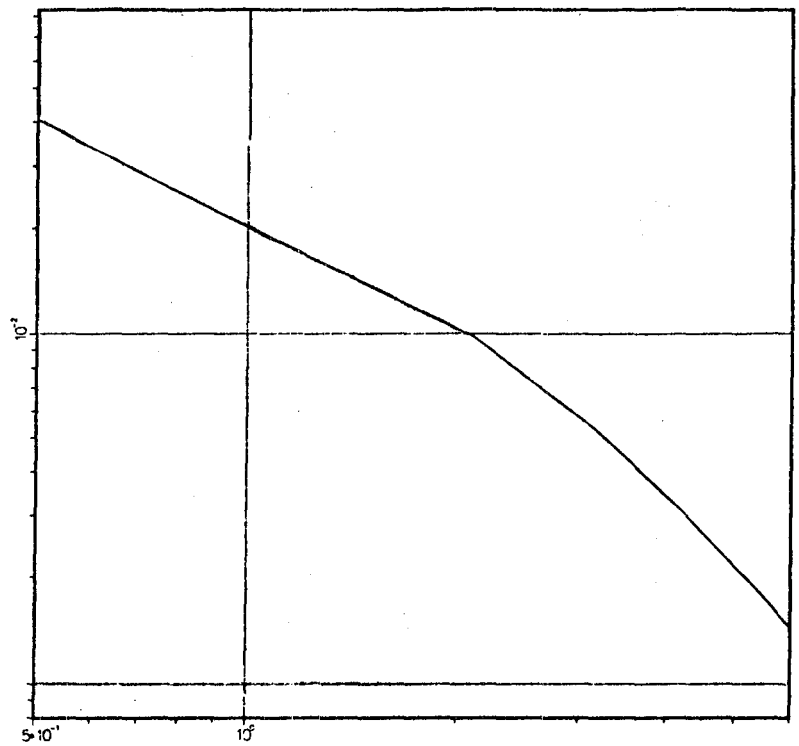

Fig. 5-9. Decay of scalar intensity as a function of time.

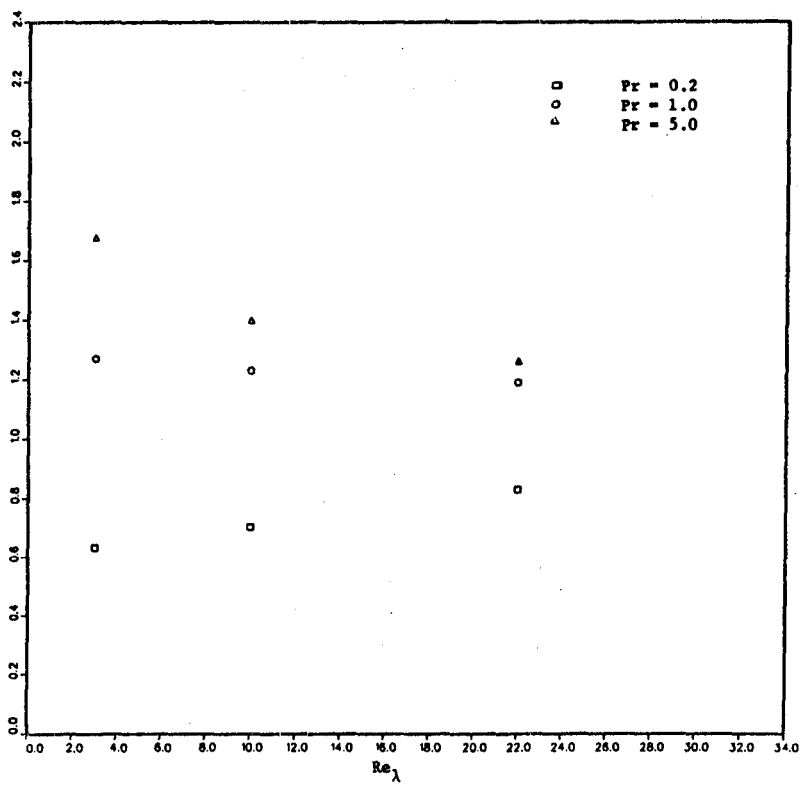

Fig. 5-10. Taylor microscale ratio as a function of Reynolds number for various Prandtl numbers.

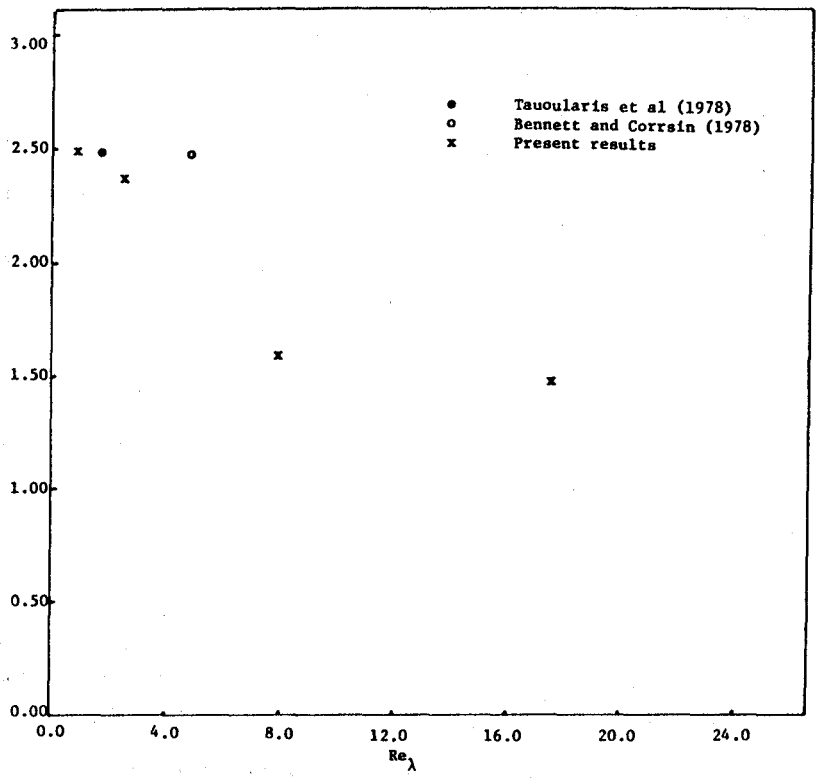

Fig. 5-11. Decay exponent of turbulent kinetic energy as a function of Reynolds number.

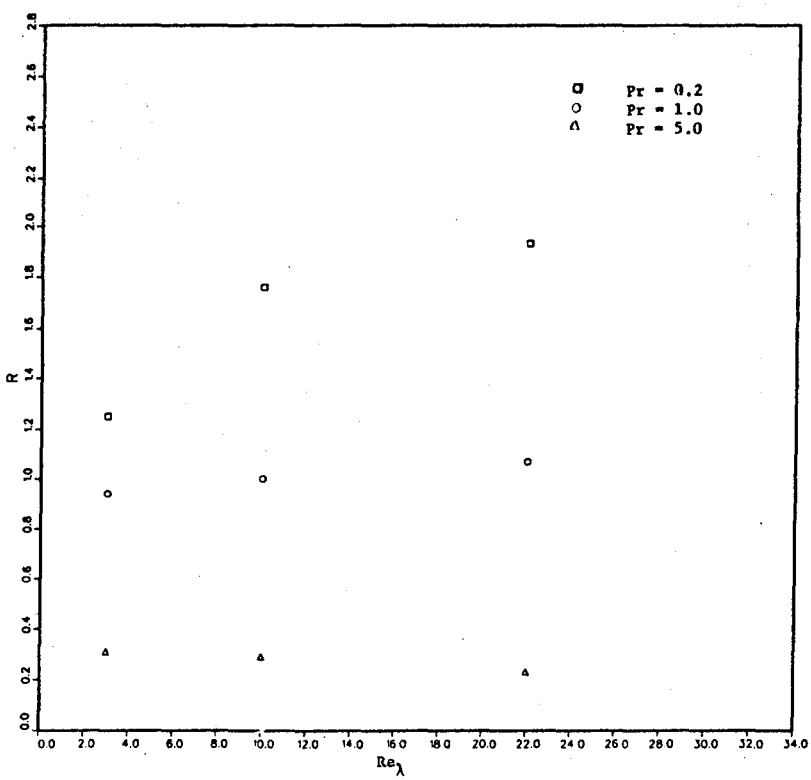

Fig. 5-12. Decay exponent ratio as a function of Reynolds number for various Prandtl numbers.

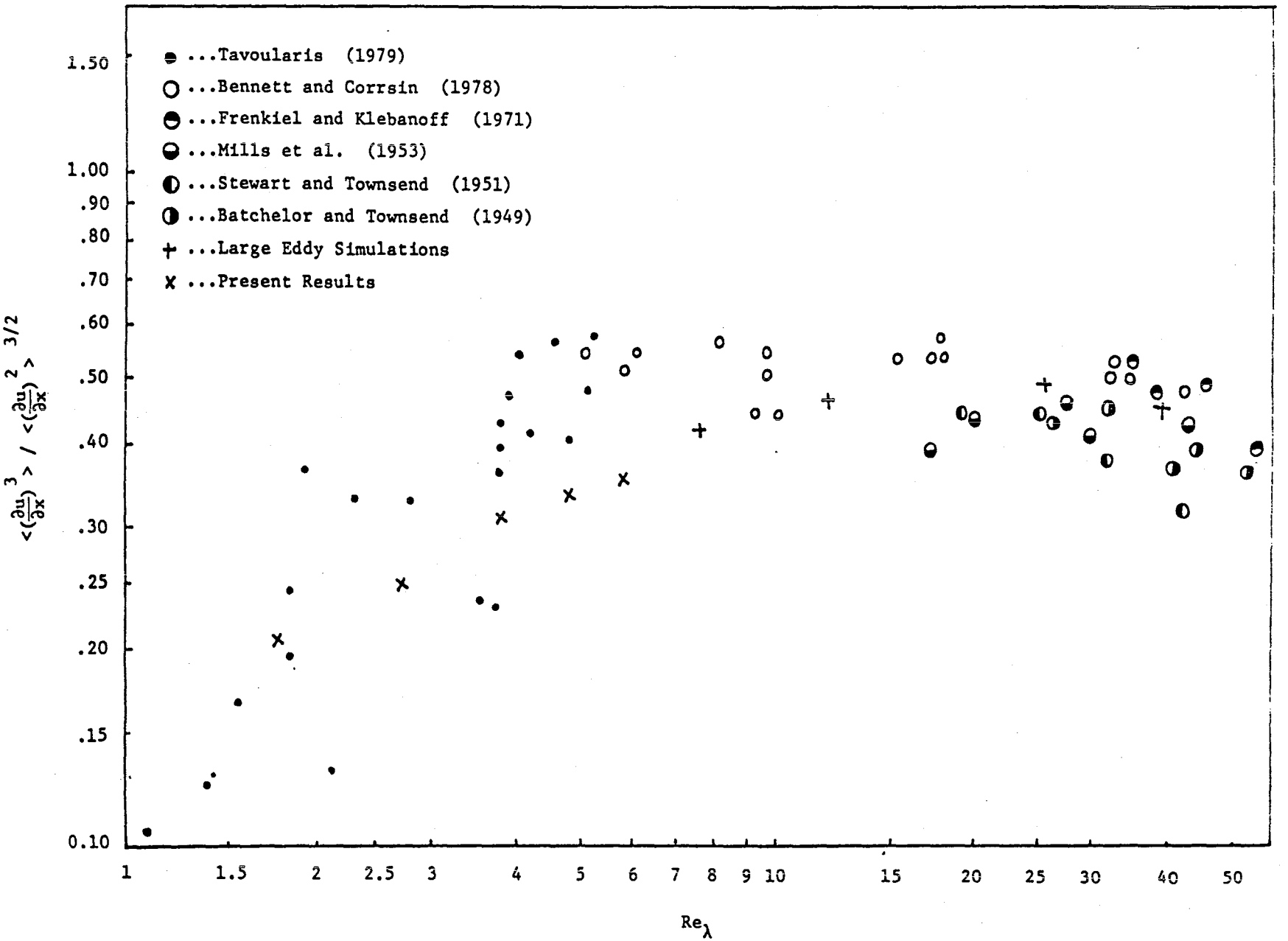

Fig. 5-13. Velocity skewness as a function of Reynolds number.

Chapter VI

RESULTS FOR HOMOGENEOUS TURBULENT SHEAR FLOWS WITH A MEAN GRADIENT OF A PASSIVE SCALAR

In this chapter the results for both the velocity and the scalar flows in a homogeneous turbulent shear flow with a passive scalar, whose mean is linear, are presented and discussed. Six velocity and fourteen scalar fields were generated. The flow fields are obtained for various Reynolds, Prandtl, and shear numbers. In this chapter a complete set of results for one of the simulated flows is presented. Also, the effects of the parameters on various turbulence statistics are discussed and models for Reynolds stress, heat/mass flux, pressure-strain, and pressure-scalar covariances are tested and their validity is discussed.

6.1 Dimensional and Non-Dimensional Parameters

The important dimensional parameters of this flow are presented in Tables 6-1 and 6-2. The dimension of the scalar, Θ, in Table 6-2, is (a) degrees if the scalar is temperature and (b) mass if the scalar is species. The integral and microscales are defined in the previous chapter.

From the parameters in the tables, the following nondimensional parameters can be formed:

$Re = q\lambda/\nu$, Reynolds number.

$\mathcal{S} = SL/q$, shear number.

$Pr = \nu/D$, Prandtl number.

$\mathcal{S}_{\theta_2} = \theta'/S_2L$, nondimensional scalar fluctuations.

L/L_θ = length scale ratio.

St = nondimensional time.

Note that L/λ depends on Reynolds number and therefore is not included above. The shear number $\mathcal{S}$ can be written as

$$\mathcal{S} = \frac{L/q}{1/S} \qquad (6\text{-}1)$$

which is the ratio of the time scales of the large scale structures and the mean flow. Assuming $L = q^3/\varepsilon$, $\mathscr{S}$ can be written in the following form:

$$\mathscr{S} = \frac{Sq^2}{\varepsilon} \tag{6-2}$$

which is proportional to the ratio of the production to dissipation of turbulent kinetic energy.

The parameter $\mathscr{S}_{\theta 2}$ is analogous to the inverse of $\mathscr{S}$. It is approximately the ratio of the production to dissipation of the scalar fluctuations.

Some of the nondimensional parameters mentioned above are related through the dynamics of the flow, that is, they are not independent. The results obtained from a set of $32 \times 32 \times 32$ mesh point computer runs show that the length scale ratio, L/L_θ, and the nondimensional scalar quantity, $\mathscr{S}_{\theta 2}$, are dependent parameters. Figure 6-1 shows $\mathscr{S}_{\theta 2}$ as a function of time for four different runs. The initial Reynolds, shear, and Prandtl numbers and length scale ratios are the same for all runs, but the initial $\mathscr{S}_{\theta 2}$ is changed from one run to another. As shown in the figure, the final value of $\mathscr{S}_{\theta 2}$ is independent of its initial value. In other words, $\mathscr{S}_{\theta 2}$ is a function of Reynolds, shear, and Prandtl numbers, i.e., a dependent parameter.

Similarly, as shown in Fig. 6-2, the final value of the length scale ratio L/L_θ is independent of its initial value, i.e., L/L_θ is a dependent parameter. Therefore, the only nondimensional parameters we need to deal with are Reynolds, shear, and Prandtl numbers. The scalar field is determined by the velocity field and the Prandtl number.

6.2 Description of the Simulations

Six simulations of the hydrodynamic field and fourteen simulations of the scalar field have been performed. All of the simulations used $64 \times 64 \times 64$ mesh points. The results presented in the rest of this chapter are from these simulations.

As discussed in Chapter III, the simulations use an artificial initial field. There is also a time at which the turbulent structures become large compared to the size of the computational domain, and the periodic boundary conditions no longer hold. The results are not acceptable after that time. According to the criteria mentioned in Chapter III, the period in which the data are acceptable lies between $St = 4$ and $St = 7$ for all of the simulations.

The simulated flow fields are stored on tape, and the turbulence statistics are calculated only when St is an integer. This is done mainly because, when St is an integer, the coordinate is Cartesian and the calculations of the turbulence statistics involving derivatives are easier.

Thus, four flow fields (at $St = 4$, 5, 6, and 7) are available from each simulation. Consequently, a total of 24 hydrodynamic fields and 56 scalar fields are available. The available flow fields cover a rather large range of Reynolds, shear, and Prandtl numbers. Table 6-3 shows the range of these nondimensional parameters in our simulations and from the available experimental results.

As can be seen from the table, the range of Reynolds number covered is lower than the available experimental values. We are limited to low Re_λ because there is a maximum Re_λ beyond which we are not able to resolve the full range of scales of turbulence. As will be shown in the following sections, we are mainly interested in turbulence statistics which depend on the large structures and which may be only weakly Reynolds number dependent, so the Reynolds number limitation may not be very serious. This will become clear in later sections, where we compare our low Reynolds number results with the experimental results.

As can be seen from Table 6-3, we have covered a rather large range of the shear number. Near the upper limit the nonlinear and viscous terms in the Navier-Stokes equations (Eq. (2-18)) become negligible, and one can apply rapid distortion theory. At lower values of the shear number, the flow becomes isotropic (the results for this case are discussed in the previous chapter).

The only available experimental data for the scalar field, obtained for $Pr = 0.7$, were taken by Tavoularis and Corrsin (1978). We have covered a significant range of Prandtl number (from 0.2 to 5.0).

At very high Prandtl numbers ($Pr \gg 1$), the diffusion equation (2-20) becomes:

$$\frac{\partial \theta}{\partial t} + \frac{\partial u_j \theta}{\partial x_j} = 0 \qquad (6\text{-}4)$$

Therefore, the results are independent of Prandtl number (we assume viscosity is fixed). On the other hand, for very low Prandtl numbers ($Pr \ll 1$), the effect of shear becomes negligible and the diffusion equation is

$$\frac{\partial \theta}{\partial t} = D \frac{\partial^2 \theta}{\partial x_j \partial x_j} \qquad (6\text{-}5)$$

and the results are discussed in the previous chapter.

For the region between these two extremes, where $Pr \approx 1$, there is no analytical solution. The effect of the Prandtl number on the various turbulence statistics in this region is studied and discussed, using our simulated results, in the following sections.

Table 6-4 shows the nondimensional parameters for each simulation in the "developed" region. In Appendix C, we have provided a set of tables which give the raw data and various turbulence statistics from each simulation. These tables may be helpful to the readers in further investigations.

6.3 Complete Results for a Typical Simulation

In this section, we present the results obtained for a typical run (Run HS64J), which has the following initial values:

Reynolds number $Re_\lambda = 20.00.$

Shear number $\mathcal{S} = 3.30.$

Nondimensional scalar fluctuation $\mathcal{S}_{\theta 2}^{-1} = 3.20.$

Prandtl number $Pr = 1.00.$

Integral length scale ratio $L/L_\theta = 1.40$.

Taylor microscale ratio $\lambda/\lambda_\theta = 1.29$.

Integral length scale $L = 0.71$.

Taylor micro-scale $\lambda = 0.22$.

The above values are non-dimensionalized, as explained in Section 2.3. The results will be discussed for both hydrodynamic and scalar fields in the following sections.

A. The Hydrodynamic Field

A-1. Three-Dimensional Energy Spectrum

Figure 6-3 shows the evolution of the three-dimensional energy spectrum. The initial 3-D energy spectrum is a square wave. At a later time, the 3-D energy spectrum has a slope of 4 at low wavenumbers, as expected. No inertial subrange with slope of -5/3 appears in the 3-D energy spectrum because the Reynolds number is low. Figure 6-4 shows the 3-D spectra of the three components of the turbulent kinetic energy at $St = 4$. As can be seen, there are anisotropy effects at low and moderate wavenumbers. The 3-D spectrum of u_2^2 has more energy at low wavenumbers and less at moderate wavenumbers, whereas u_1^2 has more energy at moderate wavenumbers and less at low wavenumbers. These are effects of the applied shear.

A-2. Turbulent Kinetic Energy History

The time evolution of turbulent kinetic energy and its three components are shown in Fig. 6-5. At $St = 0$, the flow field is nearly isotropic. At later times, however, the flow becomes anisotropic. The streamwise component of the kinetic energy becomes the largest while the normal component is the smallest. This is also observed experimentally in both homogeneous shear flows (Champagne et al. (1970) and Harris et al. (1976)) and boundary layers (Klebanoff (1955), Bradshaw (1967)).

As shown in Fig. 6-5, the turbulent kinetic energy first decreases with time and then increases. This is because the production of turbulent kinetic energy is small at early times. The production increases

with time, and there is a time after which the production is larger than the dissipation and the energy begins to grow. This effect can be seen from the experimental results obtained by Harris et al. (1976) and Tavoularis (1979). The experimental results obtained by Champagne et al. (1970) and Rose (1970), however, do not show the increase in the turbulent kinetic energy. Their measurements did not go far enough downstream.

From our computed results and the experimental results of Tavoularis (1979), the flow fields seem to be going toward some kind of structural equilibrium. Statistical equilibrium is a state in which the components of the Reynolds stress anisotropy tensor, b_{ij}, reach asymptotic values. As noted before, we were able to carry out the simulations only up to $St = 7$ and did not reach an equilibrium region. Rogallo (1981) simulated this flow with $128 \times 128 \times 128$ mesh points. He was able to continue the computation to $St = 16$ and found that the rate of change of components of b_{ij} with time decreases, but it does not become zero.

A-3. Length Scales

Figures 6-6 and 6-7 show the evolution of integral and Taylor microscales in the streamwise direction, respectively. The length scales were obtained from the two-point correlations in the manner explained in the previous chapter. Figure 6-8 shows the Kolmogorov scale, the mixing-length scales, and the transfer (or dissipation) length scale, where the Kolmogorov length scale, η, is defined by Eq. (2-1) and the mixing length is defined as

$$L_m = \frac{\sqrt{\langle u_1 u_2 \rangle}}{\partial \bar{U}/\partial x_2} \tag{6-6}$$

and the transfer length scale, L_{tr}, is defined as

$$L_{tr} = q^3/\varepsilon \tag{6-7}$$

As can be seen, all length scales increase with time. As shown in the figure, the mixing length is nearly constant, while L_d and η

increase with time. The Kolmogorov length scale is the smallest, and transfer length scale is the largest length scale. Thus the mixing length cannot be correlated with any of the other length scales.

A-4. Two-Point Correlations

Figures 6-9 through 6-11 show the two-point correlations of the velocity (Eq. (5-3)) in the streamwise direction at three different times. As can be seen, the two-point velocity correlations, $R_{ij}(r)$, at $St = 0$, are nearly zero at large r, i.e., there exist only small eddies in the computational box. However, at later times, the results show that the velocities become well correlated in the computational box. As discussed before, there is a time after which the large eddies become comparable with the box length (in other words, $R_{ij}(r)$ becomes large at large r), and the computation has to be stopped. In most of our results, $R_{ij}(r)$ is less than 0.3 at $r = L_b/2$ at the end of the computation, where L_b is the computational box length.

A-5. One-Dimensional Spectra

Figures 6-12 through 6-14 show the 1-D spectra of the velocity components in three directions. The difference between the three components of the velocity spectra show the anisotropy at various eddy sizes. As can be seen, even at high wavenumbers the three components are different, i.e., the small scales are anisotropic. This may be because the Reynolds number is low. The anisotropy at high wavenumbers will be discussed in more detail in Section 6-5D. The fluctuations of the spectra at the low wavenumbers are due to the small number of samples at which spectra are calculated.

A-6. Three-Dimensional Pressure Spectrum

As discussed in Section 4-2C, the pressure consists of two parts. $p^{(1)}$ is proportional to the mean shear, while $p^{(2)}$ does not depend explicitly on the mean flow. Figures 6-15 and 6-16 show the 3-D spectra of each component, as well as the 3-D spectrum of the total pressure at various times. Understanding the behavior of each component helps in modeling the pressure-strain and pressure-scalar covariances. As shown

in Fig. 6-16, $p^{(1)}$ is larger at low wavenumbers, i.e., it depends mainly on the large scale structures. On the other hand, $p^{(2)}$ is larger at high wavenumbers, i.e., it depends mainly on the small scale structures. We also see that the 3-D spectrum of $p^{(1)}$ has a slope of -5 at high wavenumbers. This is observed in all of the simulated flow fields. Also, the k^{-5} part of the spectrum is observed to become more important with time; the peak in the spectrum moves upward and to the left as time goes on.

A-7. One-Point Correlations

The one-point correlations of the velocities are defined as

$$C_{ij} = \frac{< u_i u_j >}{u_i' u_j'} \quad \text{(no summation)} \tag{6-8}$$

Note that $C_{ii} = 1$. Figure 6-17 shows the one-point velocity correlations as a function of time. The only non-zero component for $(i \neq j)$ is $< u_1 u_2 > / u_1' u_2'$, which starts from zero and reaches an asymptotic value of about -0.6. Similar values were obtained from computed flow fields by Feiereisen (1981) and Rogallo (1981). The experimental value lies between -0.4 and -0.5. The reason for this difference may be the Reynolds number difference between the computed and the experimental results.

The one-point correlation, C_{12} is Reynolds number dependent, because $< u_1 u_2 >$ depends mainly on the large scale structures and is therefore not strongly Reynolds number dependent, whereas u_1' and u_2' depend on both the large and small scales and are thus more Reynolds number dependent. Therefore, as the Reynolds number decreases, $< u_1 u_2 > / u_1' u_2'$ increases. The effect of Reynolds number on this quantity is given later in this chapter.

A-8. Reynolds Stress Anisotropy Tensor

The Reynolds stress anisotropy tensor, b_{ij}, is defined by Eq. (4-44). Figure 6-18 shows b_{ij} as a function of time. If the components of b_{ij} reach asymptotic values, the flow has reached structural equilibrium. As shown in the figure, b_{ij} start from zero, indicating

that the initial velocity field is isotropic, and change with time. At early times the b_{ij} change rapidly; later, however, the variation of b_{ij} is smaller. It seems that the flow might reach a state of equilibrium if the computation were continued.

A-9. Dynamical Reynolds Stress Equations

The volume-averaged equations for the Reynolds stress, $\langle u_i u_j \rangle$, are given by Eqs. (4-3)-(4-5) and (4-10) and discussed in Chapter IV. The equations contain production, pressure-strain, and dissipation terms. Transfer terms do not appear in these equations because the volume averages of these terms are zero. Figures 6-19 through 6-22 show the values of each term in the various stress equations as a function of time. As can be seen, the pressure-strain term is negative in the $\langle u_1^2 \rangle$ equation and positive in the equations for the other components of the Reynolds stress. That is, energy is transferred from $\langle u_1^2 \rangle$ to the other components of $\langle u_i u_j \rangle$ through the action of the pressure-strain terms.

Figure 6-23 shows the terms in the volume-averaged turbulent kinetic energy equation (4-8). No pressure-strain term appears in this figure because, by continuity, $\langle p \frac{\partial u_i}{\partial x_i} \rangle$ is zero.

Figures 6-24 through 6-28 show three-dimensional spectra of various terms in $\langle u_i u_j \rangle$ equations at $St = 4$. The production and pressure-strain terms are concentrated on the large scales, whereas the dissipation terms mainly come from the small scales, as expected. As can be seen in Fig. 6-25, unlike its behavior in the other equations, the pressure-strain term, $\langle p \frac{\partial u_2}{\partial x_2} \rangle$, in the $\langle u_2^2 \rangle$ equation is not only a source term but it acts as a transfer term, too. That is, $\langle p \frac{\partial u_2}{\partial x_2} \rangle$ takes energy from moderate-sized eddies and transfers it to the small and large eddies.

The transfer terms have the following form:

$$T_{ij} = u_i \frac{\partial u_j u_k}{\partial x_k} + u_j \frac{\partial u_i u_k}{\partial x_k} \qquad (6\text{-}9)$$

The 3-D spectrum of T_{ij} is defined by

$$\hat{T}_{ij} = \hat{u}_i \left(\frac{\partial u_j u_k}{\partial x_k}\right)^* + \hat{u}_i^* \left(\frac{\partial u_j u_k}{\partial x_k}\right) + \hat{u}_j \left(\frac{\partial u_i u_k}{\partial x_k}\right)^* + \hat{u}_j^* \left(\frac{\partial u_i u_k}{\partial x_k}\right) \qquad (6\text{-}10)$$

As can be seen from Figs. 6-24 through 6-28, the transfer term transfers energy from both small and large scales to the medium-sized eddies, except for the transfer term in the $< u_2^2 >$ equation, which transfers energy from large eddies to the small eddies. These effects, which are somewhat surprising, have been observed in all the calculated flow fields. McMillan and Ferziger (1978) have also found that the transfer term is negative at high wavenumbers when the shear is high. These results were obtained at high Reynolds numbers.

A-10. The Dissipation Anisotropy Tensor

The dissipation anisotropy tensor, d_{ij}, is defined by Eq. (4-47). Figure 6-29 shows d_{ij} as a function of time. It has generally been assumed that the small scales in turbulent flows are isotropic, i.e., the dissipation anisotropy is nearly zero. However, as can be seen, the components of d_{ij} start from zero and vary with time. d_{11} increases while d_{22} decreases in the developing region. It also can be seen that d_{33} is an order of magnitude smaller than the other components and is therefore not significant. Furthermore, as we shall see later, d_{ij} seems not to be very Reynolds number dependent, and this result is of considerable significance in turbulence modeling. Also note that the dissipation anisotropy is very similar to the Reynold stress anisotropy (Fig. 6.18); its components behave in the same way with time.

B. The Scalar Field

The length scales, two point-correlations, and one-dimensional spectra of the scalar fluctuations behave in a manner similar to those of the velocity field. They are shown in Figs. 6-7 through 6-14. From the two-point correlations and the 1-D spectra of the scalar and velocity fields, it can be seen that the scalar quantity behaves very much like the streamwise velocity.

The time evolution of the 3-D spectrum of the scalar fluctuations is shown in Fig. 6-30. As can be seen from the figure, the behavior of the 3-D spectrum of the scalar quantity is similar to that of the 3-D energy spectrum. The scalar-fluctuation intensity as a function of time is shown in Fig. 6-31. The scalar intensity increases with time in the developed region. Its behavior with time is similar to the behavior of $\langle u_1^2 \rangle$, i.e., they both increase at the same rate in the "developed" region.

The one-point velocity-scalar correlations as a function of time are shown in Fig. 6-32. As can be seen, there are two non-zero components:

$$\frac{\langle \theta u_1 \rangle}{\theta' u_1'} \quad \text{and} \quad \frac{\langle \theta u_2 \rangle}{\theta' u_2'}$$

This suggests that there are heat/mass fluxes in both the streamwise and normal directions. The one-point correlation with the streamwise velocity reaches a value of 0.75. The experimental value for this term, which was obtained by Tavoularis (1979), is about 0.6. The one-point correlation for the normal direction reaches a value of -0.52; the corresponding experimental value is -0.4. The difference between our computed results and the experimental results for these terms is probably due to the Reynolds number difference, as discussed in Section 3A-7 of this chapter.

As can be seen from Fig. 6-32, the streamwise velocity and the scalar quantity are well correlated. This is consistent with the Prandtl mixing-length theory, which is based on the assumption that the streamwise velocity component acts as a scalar which is transported vertically.

The volume-averaged equations for the scalar intensity and the heat/mass flux are given by Eqs. (4-9), (4-11), and (4-12) and are discussed in Chapter IV. Figures 6-33 through 6-35 show the time evolution of each term in these equations. As can be seen, the pressure-scalar covariances for both $\langle \theta u_1 \rangle$ and $\langle \theta u_2 \rangle$ equations are such that they tend to destroy the correlations. This effect is similar to that of the analogous terms in the Reynolds shear stress, $\langle u_1 u_2 \rangle$, equation.

Figures 6-36 and 6-37 show the 3-D spectra of each term in the θ^2 and θu_2 equations. The transfer terms behave in a manner similar to that of the transfer term in the $u_1 u_2$ equation.

6.4 Statistics of the Velocity Fields and Models

As stated above, 24 velocity fields were produced at various Reynolds and shear numbers. In this section, the effects of these nondimensional parameters on various turbulence statistics will be tested and their validity will be examined. To do this, we use a power law of the nondimensional parameters to fit the data. The accuracy of the fit can be judged by r.m.s. relative error obtained from the simulated data and the power law.

A. Reynolds Stress Tensor

The values of the Reynolds stress tensor components, $< u_i u_j >$, are given in Appendix C. Their behavior is particularly important, because they appear in the mean momentum equations and are modeled most often.

The angle of the principal axis of the Reynolds stress tensor relative to the computational coordinate system (cf. Eq. (4-17) is given in Table 6-5. As can be seen, the principal axis angle varies between 11.5 and 26 degrees, depending on the shear and Reynolds numbers. The behavior of this angle as a function of the Reynolds and shear number is shown in Figs. 6-38 and 6-39, respectively. As shown in these figures, the principal axis angle is Reynolds- and shear-number dependent. It decreases with both Re_λ and $\mathcal{A}$. At high Reynolds numbers, however, the angle seems to reach an asymptotic value. This value is shear number dependent.

The most common model for $< u_i u_j >$ is based on the Boussinesq eddy-viscosity concept, Eq. (4-21), i.e., $< u_i u_j >$ is proportional to the mean shear. The problem with this model is that it requires $< u_1^2 > = < u_2^2 > = < u_3^2 >$ for the shear flows. On the other hand, the angle of the principal axis of the mean strain, S_{ij} (cf. Eq. (4-19)) is 45 degrees, while the angle of the principal axis of $< u_i u_j >$ varies

between 11.5 and 26 degrees in our flow fields. Thus this model cannot represent the Reynolds stress tensor.

A modified version of this model was suggested by Wilcox and Rubesin (1980). Their model has the following form:

$$< u_i u_j > = \frac{1}{3} q^2 \delta_{ij} - 2\nu_T S_{ij} - C \frac{q^6}{\varepsilon^2} (S_{im}\Omega_{mj} + S_{jm}\Omega_{mi}) \quad (6\text{-}10)$$

The last term in this model is designed so that $< u_1^2 >> < u_3^2 > > < u_2^2 >$ in a shear flow such as the one we have treated; it makes no contribution to $< u_1 u_2 >$ in these flows and this model is identical to Eq. (4-21) for this term. For the other components of $< u_i u_j >$, the model has the following form:

$$\begin{aligned} < u_1^2 > &= \frac{1}{3} q^2 + \frac{C}{2} \frac{q^6 S^2}{\varepsilon^2} \\ < u_2^2 > &= \frac{1}{3} q^2 - \frac{C}{2} \frac{q^6 S^2}{\varepsilon^2} \\ < u_3^2 > &= \frac{1}{3} q^2 \end{aligned} \quad (6\text{-}11)$$

Wilcox and Rubesin suggested that the coefficient C, for boundary layers, is 1.23. From our results, however, the coefficient C is found to vary between 0.00022 and 0.0145, depending on the Reynolds and shear numbers; the variation of C does not exhibit any clear-cut pattern. This suggests that this model is not good for homogeneous shear flows.

A more complicated model for the Reynolds stress tensor was derived by Rodi (1976). Rodi's nonlinear algebraic model is based on the assumption that b_{ij} is time-independent and is derived for high Reynolds number flows. It has the following form:

$$< u_i u_j > = q^2 \left[\frac{1}{3} \delta_{ij} + \frac{1}{2} \frac{(1-\gamma)}{C_1} \frac{(\mathcal{P}_{ij}/\varepsilon - \frac{2}{3}\delta_{ij}\mathcal{P}/\varepsilon)}{1 + \frac{1}{C_1}(\mathcal{P}/\varepsilon - 1)} \right] \quad (6\text{-}12)$$

where

$$\mathcal{P}_{ij} = - \langle u_i u_j \rangle \frac{\partial \overline{U}_j}{\partial x_k} - \langle u_j u_k \rangle \frac{\partial \overline{U}_i}{\partial x_k}$$

and

$$\mathcal{P} = \frac{1}{2} \mathcal{P}_{ii}$$

C_1 and γ are model constants. Although the values of γ and C_1 are constant, this model requires $\langle u_2^2 \rangle = \langle u_3^2 \rangle$ in our flow, which is not true.

For the Reynolds shear stress, $\langle u_1 u_2 \rangle$, Eq. (4-21) has the following form:

$$\langle u_1 u_2 \rangle = - \nu_T \frac{\partial \overline{U}_1}{\partial x_2} \tag{6-13}$$

where the eddy viscosity, ν_T, itself needs to be modeled. Models for ν_T are discussed in Chapter IV. Using the results for each of the fourteen simulated flow fields and Eq. (4-23), $\nu_T = CqL$, and Eq. (6-13), we calculate the constant C in Eq. (4-23) and correlate it with the nondimensional parameters. (Note that the length scale used here is the integral length scale, L.) The fitting function used for this purpose has the form:

$$F = C \, Re^{\alpha} \mathcal{A}^{\beta} \tag{6-14}$$

where α, β, and C are determined using least-squares fitting. The results are shown in Fig. 6-40. The straight line in this figure represents a perfect fit, and the symbols are our simulated results. The r.m.s. error shown in the figure indicates the deviation of the data from the fit. It is defined as the average of the squares of difference between our computed data and the fitting function normalized by the average of the data. The solid points are the experimental results of Tavoularis (1978). As shown in the figure, ν_T/qL is nearly Reynolds number independent (the exponent α in Eq. (6-14) is -0.08), and is approximately proportional to the shear number.

$$\frac{\nu_T}{qL} \simeq 0.265\ Re_\lambda^{-0.08}\ \mathcal{A}^{-1.07} \qquad (6\text{-}15)$$

From this relation, one gets

$$\frac{\langle u_1 u_2 \rangle}{q^2} \simeq -0.265\ Re_\lambda^{-0.08}\ \mathcal{A}^{-0.07} \qquad (6\text{-}16)$$

Note that the above relation is good only for $\mathcal{A} > 1$. As can be seen, $\langle u_1 u_2 \rangle / q^2$ is nearly constant in homogeneous shear flows and does not depend heavily on Reynolds and shear numbers.

B. Reynolds Shear Stress Correlation

The values of the Reynolds shear stress correlation, $\frac{\langle u_1 u_2 \rangle}{u_1' u_2'}$, obtained from the simulated flow fields, are given in Table 6-6. As can be seen, $\frac{\langle u_1 u_2 \rangle}{u_1' u_2'}$ varies from -0.54 to -0.74, depending on the Reynolds and shear numbers and time. Assuming that it depends only on Re_λ and $\mathcal{A}$, we use the function (6-14) to correlate $\frac{\langle u_1 u_2 \rangle}{u_1' u_2'}$ with the nondimensional parameters. The results are shown in Fig. 6-41. As shown, the correlation decreases slightly with the Reynolds number and increases with the shear number. This is expected, as discussed in Section 3A-7 of this chapter. The dependence on Reynolds number is very weak. The result is

$$\frac{\langle u_1 u_2 \rangle}{u_1' u_2'} \simeq -0.515\ Re_\lambda^{-0.043}\ \mathcal{A}^{0.134} \qquad (6\text{-}17)$$

The experimental results of Tavoularis (1979), which obtained at St = 8 to 11, are also shown in this figure. They lie slightly below our computed results. This may be because the Reynolds shear stress correlation is time-dependent and/or the fitting function is not exact.

C. Reynolds Stress Anisotropy Tensor

The Reynolds stress anisotropy tensor, b_{ij}, is defined by Eq. (4-33). It is a symmetric and trace-free tensor, which is zero in isotropic flows. To determine the effects of Re_λ and $\mathcal{A}$ on the compo-

nents of b_{ij}, we again use function (6-14) and least-squares to fit the results. The results are shown in Figs. 6-42 through 6-44. As can be seen, b_{ij} is almost independent of Reynolds number. $\mathcal{A}$ has a rather strong effect on b_{11} and b_{22}, but does not have much effect on b_{12}. b_{33} is an order of magnitude smaller than the other components of b_{ij} and is negligible. It can also be seen from the figures that the function does not fit the data well, i.e., there is considerable scatter. It may be because (a) the fitting function is not suitable for b_{ij}, or (b) b_{ij} is time-dependent. The latter seems more reasonable, since the data figures belonging to one flow fall in a line which is not parallel to the fit line.

D. Pressure-Strain Terms

As discussed in Chapter IV, the pressure-strain term ϕ_{ij}, which is responsible for transferring energy from one component of the turbulent kinetic energy to another, can be divided into two distinct parts, the fast term and the Rotta term. The magnitudes of each part of the pressure-strain tensor are given in Appendix C. Since the fast and Rotta terms behave differently, each requires a different model. In this section, we test models which were introduced in Chapter IV for these terms.

D-1. The Fast Term

The part of the pressure strain which is proportional to the mean shear is called the fast term (Eq. (4-46)). A model for this term is given by Eq. (4-49). This model, which was introduced by Hanjalic and Launder (1972) Lumley (1974) and W. C. Reynolds (1976), has only one constant A_1. The constant is computed for each component in each flow. A_1 changes only slightly from one flow field to another; the effects of Reynolds and shear numbers are very small. However, the constant A_1 obtained for $\phi_{11}^{(1)}$ is very different from the constants for the other components of $\phi_{ij}^{(1)}$. The average value of the constant for each component is shown in the first column of Table 6.7. The constant was also fit with the function (6.11), and the results are shown in the last three columns of this table. The Gibson-Launder model is a simplified version of the

above model. It assumes $\phi_{22}^{(1)} = \phi_{33}^{(1)}$, which is found to be incorrect in our flow; therefore this model is poor compared to the more general model, Eq. (4-49).

D-1. The Rotta Term

The part of the pressure strain which is not explicitly dependent on the mean flow, $\phi_{ij}^{(2)}$, is the Rotta term (Eq. (4-53)). As shown in Table C-5, the magnitude of $\phi_{33}^{(2)}$ is very small compared to the magnitude of the other components. For this reason, this component is not considered in this section.

Two models for $\phi_{ij}^{(2)}$ are given in Chapter IV. The Rotta model, Eq. (4-55), assumes that the pressure-strain tensor is proportional to the Reynolds stress anisotropy. The constant A_2 for this model is calculated using our simulated results and is given in Table 6-8. The constant A_2 obtained from each component of $\phi_{ij}^{(2)}$, is fitted by a function of the form (6.11). The results are given in the table. As can be seen, A_2 varies very much from one flow to another and is not well fit as a function of the nondimensional ~~prameters~~ parameters. This suggests that this model is not likely to be useful.

Table 6-9 shows the constant A_3 and its invariants obtained using the modified Rotta model, Eq. (4-56). As shown, A_3 has less variation and is nearly constant for all of the components. The variation of A_3 with Re_λ and $\mathcal{A}$ is obtained using least-square fitting, and the results are given in Table 6-9. The constant A_3 increases with the Reynolds number and decreases with the shear number. If a constant value for A_3 is to be used, our results suggest $A_3 = 2.7$.

E. Dissipation Anisotropy Tensor

The dissipation anisotropy tensor, d_{ij}, is defined by Eq. (4-57). Its magnitude can be calculated from the dissipation tensor, given by Table C-3. d_{ij} is a symmetric, trace-free tensor. The dissipation is frequently assumed isotropic at high Reynolds numbers, and we expect $|d_{ij}|$ to decrease with Reynolds number. On the other hand, $|d_{ij}|$ is zero in isotropic flows when $\mathcal{A} = 0$, and one expects it to increase with the shear number. We use a least-squares fit to our simulated

data, using function (6-11) to study the behavior of d_{ij} as a function of $\mathcal{A}$ and Re_λ. Figures 6-45 through 6-47 show the results. Note that d_{33} is very small, so its behavior is not shown here. As can be seen from the figures, all of the components decrease with Re_λ and increase with $\mathcal{A}$. This is expected, as discussed above. However, the effect of Reynolds number is smaller than expected, suggesting that the dissipation may remain anisotropic even at quite high Reynolds numbers. This is contrary to the assumption made by many people that the dissipation is isotropic at high Reynolds numbers.

6-5. Behavior of the Scalar Fields and Their Models

In this section, the effects of Reynolds, shear, and Prandtl numbers on various turbulence statistics obtained from 56 generated scalar fields will be studied. Models introduced in Chapter IV for these terms will be tested, and their validity over the range of Re_λ, $\mathcal{A}$, and Pr will be examined. The constant(s) for each model will be calculated, and their behavior as functions of the non-dimensional parameters will be discussed. We use least-squares fits to correlate the results.

A. The Non-Dimensional Scalar Fluctuations

The non-dimensional scalar fluctuation, $\mathcal{A}_{\theta 2} = \theta'/S_2 L$, is a dependent parameter, as discussed in Section 6-1. Therefore, we suspect $\mathcal{A}_{\theta 2}$ to be a function of Reynolds, shear, and Prandtl numbers. We use the following power-law function to determine its dependence on Re_λ, $\mathcal{A}$, and Pr:

$$F = C\, Re_\lambda^{\alpha}\, \mathcal{A}^{\beta}\, Pr^{\gamma} \qquad (6\text{-}18)$$

where C, α, β, and γ are determined by least-squares fitting. The results, along with the experimental results, are shown in Fig. 6-48.

As can be seen, the experimental results behave very similar to the simulated results. It can also be seen that $\mathcal{A}_{\theta 2}$ is almost independent of Re_λ. The result is

$$\mathcal{A}_{\theta 2} \simeq Re_\lambda^{-0.021}\, \mathcal{A}^{-0.955}\, Pr^{0.172} \qquad (6\text{-}19)$$

Substituting the definitions of $\mathcal{A}_{\theta 2}$ and $\mathcal{A}$ in the above equation, the above relation can be approximated as:

$$\frac{\theta'}{\partial \overline{C}/\partial x_2} \simeq \frac{q}{\partial \overline{U}_1/\partial x_2} \, Pr^{0.172} \tag{6-20}$$

so the ratio of the r.m.s. scalar fluctuation to the mean scalar gradient is proportional to the ratio of the turbulence velocity to the mean velocity gradient.

B. Turbulence Heat Flux

The magnitudes of the turbulence heat fluxes, $< \theta u_1 >$ and $< \theta u_2 >$, obtained from the simulated scalar fields, are given in Appendix C. Note that $< \theta u_3 > = 0$. As can be seen from Table C-7, the heat flux ratio, $< \theta u_1 > / < \theta u_2 >$ varies from 1 to 4, depending mainly on the shear number. This is expected because, as $\mathcal{A}$ increases, the flow becomes more anisotropic and u_1'/u_2' increases. Therefore, $< \theta u_1 > / < \theta u_2 >$ increases with $\mathcal{A}$.

C. One-Point Velocity-Scalar Correlations

The velocity-scalar correlation is defined as $< \theta u_i > / \theta' u_i'$ (no summation). There are two non-zero components, $< \theta u_1 > / \theta' u_1'$ and $< \theta u_2 > / \theta' u_2'$. They are given in Table 6-10. The magnitudes of these terms change only slightly from one flow to another. To correlate these terms with the independent parameters of the flow, we use function (6-18). The results are shown in Figs. 6-49 and 6-50. They have the following form:

$$\frac{< \theta u_1 >}{\theta' u_1'} = 0.417 \, Re_\lambda^{0.021} \, \mathcal{A}^{0.138} \, Pr^{0.012} \tag{6-21}$$

and

$$\frac{< \theta u_2 >}{\theta' u_2'} \simeq -0.561 \, Re_\lambda^{0.066} \, \mathcal{A}^{0.139} \, Pr^{-0.061} \tag{6-22}$$

Comparing these with Eq. (6-17), we see the one-point velocity-velocity and velocity-scalar correlations are very similar. They all increase

with the shear number at the same rate and have very weak dependence on Reynolds number.

D. Turbulent Eddy Diffusivity Tensor

The turbulent eddy diffusivity tensor, D_{ij}, is defined by Eq. (4-26). It is non-symmetric. Only two components D_{12} and D_{22} can be calculated from our 56 simulated scalar fields. The other components can be computed when $\partial\bar{C}/\partial x_1$ and $\partial\bar{C}/\partial x_3$ are not zero and will be discussed later. Let us consider the behavior of D_{12} and D_{22}. Then we study the behavior of the other components using the results obtained from two particular runs with non-zero $\partial\bar{C}/\partial x_1$ and $\partial\bar{C}/\partial x_3$. Figures 6-51 and 6-52 show D_{12}/qL and D_{22}/qL as power law functions of the non-dimensional parameters. The results obtained by using least-squares fitting have the following forms:

$$\frac{D_{12}}{qL} \simeq 0.259\ \mathrm{Re}^{-0.014}\ \mathcal{A}^{-0.72}\ \mathrm{Pr}^{0.19} \qquad (6\text{-}23)$$

$$\frac{D_{22}}{qL} \simeq -0.487\ \mathrm{Re}_\lambda^{-0.132}\ \mathcal{A}^{-1.1}\ \mathrm{Pr}^{0.11} \qquad (6\text{-}24)$$

Using the definition of D_{ij} and $\mathcal{A}$, and Eq. (6-16), the above relations are approximately

$$\frac{\langle \theta u_1 \rangle}{q\theta'} \simeq 0.478 \qquad (6\text{-}25)$$

$$\frac{\langle \theta u_2 \rangle}{q\theta'} \simeq 0.248 \qquad (6\text{-}26)$$

These are very similar to the relation for the one-point velocity-velocity correlations, Eq. (6-16). This suggests that the eddy viscosity and diffusivity behave similarly. This is also seen from the experimental results (Tavoularis (1979)).

In Chapter IV, we derived a model for the eddy diffusivity tensor. The models for D_{12} and D_{22}, Eq. (4-35), have the following forms.

$$\frac{D_{12}}{q^2/S} = \left[C_1 \frac{\langle u_1 u_2 \rangle}{q^2} + \frac{C_2}{2} \right] \mathrm{Re}_\lambda^{\alpha}\ \mathcal{A}^{\beta}\ \mathrm{Pr}^{\gamma} \qquad (6\text{-}27)$$

and

$$\frac{D_{22}}{q^2/S} = \left[C_1\left(\frac{<u_2^2>}{q^2} - \frac{1}{3}\right) + C_3\right] Re_\lambda^{\alpha'} \mathcal{A}^{\beta'} Pr^{\gamma'} \qquad (6\text{-}28)$$

The magnitudes of the constants in the above relations were obtained using least-squares of our computed results. The results are shown in Figs. 6-53 and 6-54. As shown, the magnitudes of the constants are $C_1 = 1.20$, $C_2 = 0.99$, and $C_3 = 0.569$; the constant C_1 is fixed for both D_{12} and D_{22}. The constants are nearly independent of Reynolds number and are proportional to $Pr^{0.17}$. This model fits the data quite well.

So far, we have discussed only the two components of D_{ij} that participate when $\partial\overline{C}/\partial x_2$ is the only non-zero mean scalar gradient. To obtain the other components of D_{ij}, we ran two further cases. Each run used the same hydrodynamic field and initial conditions, but one had non-zero $\partial\overline{C}/\partial x_1$ and the other was for non-zero $\partial\overline{C}/\partial x_3$. Table 6-11 shows the components of D_{ij} obtained from these simulations. As can be seen, D_{11} has the largest value. This is expected because D_{11} is proportional to u_1, which is the largest velocity component. D_{22} and D_{21} have the smallest values, for similar reasons. Only a few components of D_{ij} are experimentally determined. Table 6-12 shows the values of D_{ij}/D_{22} obtained from the experimental results of Corrsin (1980) and the present results. The experimental results are obtained at $Re_\lambda = 396$ and $\mathcal{A} = 12.76$.

Note that the diffusion equation (2-20) is linear, so the θ obtained from different runs can be added or subtracted. Results for a case in which the mean scalar gradient is non-zero in all three directions can be obtained from three runs, each of which has a mean gradient in one direction. However, the θ fields are not uncorrelated, because the same velocity field is the same. Then, $<\theta_1\theta_2>$ is not necessarily zero when θ_1 and θ_2 are results from two different runs.

E. Turbulent Prandtl Number

The turbulent Prandtl number, Pr_T, is the ratio of eddy viscosity to eddy diffusivity (Eq. (4-36)). The magnitude of turbulent Prandtl

number for each flow field is given in Table 6-13. Its behavior as a function of Reynolds, shear, and Prandtl numbers is shown in Fig. 6-55. As can be seen, Pr_T is almost independent of Re_λ and $\mathcal{A}$. It decreases when molecular Prandtl number increases, and vice versa. The result of least-squares fitting of the data is:

$$Pr_T \simeq 0.528\ Re_\lambda^{0.05}\ \mathcal{A}^{0.036}\ Pr^{-0.105} \qquad (6\text{-}29)$$

The values of Pr_T obtained from 56 simulated flow fields were used to test models described in Chapter IV. The results are shown in Figs. 6-56 through 6-59.

The first three of these figures test Reynolds', Wassel's, and Crawford's models, given by Eqs. (4-37) through (4-39), respectively. All of the models behave similarly and fit the simulated results rather poorly. The suggested values for the model constants suggested in the literature are different from the constants obtained from our simulated results.

Figure 6-59 tests the model derived in Chapter IV, Eq. (4-40). This model fits the data much better than the models mentioned above. The model can be approximately simplified to:

$$Pr_T = \frac{0.38}{\mathcal{A}^{0.2}\ Pr^{0.12}\left(1.20\ \frac{<u_2^2>}{q^2} + 0.169\right)} \qquad (6\text{-}30)$$

F. Pressure-Scalar Covariance

Like the pressure-strain, the pressure-scalar covariance contains two parts. The magnitudes of each part of the pressure-scalar covariance computed from our simulated flow fields are given in Appendix C. In this section we examine the pressure-scalar covariance models introduced in Chapter IV.

F-1. The Fast Term

The part of the pressure-scalar covariance which is proportional to the mean velocity gradient $\phi_i^{(1)}$ is called the fast or rapid term (Eq. (4-60)).

Let us consider the model given by Eqs. (4-69) and (4-70). The constant A_o in this model is 2/5, according to the assumptions made in Chapter IV. In this section we use our simulated results and calculate A_o. The behavior of A_o as a function of the nondimensional parameters is obtained using the least-squares fitting and function (6-21). The results are shown in ~~Figs. 6-70 to 6-71 and also~~ in Table 6-14. As shown, the value of A_o changes very slightly throughout the 56 flow fields (i.e., the variance of A_o is small) and has small dependency on Re_λ, $\mathcal{A}$, and Pr. This suggests that much of the important physics is captured by the model. On the other hand, the computed value of A_o is less than one-half of the expected value. This suggests that the assumptions (mentioned in Chapter IV) made in deriving the model are not sufficient, and a more complicated model may be needed to get better results.

Let us now consider Lumley's model, Eqs. (4-72) and (4-73). This model satisfies all of the conditions of the previous one plus a new condition mentioned in Chapter IV. The constant A_o in this model is predicted to be 1/2. The values of A_o and its behavior as a function of Re_λ, $\mathcal{A}$, and Pr for the two components of $\phi_i^{(1)}$. are given in Table 6-15. As shown, the variation of A_o over 56 flow fields is small, and therefore the model captures much of the important physics. However, the magnitude of the constant is different from 1/2 and varies from one component to another.

F-2. The Rotta Term

The second part of the pressure-scalar covariance, $\phi_i^{(2)}$, is defined by Eq. (4-74). This part does not explicitly depend on the mean flow. Equations (4-79) and (4-80) represent a model for this term. The model is analogous to the modified Rotta model used for the pressure-strain covariance. The constant A_1 obtained by using our simulated results is given in Table 6-16. The behavior of A_1 as a function of

Re_λ and $\mathscr{A}$ are also given in the table. As we see, the constants for both components of $\phi_i^{(2)}$ are nearly the same and have very small variation due to the Re_λ, $\mathscr{A}$, and Pr. This is similar behavior to that of the modified Rotta model for the pressure-strain terms.

6.5 Comparison with the Other Flows

Nearly all turbulent flows in nature are inhomogeneous, i.e., the shear varies through the flow. The homogeneous flows may be structurally different from their inhomogeneous counterparts; the two kinds of flows might require different types of models, and thus our results and discussion for mixing of a passive scalar in homogeneous flows might not be valid for inhomogeneous flows. We shall briefly compare some of our results with those for inhomogeneous flows.

Table 6-17 compares non-dimensional quantities obtained in the logarithmic region of a boundary layer and in one of our runs. These values are nearly constant in the logarithmic region but differ in the outer region.

The shear number was found to play an important role in homogeneous flows. Its value as a function of y^+ in the boundary layer is given in Table 6-18. It is nearly constant in the logarithmic region but changes rapidly in the other regions. In this region, the agreement with our results is quite good. In the inner region, the shear number changes rapidly and the wall has a very strong effect on the behavior of the turbulence. Both of these effects make the flow very different from a homogeneous flow, and our results cannot be applied. Clearly, specific models which account for these effects are needed and are, of course, in common use. In the outer (wake) region of the boundary layer, the shear number rapidly becomes small and there are again inhomogeneity effects which make comparison with our results very difficult. The interaction with the irrotational outer flow also has a strong effect.

Table 6-19 shows the variation of some of the turbulence statistics through a turbulent free shear layer and compares them with our homogeneous shear flow results. The turbulence statistics are nearly constant for $-0.5 < \eta < 0.5$. In this region the shear rate, $\partial \overline{U}_1/\partial x_2$, is

nearly constant and the results, as expected, are comparable to our homogeneous shear flow results. The shear number is also nearly constant in this region and is of the same order of magnitude as in boundary layers. In the region where $|\eta| > 0.5$, the interaction with the irrotational flow causes strong inhomogeneity effects and the comparison with our flow is difficult.

Table 6-1

VELOCITY FIELD

Parameter	Notation	Dimension
Turbulence Velocity	$q = \langle u_i u_i \rangle^{1/2}$	$L\ T^{-1}$
Kinematic Viscosity	ν	L^2T^{-1}
Integral Length Scale	L	L
Taylor Microscale	λ	L
Time	t	T

Table 6-2

SCALAR FIELD

Parameter	Notation	Dimension
Turbulent Scalar Intensity	$\theta' = \langle \theta^2 \rangle^{1/2}$	Θ
Diffusion Coefficient	D	L^2T^{-1}
Mean Scalar Gradient	$S_2 = \frac{\overline{\partial C}}{\partial x_2}$	$\Theta\ L^{-1}$
Integral Length Scale	L_θ	L
Taylor Microscale	λ_θ	L

TABLE 6-3

Range of Non-Dimensional Parameters

Parameters	Present Data	Experimental Data
Re	10 - 120	130 - 400
α	5 - 70	3 - 14.8
Pr	0.2 - 5	0.7
St	0 - 7	0 - 12

TABLE 6-4

Non-Dimensional Parameters For Each Flow Field

Simulations	Parameters	St=4	St=5	St=6	St=7
HS64A	Re	44.560	52.057	59.215	66.762
	α	18.549	18.983	19.485	19.993
	Pr	1.000	1.000	1.000	1.000
HS64B	Re	18.996	21.840	24.545	27.175
	α	23.727	25.178	26.790	29.397
	Pr	1.000	1.000	1.000	1.000
HS64G	Re	60.348	75.711	92.476	10.080
	α	66.879	69.205	68.924	68.878
	Pr	1.000	1.000	1.000	1.000
HS64J	Re	24.202	27.626	31.233	35.222
	α	11.228	12.617	14.493	16.328
	Pr	1.000	1.000	1.000	1.000
HS64M	Re	29.156	34.132	39.054	44.550
	α	8.936	10.333	11.987	13.853
	Pr	1.000	1.000	1.000	1.000
HS64O	Re	64.310	71.840	78.990	86.910
	α	6.376	7.120	7.738	8.236
	Pr	1.000	1.000	1.000	1.000
HS64C	Re	18.996	21.840	24.545	27.175
	α	23.727	25.178	26.790	29.397
	Pr	5.000	5.000	5.000	5.000

TABLE 6-4 Continued

Simulations	PArameters	St=4	St=5	St=6	St=7
HS64D	Re	44.560	52.057	59.215	66.762
	α	18.549	18.983	19.485	19.993
	Pr	5.000	5.000	5.000	5.000
HS64E	Re	44.560	52.057	59.215	66.762
	α	18.549	18.983	19.485	19.993
	Pr	0.200	0.200	0.200	0.200
HS64F	Re	18.996	21.840	24.545	27.175
	α	23.727	25.178	26.790	29.397
	Pr	0.200	0.200	0.200	0.200
HS64H	Re	60.348	75.711	92.476	10.080
	α	66.879	69.205	68.924	68.878
	Pr	5.000	5.000	5.000	5.000
HS64I	Re	60.348	75.711	92.476	10.080
	α	66.879	69.205	68.924	68.878
	Pr	0.200	0.200	0.200	0.200
HS64N	Re	29.156	34.132	39.054	44.550
	α	8.936	10.333	11.987	13.853
	Pr	0.200	0.200	0.200	0.200
HS64P	Re	64.310	71.840	78.990	86.910
	α	6.376	7.120	7.738	8.236
	Pr	0.200	0.200	0.200	0.200

TABLE 6-5

Principal Axis Angle (Radians)

Equation 4-17

Simulation	ST=4	ST=5	ST=6	ST=7
HS64A	0.31886	0.27182	0.23674	0.22285
HS64B	0.32776	0.27180	0.22677	0.20689
HS64G	0.26261	0.21147	0.17420	0.15333
HS64J	0.40883	0.34481	0.29152	0.26612
HS64M	0.43080	0.37272	0.32677	0.30371
HS64O	0.45910	0.42296	0.40323	0.39940

TABLE 6-6

One-Point Correlations of the Velocity Field

$$\langle u_1 u_2 \rangle / u_1' u_2'$$

Simulation	St=4	St=5	St=6	St=7
HS64A	0.68350	0.67890	0.68780	0.67250
HS64B	0.67680	0.67560	0.70390	0.69340
HS64G	0.72830	0.73470	0.76240	0.74390
HS64J	0.62960	0.63344	0.63720	0.61760
HS64M	0.61800	0.61666	0.60490	0.59520
HS64O	0.54260	0.54720	0.54800	0.54280

TABLE 6-7

Constant For the Pressure-Strain Model, Eq. 4-49

The Fast Term

Fitting Function $A_1 = C\,Re^{\alpha}\,\ell^{\beta}$

Equation	A_1	C	α	β	r.m.s. error
i=1, j=1	-6.94 ±0.519	9.75	-0.028	-0.082	0.038
i=2, j=2	-1.83 ±0.400	1.55	0.038	0.008	0.060
i=3, j=3	-1.57 ±0.380	6.82	-0.185	-0.282	0.093
i=1, j=2	-1.52 ±0.077	2.01	-0.082	0.010	0.032

TABLE 6-8

Constant For the Pressure-strain model, Eq. (4-53)

Rotta Model

Fitting Function $A_3 = C\,Re^{\alpha}\,\ell^{\beta}$

Equation	A	C	α	β	r.m.s. error
i=1, j=1	0.673 ±0.599	1.143	0.678	-1.195	0.15
i=2, j=2	0.673 ±0.570	0.734	0.715	-1.075	0.13
i=1, j=2	0.679 ±0.452	0.238	0.813	-0.776	0.15

TABLE 6-9

Constant For the Pressure-Strain Model, Eq. (4-56)

Modified Rotta Model

Fitting Function $A_3 = C\,Re^{\alpha}\,\ell^{\beta}$

Equation	A_3	C	α	β	r.m.s. error
i=1, j=1	2.862 ±0.349	3.342	0.144	-0.225	0.045
i=2, j=2	3.080 ±0.428	4.200	0.119	-0.245	0.048
i=1, j=2	2.472 ±0.426	1.633	0.330	-0.266	0.085

TABLE 6-10

One-Point Velocity-Scalar Correlation

$$\langle u_i \theta \rangle / u_i' \theta'$$

Simulation	I	St=4	St=5	St=6	St=7
HS64A	1	0.6674	0.6513	0.6351	0.5822
	2	0.7064	0.6742	0.6370	0.5891
HS64B	1	0.6504	0.6130	0.5726	0.5197
	2	0.7476	0.7302	0.7072	0.6410
HS64G	1	0.7949	0.7541	0.7041	0.6583
	2	0.7803	0.7746	0.7765	0.7320
HS64J	1	0.8552	0.8236	0.7709	0.7102
	2	0.6890	0.6542	0.5878	0.5197
HS64M	1	0.7721	0.7662	0.7687	0.7244
	2	0.6570	0.6134	0.5570	0.5222
HS64O	1	0.8131	0.8058	0.8031	0.7564
	2	0.5682	0.5506	0.5195	0.4999
HS64C	1	0.7877	0.7464	0.6871	0.6524
	2	0.6674	0.6513	0.6351	0.5822
HS64D	1	0.7090	0.6724	0.6291	0.6078
	2	0.6504	0.6130	0.5726	0.5197
HS64E	1	0.6561	0.6806	0.7051	0.7414
	2	0.7949	0.7541	0.7041	0.6583
HS64F	1	0.6054	0.6129	0.6282	0.6706
	2	0.8552	0.8236	0.7709	0.7102
HS64H	1	0.7315	0.7887	0.8301	0.8614
	2	0.7721	0.7662	0.7687	0.7244
HS64I	1	0.7306	0.7770	0.8099	0.8366
	2	0.8131	0.8058	0.8031	0.7564
HS64N	1	0.5949	0.6310	0.6506	0.6805
	2	0.7877	0.7464	0.6871	0.6524
HS64P	1	0.5495	0.5793	0.5991	0.6198
	2	0.7090	0.6724	0.6291	0.6078

TABLE 6-11

Components of Nomalized Eddy Diffusivity Tensor

D_{ij} / qL

Equation	St=3	St=4	St=5	St=6
i=1, J=1	-0.08770	-0.09750	-0.10690	-0.09810
i=2, J=2	-0.03200	-0.02530	-0.01792	-0.01200
i=3, J=3	-0.03430	-0.03325	-0.03335	-0.02590
i=1, J=2	0.04645	0.04786	0.04696	0.03910
i=2, J=1	0.03253	0.03026	0.02462	0.01910

TABLE 6-12

Experimental and Computed Values of Normalized Turbulent Eddy Diffusivity

D_{ij}/D_{22}

Equations	Computed Values at St=3	Experimental Results (Corrsin (1980))
i=1, j=1	-6.00	*
i=2, j=1	1.40	*
i=1, j=2	2.30	2.20
i=2, j=2	1.00	1.00
i=3, j=3	-1.60	-1.60

* The experimental values are not available.

TABLE 6-13

Turbulent Prandtl Number

Equation (4-36)

Simulations	St=4	St=5	St=6	St=7
HS64A	0.6617	0.7089	0.7850	0.8585
HS64B	0.5984	0.6173	0.6766	0.7550
HS64G	0.6589	0.6950	0.7445	0.7945
HS64J	0.5800	0.6125	0.7006	0.8010
HS64M	0.6093	0.6602	0.7321	0.7950
HS64O	0.6143	0.6386	0.6917	0.7269
HS64C	0.5302	0.5452	0.5900	0.6522
HS64D	0.6129	0.6538	0.7192	0.7870
HS64E	0.8609	0.9190	1.0280	1.1200
HS64F	0.8769	0.8910	0.9996	1.1310
HS64H	0.6461	0.6790	0.7241	0.7695
HS64I	0.7217	0.7716	0.8417	0.9125
HS64N	0.8584	0.8722	0.9208	0.9710
HS64P	0.7482	0.7712	0.8166	0.8335

TBALE 6-14

Constant for Pressure-Scalar Covariance Model, Eqs. (4-69) and (4-70)

The Fast Term

Fittins Function $A_0 = C\ Re^{\alpha}\ \mathcal{A}^{\beta}\ Pr^{\gamma}$

Equation	A_0	C	α	β	γ	r.m.s. error
(4-69)	0.229 ±0.079	0.543	0.025	-0.341	-0.096	0.17
(4-70)	0.144 ±0.066	0.312	-0.018	-0.287	-0.148	0.11

TABLE 6-15

Constant for Pressure-Scalar Covariance Model, Eq.(4-71)

Lumley's Model for the Fast Term

Fittins function $A_0 = C\ Re^{\alpha}\ \mathcal{A}^{\beta}\ Pr^{\gamma}$

i	A_0	C	α	β	γ	r.m.s. error
1	0.676 ±0.081	0.754	0.014	-0.059	-0.043	0.17
2	0.276 ±0.103	0.085	-0.035	0.401	-0.018	0.18

TABLE 6-16

Constatnt for the Pressure-Scalar Model

The Rotta-Like Term

Fittins Function $A_1 = C\ Re^{\alpha}\ \mathcal{A}^{\beta}\ Pr^{\gamma}$

Equation	A_1	C	α	β	γ	r.m.s. error
(4-79)	-1.580 ±0.677	1.031	0.170	-0.128	-0.307	0.16
(4-80)	-1.789 ±0.730	0.744	0.461	-0.333	-0.157	0.14

Table 6-17

Comparison of Turbulence Statistics in Homogeneous Shear Flows and Boundary Layers

Quantity	Homogeneous Shear Flow Run HS64J at St = 7	Boundary Layer*
$\frac{\langle u_1 u_2 \rangle}{q^2}$	-0.147	-0.130
$\frac{\langle u_1 \theta \rangle}{q\theta'}$	0.547	0.50
$\frac{\langle u_2 \theta \rangle}{q\theta'}$	-0.160	-0.20
Pr_T	0.80	1.05
$\frac{D_{12}}{D_{22}}$	-2.30	-2.40

*Johnson (1959)

Table 6-18

Variation of Non-Dimensional Quantities in Channel Flow[†]

$$Re_\delta = \frac{u_c \delta^{**}}{\nu} = 13800$$

y^+	Re_L^*	$\mathscr{L}$	
3.85	747.8	1117.90	Sublayer
16.09	2200	111.63	
38.18	2190	27.47	
77.18	1496	9.50	
143.4	1540	3.95	Log-region
248.9	961	2.13	
440.7	770	1.79	
590.1	528	0.348	Centerline

[†]Moin (1981).

*Re_L is Reynolds number based on the integral length scale.

**δ is channel half-width.
u_c is mean velocity at the centerline.

Table 6-19

Comparison of Turbulence Statistics in Homogeneous Shear Flow and Free Shear Layers*

Quantity	Free Shear Layer**							Homogeneous Shear Flow, Run HS64J at St = 7
	$\eta = -1.0$	$\eta = -0.75$	$\eta = 0.5$	$\eta = 0.8$	$\eta = 0.5$	$\eta = 0.75$	$\eta = 1.0$	
$-\frac{\langle u_1 u_2 \rangle}{u_1' u_2'}$	0.312	0.38	3.45	0.50	0.40	0.28	0.16	0.62
$\frac{\langle \theta u_2 \rangle}{\theta' u_2'}$	0.55	0.59	0.60	0.65	0.42	0.332	0.23	0.520
Pr_T	0.60	0.62	0.65	0.82	0.79	0.70	0.56	0.80
	0.987	1.16	1.25	1.58	2.00	1.82	1.82	16.00
Re_L	6231	8107	9340	9262	8936	7678	6234	140

*Batt (1977).

**The values obtained at $x_1 - x_{10} = 18.5"$ for $\overline{U}_1 = 23$ ft/sec and $\overline{U}_2 = 0.0$.

$$\eta \equiv \frac{12\left(x_2 - (x_2)_{0.5}\right)}{x_1 - x_{10}}, \quad Re_L \equiv \frac{\overline{U}_1 L}{\nu}, \quad \text{where } L \text{ is integral length scale}$$

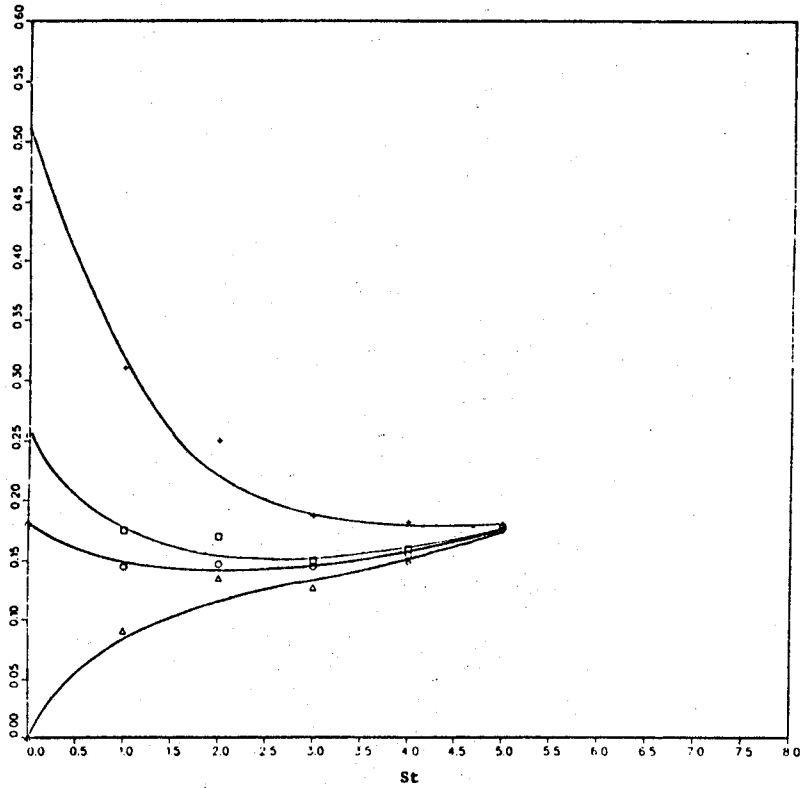

Fig. 6-1. Nondimensional scalar quantity, $\mathcal{L}_{\theta 2}$, as a function of time for various runs with different initial values.

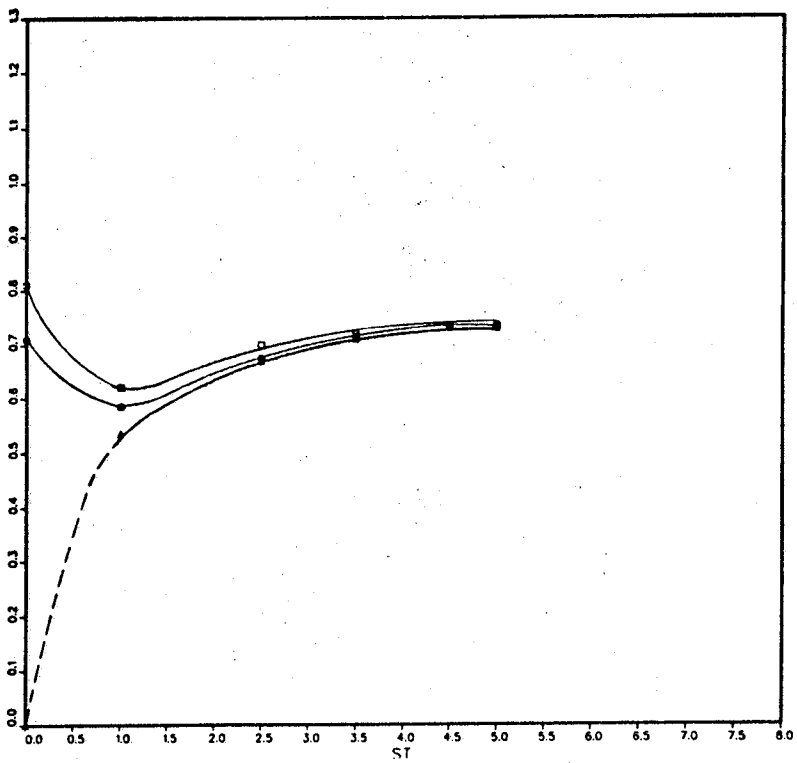

Fig. 6-2. Integral length scale ratio of the velocity and scalar field as a function of time for various runs with different initial values.

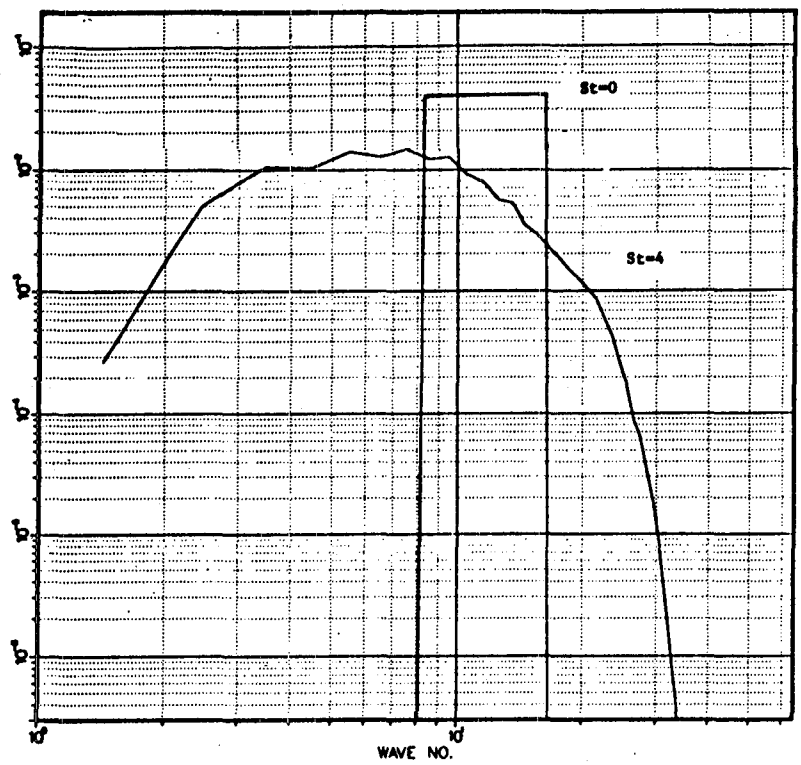

Fig. 6-3. Three-dimensional energy spectra.

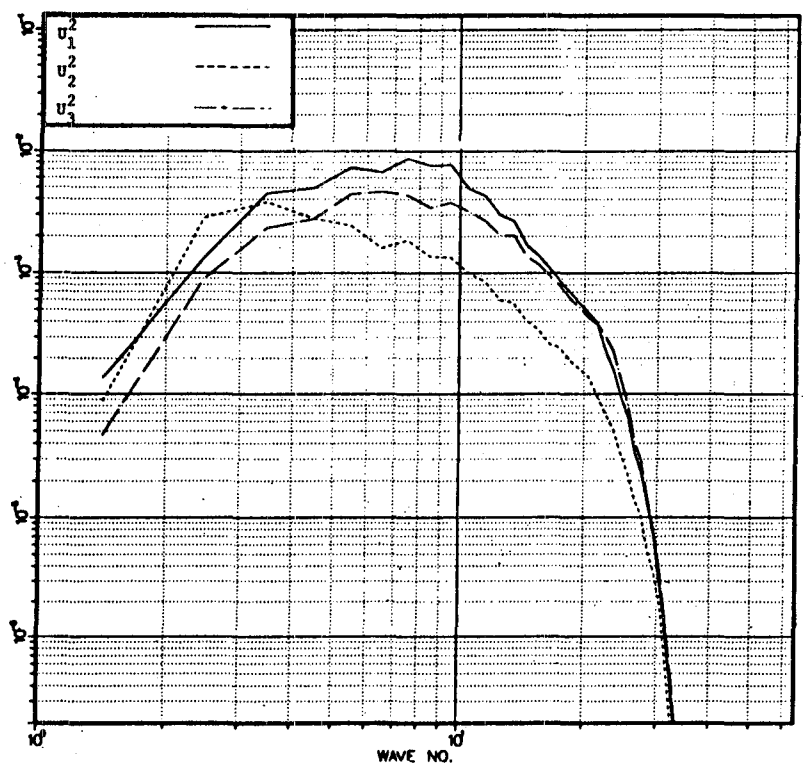

Fig. 6-4. Three-dimensional spectra of the turbulent kinetic energy components.

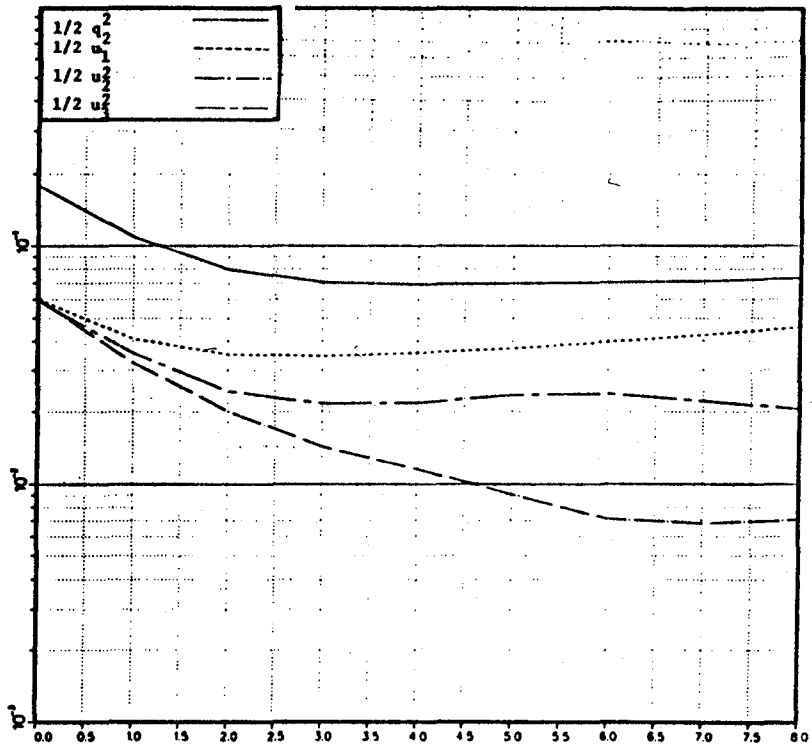

Fig. 6-5. Turbulent kinetic energy and its components as a function of time.

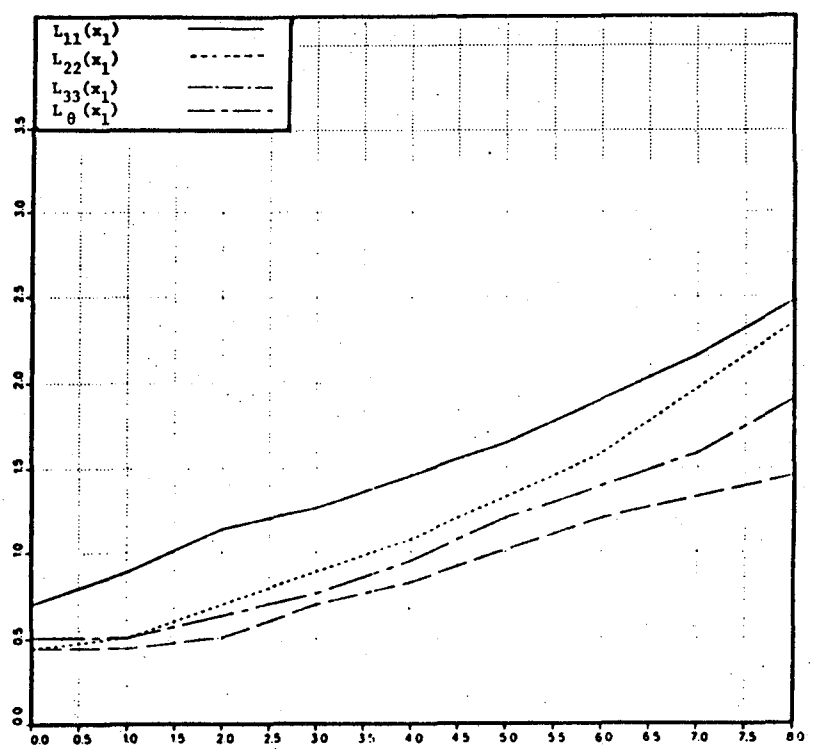

Fig. 6-6. Integral length scales in the x_1-direction as a function of time.

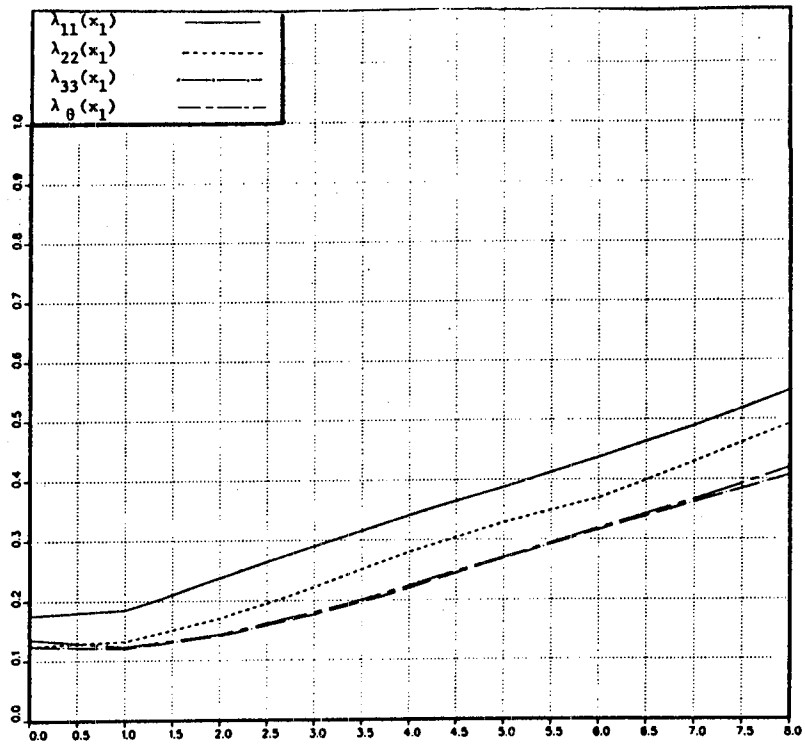

Fig. 6-7. Taylor microscales in the x_1-direction as a function of time.

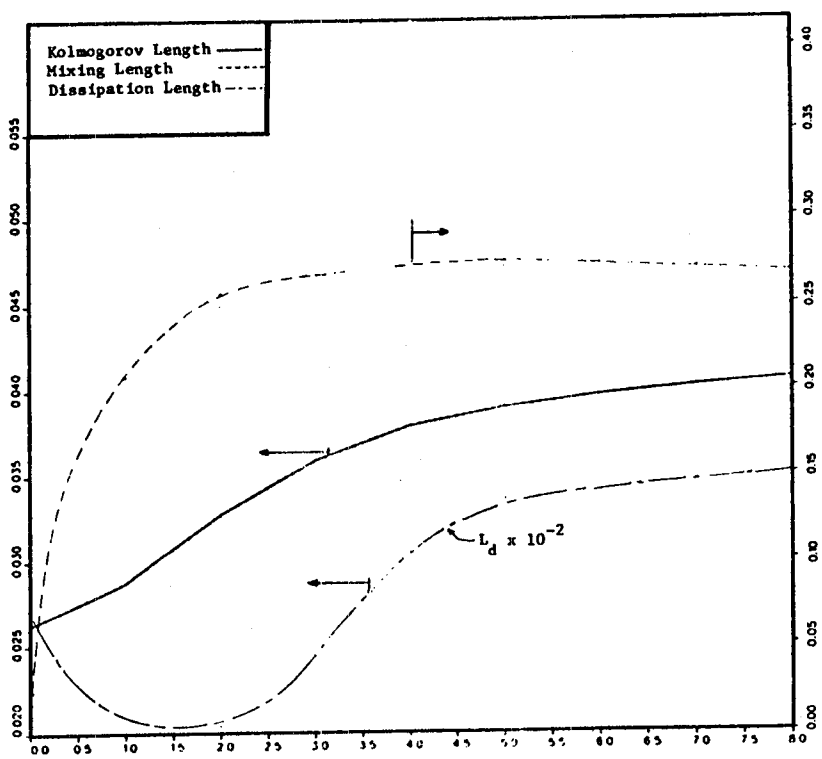

Fig. 6-8. Various lenyth scales as a function of time.

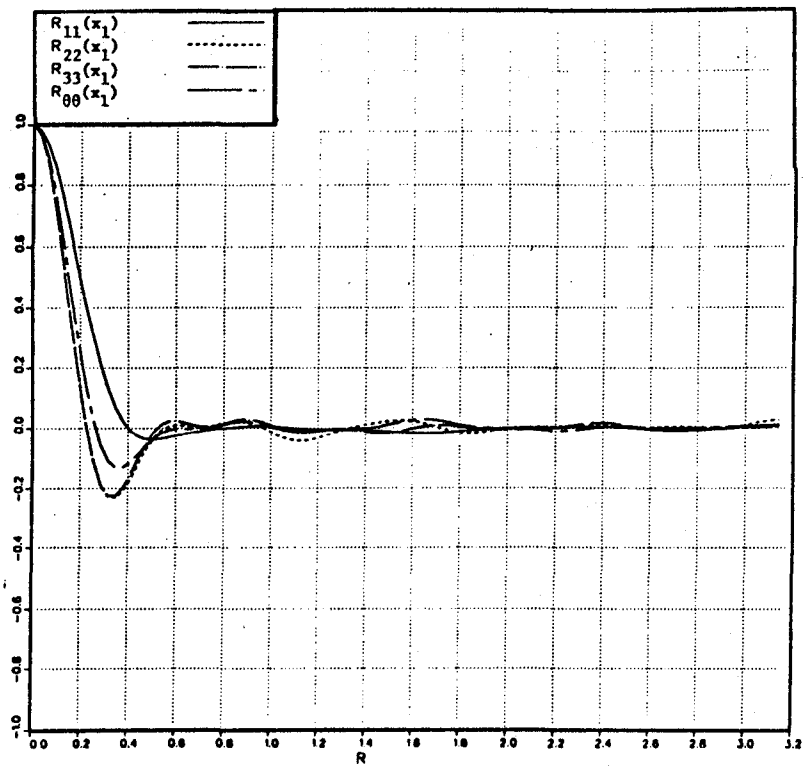

Fig. 6-9. Two-point correlations of velocity components, R_{ij}, and scalar, $R_{\theta\theta}$, at St = 0.

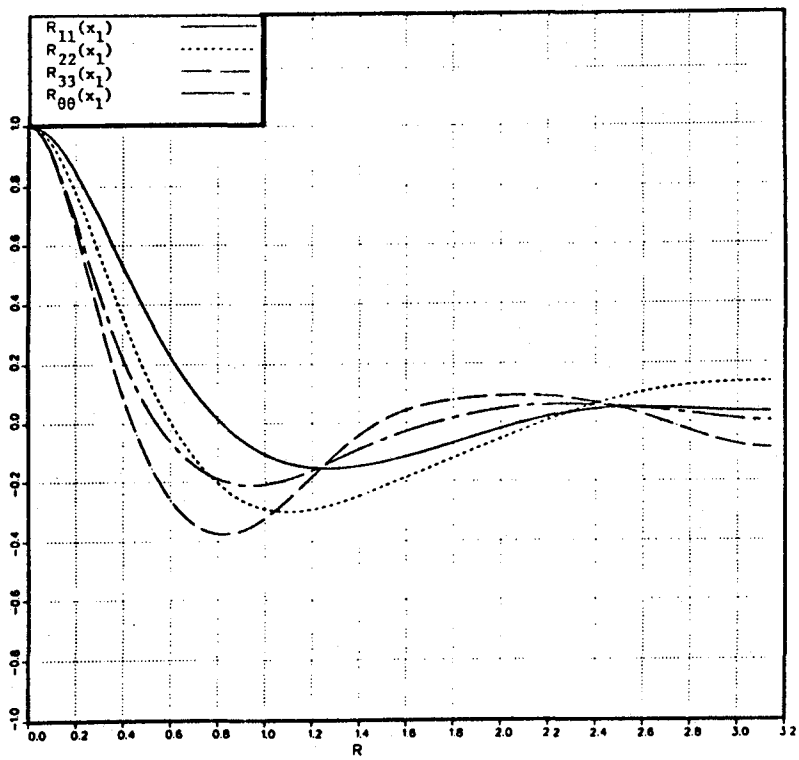

Fig. 6-10. Two-point correlations of velocity components, R_{ij}, and scalar, $R_{\theta\theta}$, at St = 4.

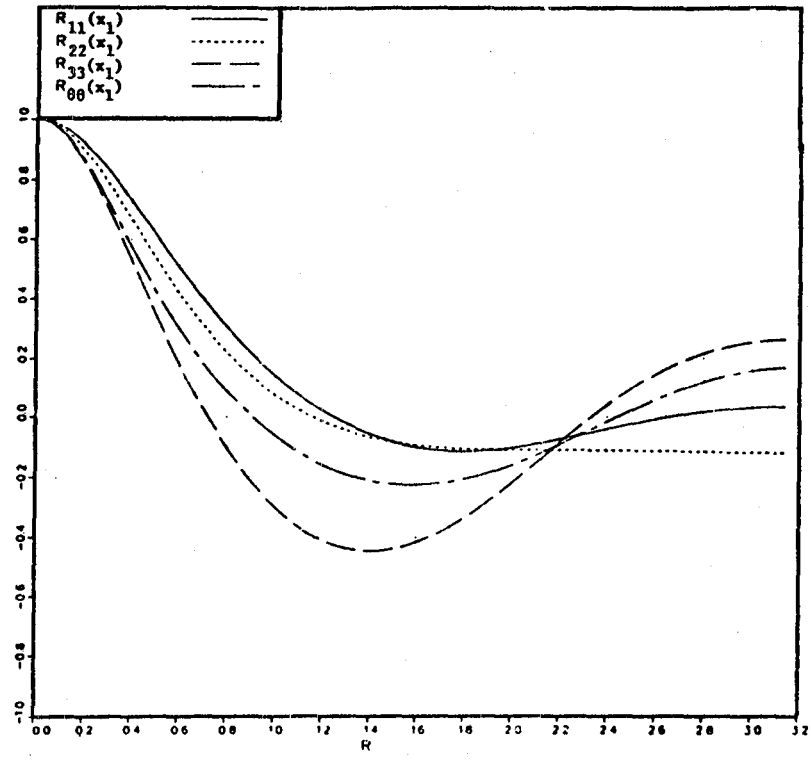

Fig. 6-11. Two-point correlations of velocity components, R_{ij}, and scalar, $R_{\theta\theta}$, at St = 7.

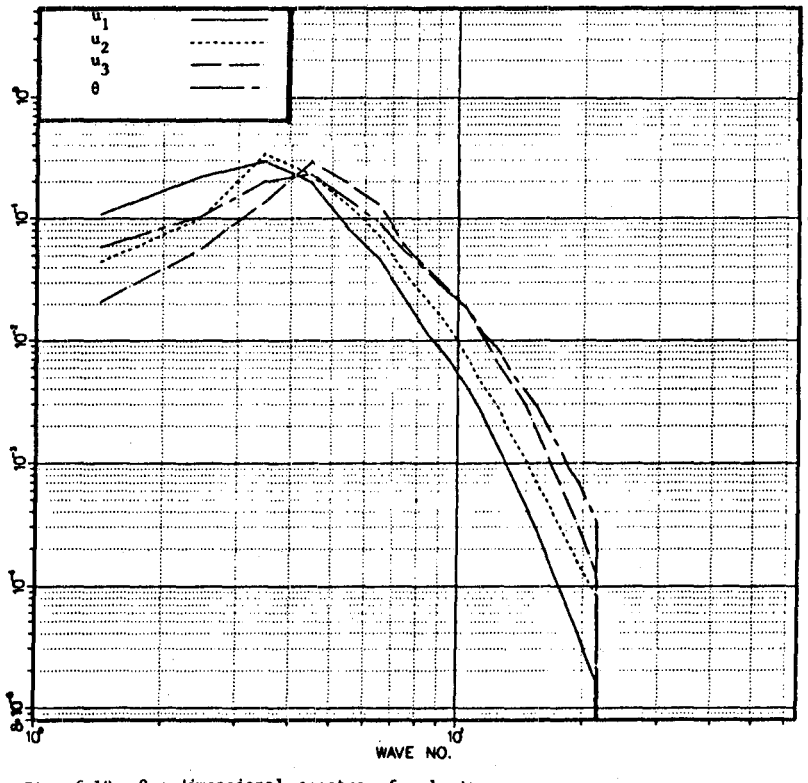

Fig. 6-12. One-dimensional spectra of velocity components and scalar in the x_1-direction.

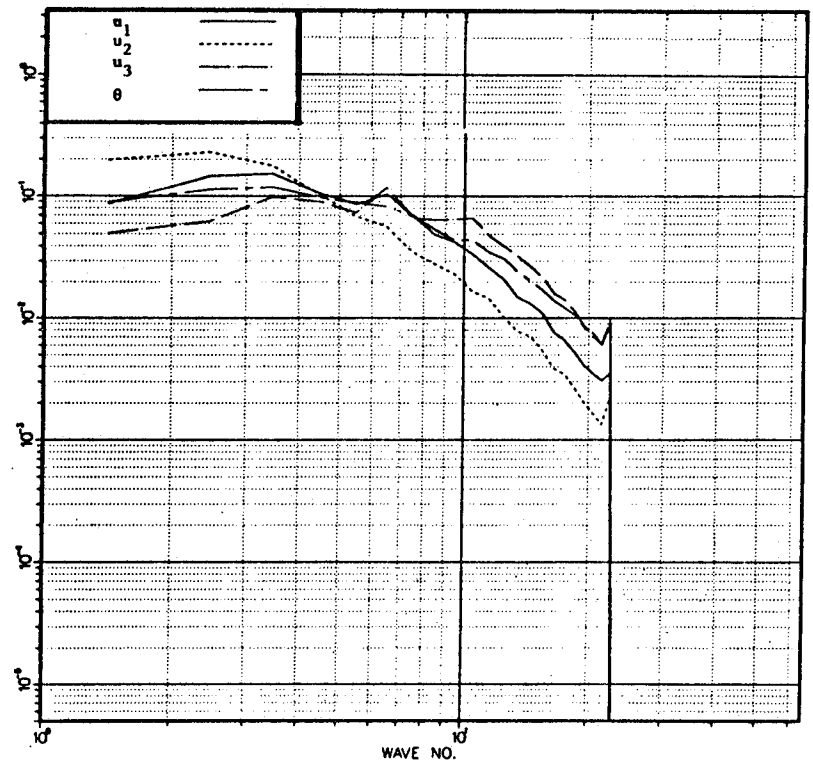

Fig. 6-13. One-dimensional spectra of velocity components and scalar in the x_2-direction.

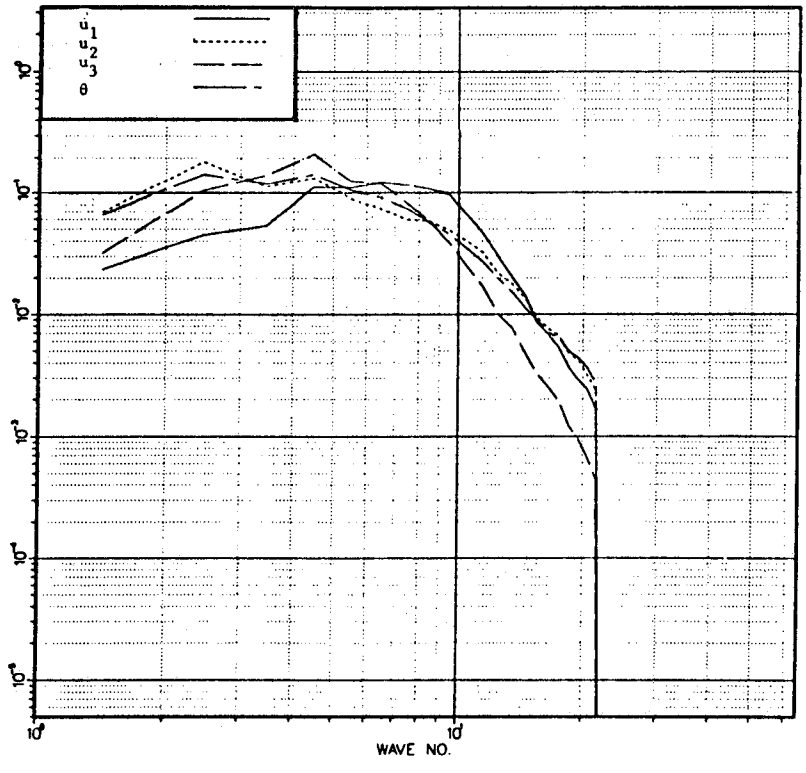

Fig. 6-14. One-dimensional spectra of velocity components and scalar in the x_3-direction.

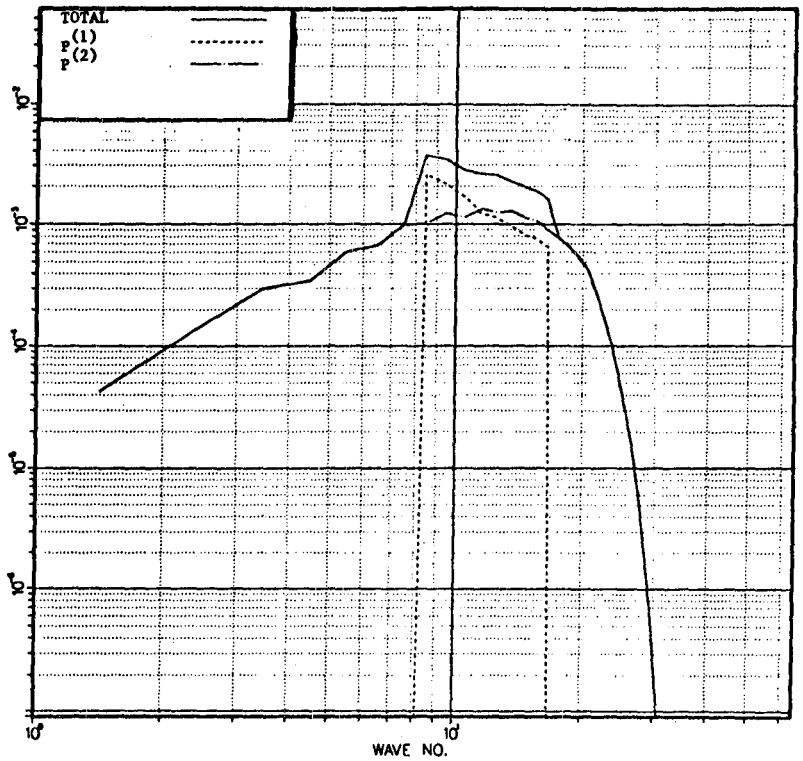

Fig. 6-15. Three-dimensional spectra of two components of pressure and total pressure at St = 0.0.

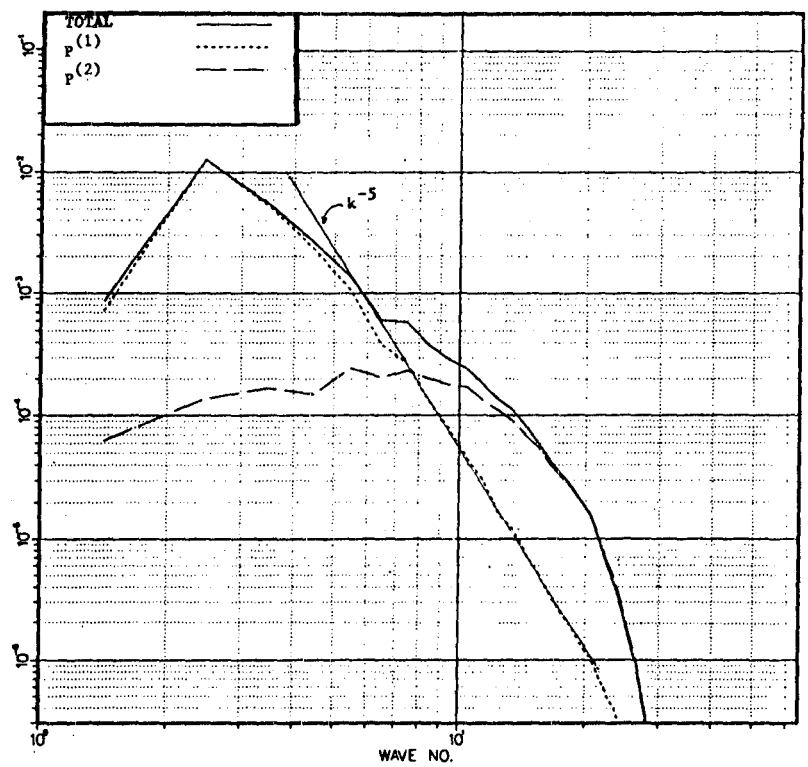

Fig. 6-16. Three-dimensional spectra of the components of pressure and total pressure at St = 4.0.

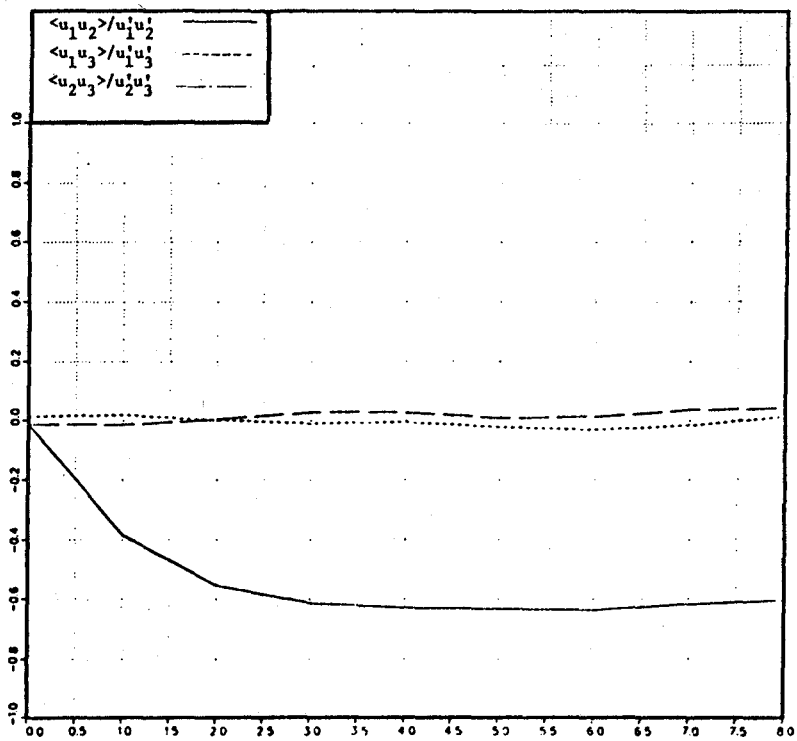

Fig. 6-17. One-point velocity correlations as a function of time.

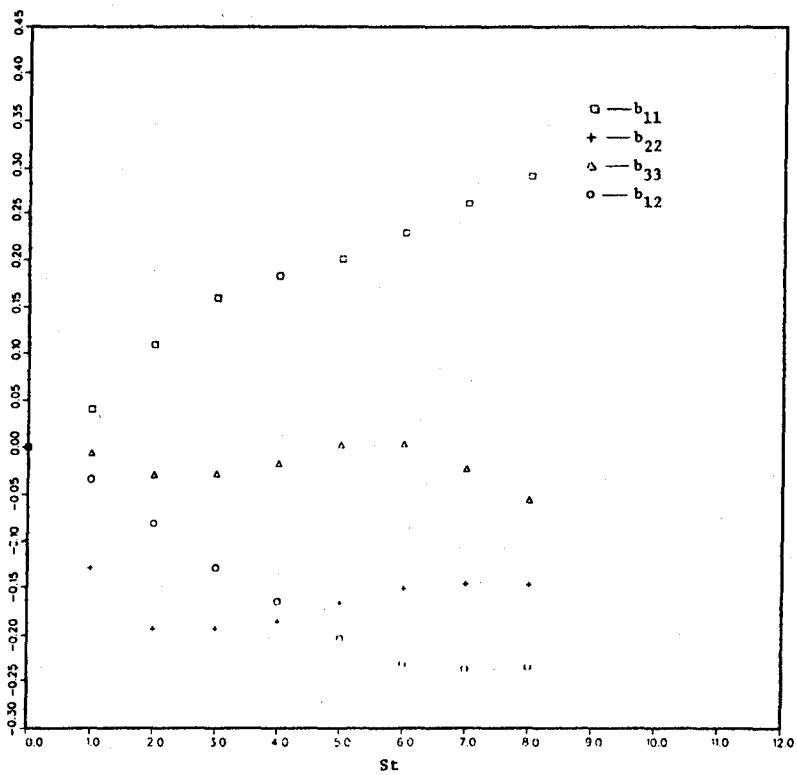

Fig. 6-18. Components of Reynolds stress anisotropy tensor as a function of time.

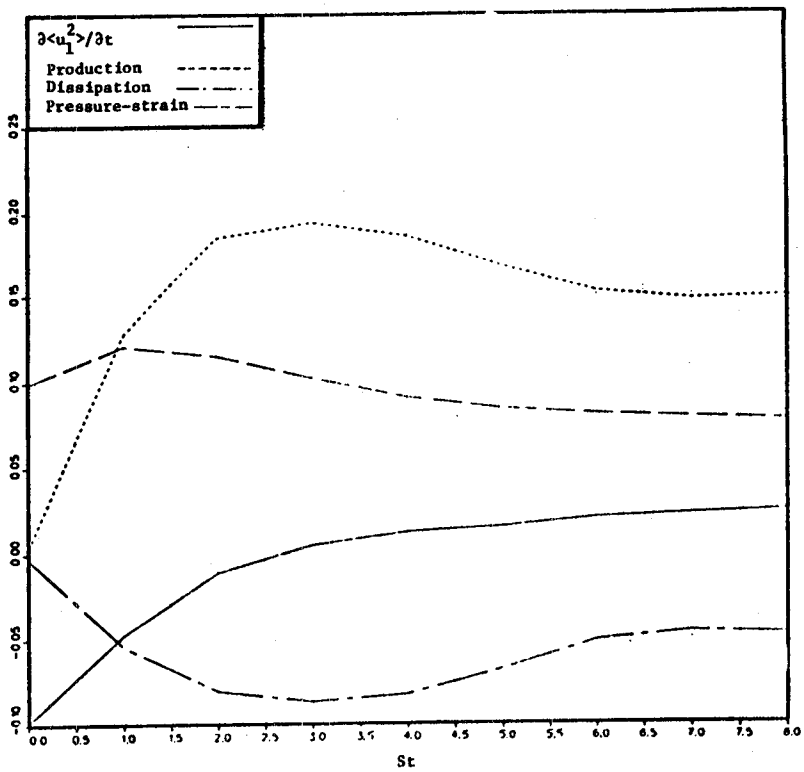

Fig. 6-19. Various terms in the $\langle u_1^2 \rangle$ equation as a function of time.

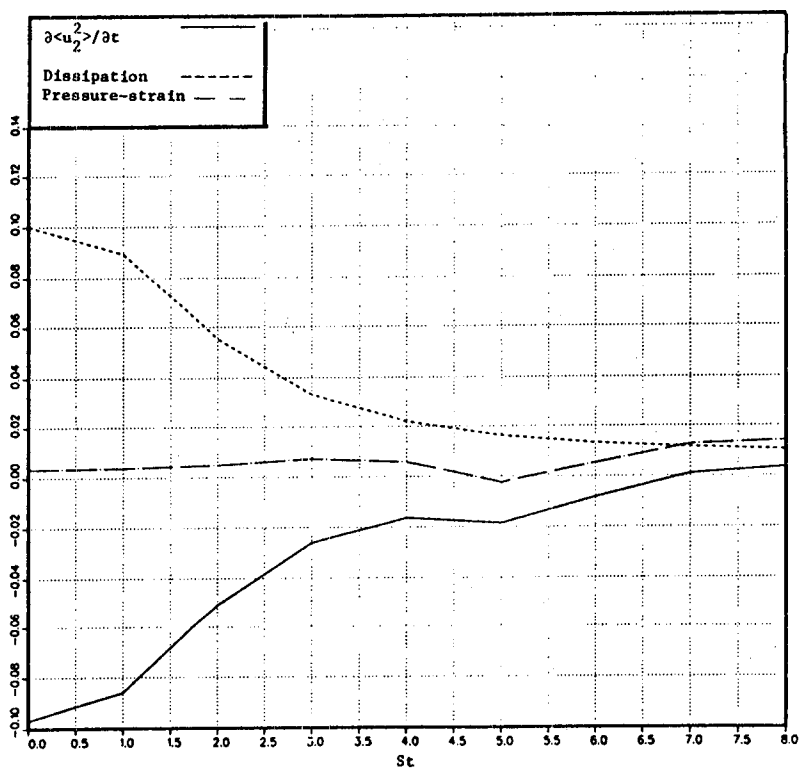

Fig. 6-20. Various terms in the $\langle u_2^2 \rangle$ equation as a function of time.

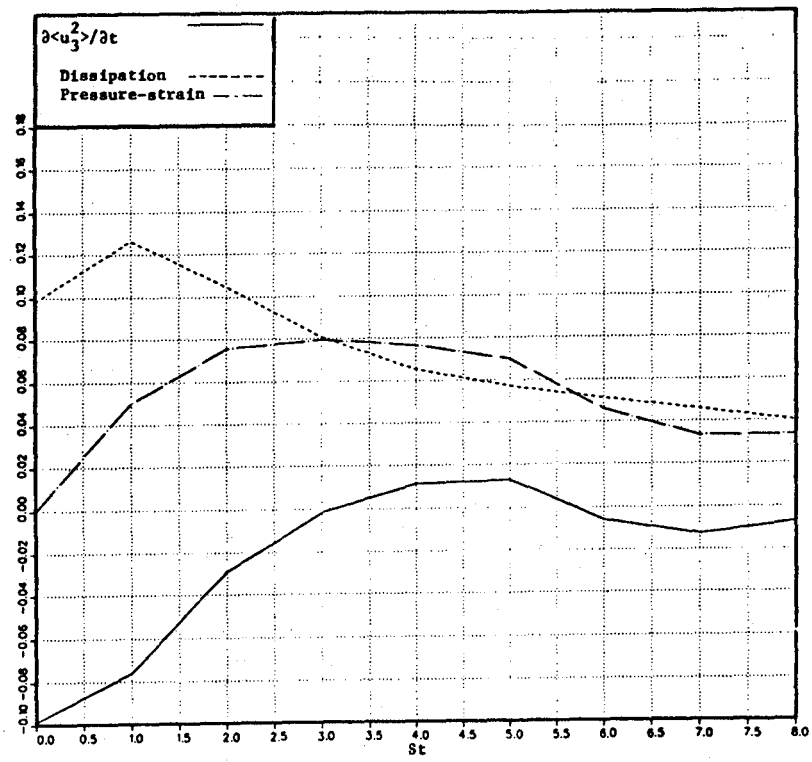

Fig. 6-21. Various terms in the $\langle u_3^2 \rangle$ equation as a function of time.

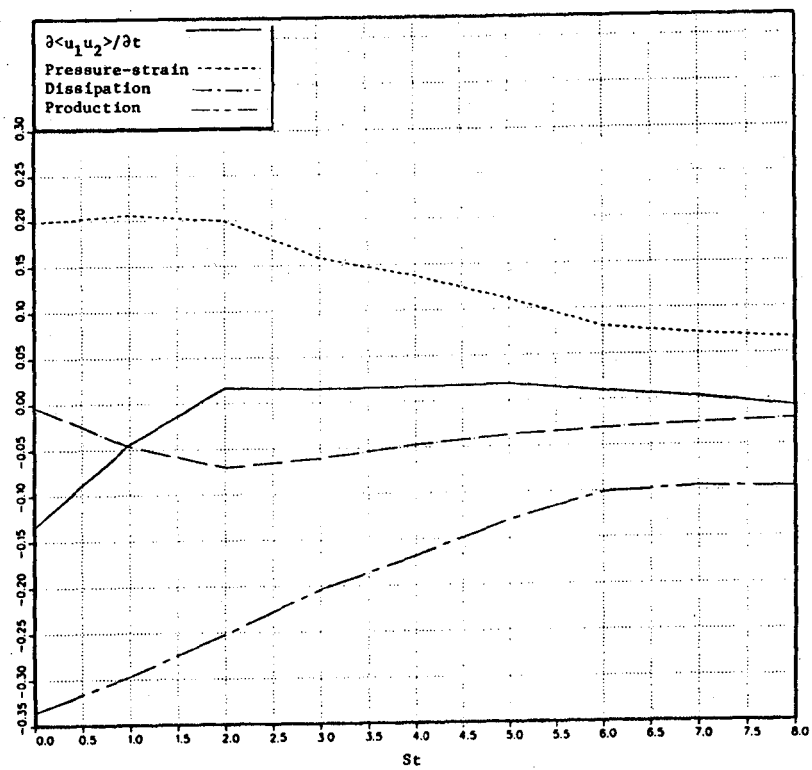

Fig. 6-22. Various terms in the $\langle -u_1 u_2 \rangle$ equation as a function of time.

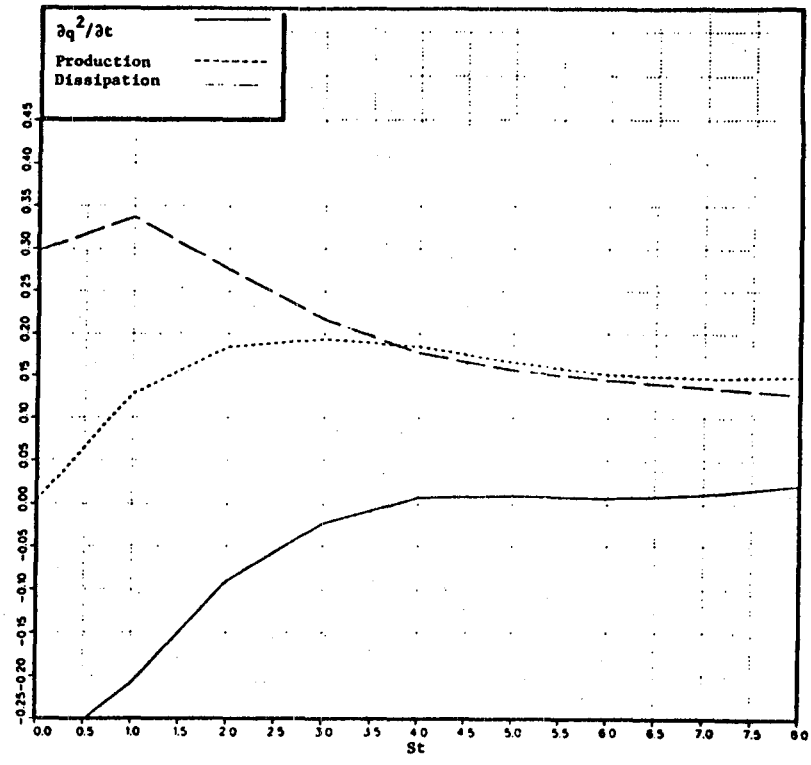

Fig. 6-23. Various terms in the turbulent kinetic energy equation as a function of time.

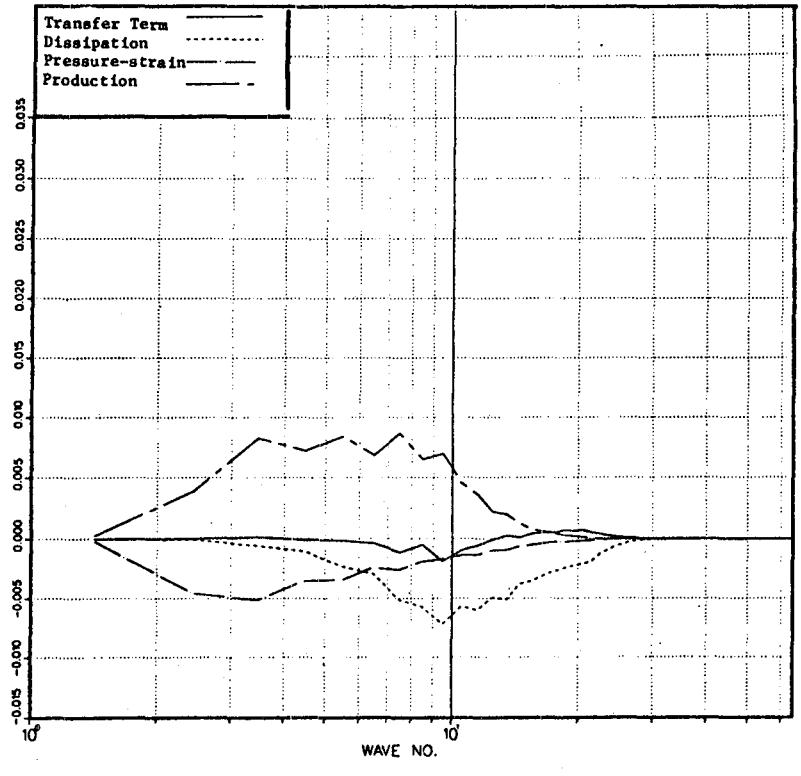

Fig. 6-24. Three-dimensional spectra of various terms in the u_1^2 equation as a function of time.

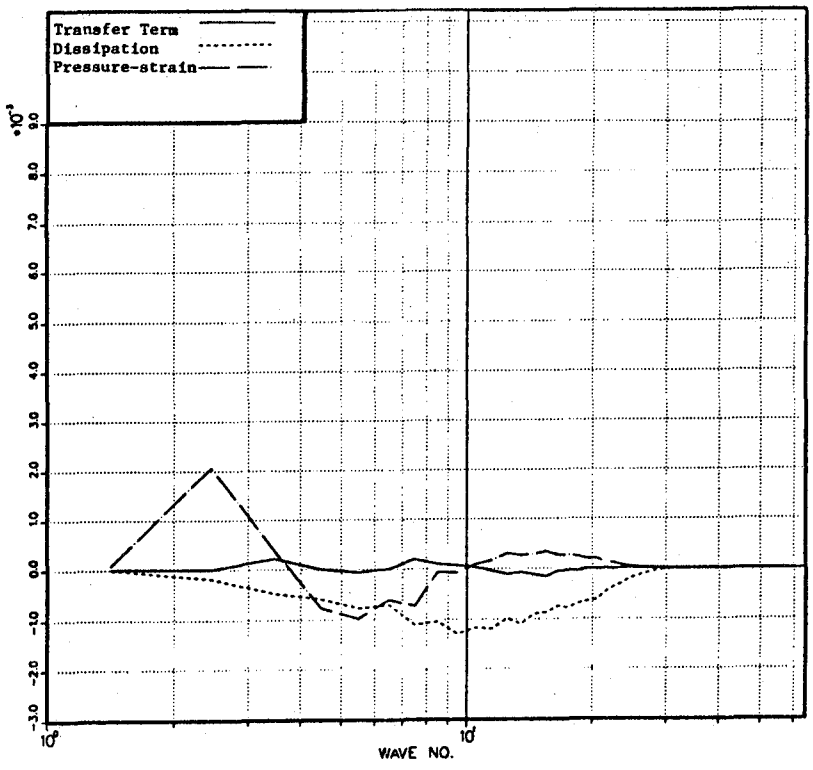

Fig. 6-25. Three-dimensional spectra of various terms in the u_2^2 equation as a function of time.

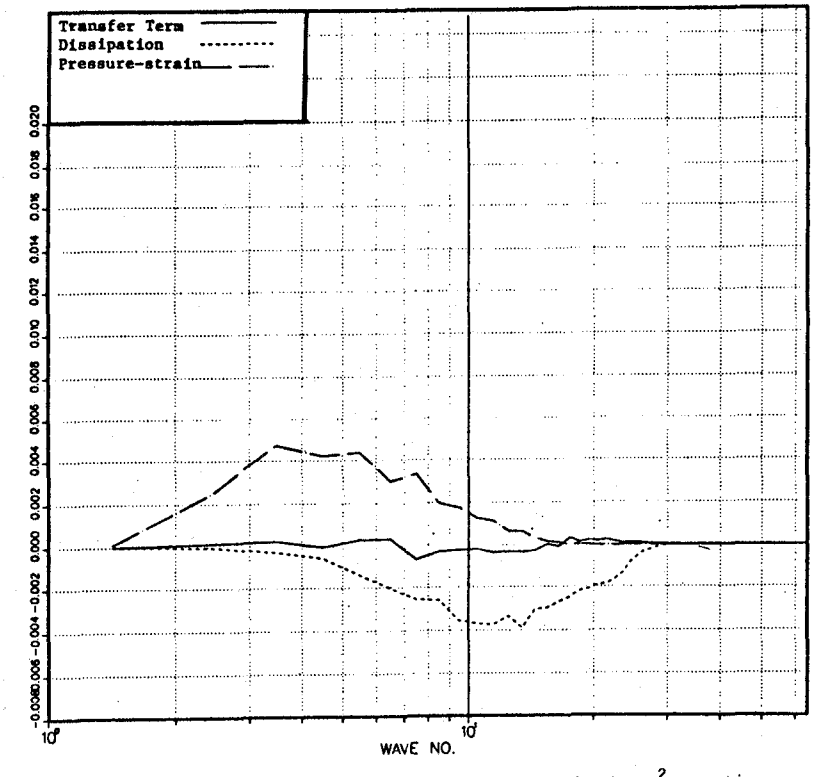

Fig. 6-26. Three-dimensional spectra of various terms in the u_3^2 equation as a function of time.

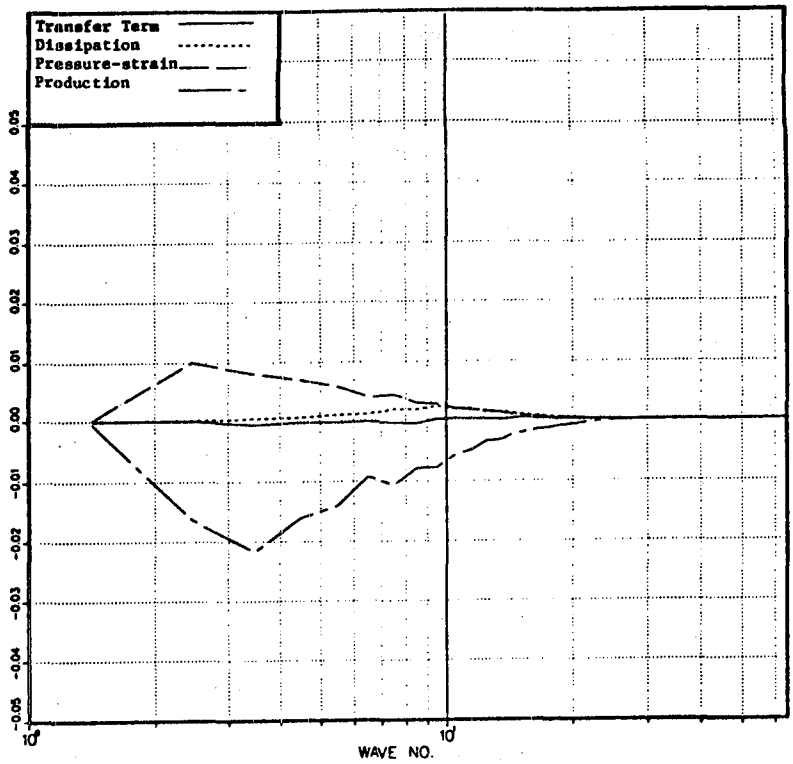

Fig. 6-27. Three-dimensional spectra of various terms in the u_1u_2 equation as a function of time.

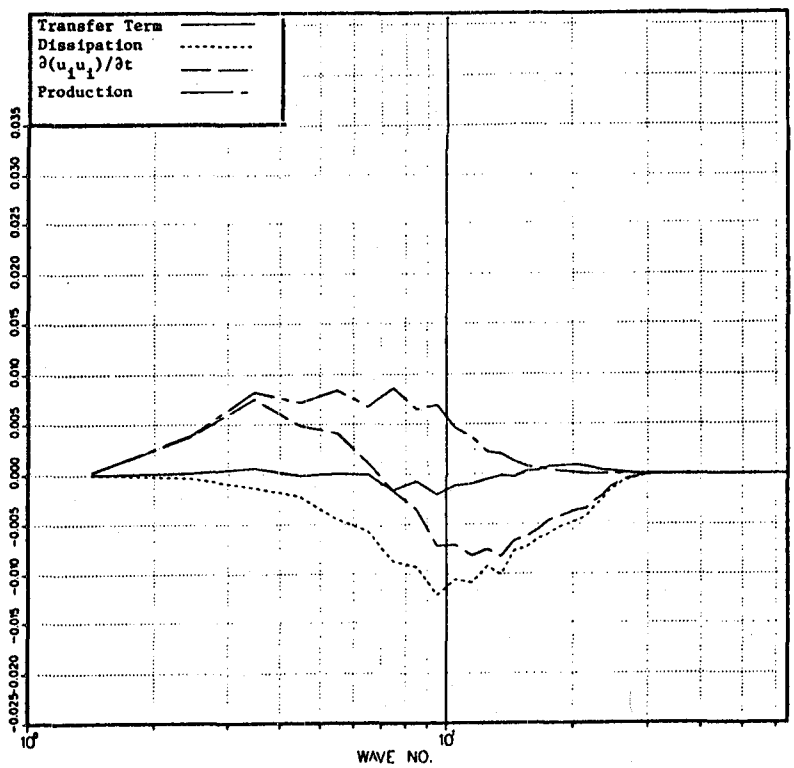

Fig. 6-28. Three-dimensional spectra of various terms in the $u_iu_i/2$ equation as a function of time.

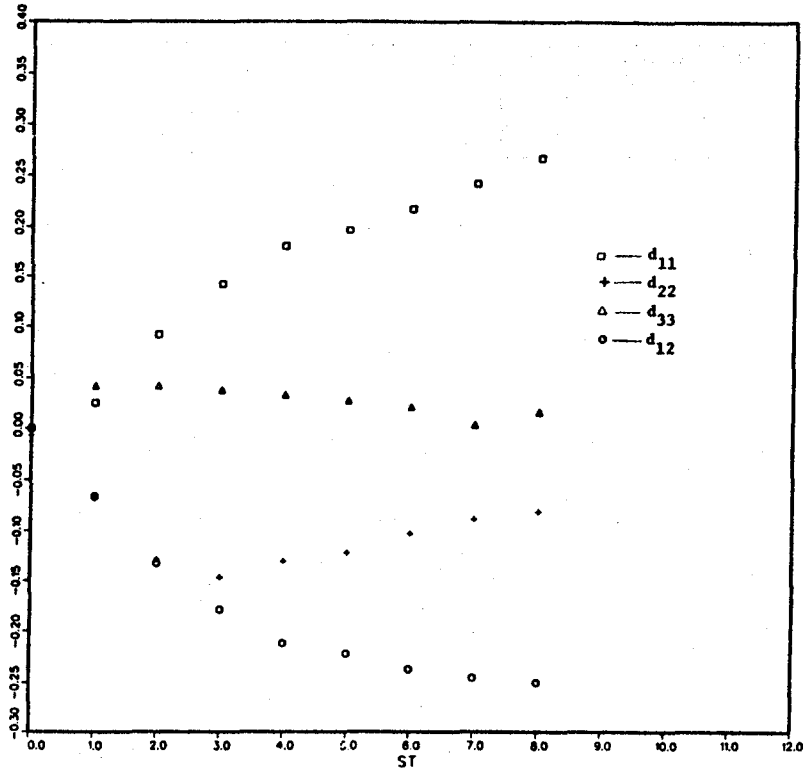

Fig. 6-29. Components of dissipation anisotropy tensor as a function of time.

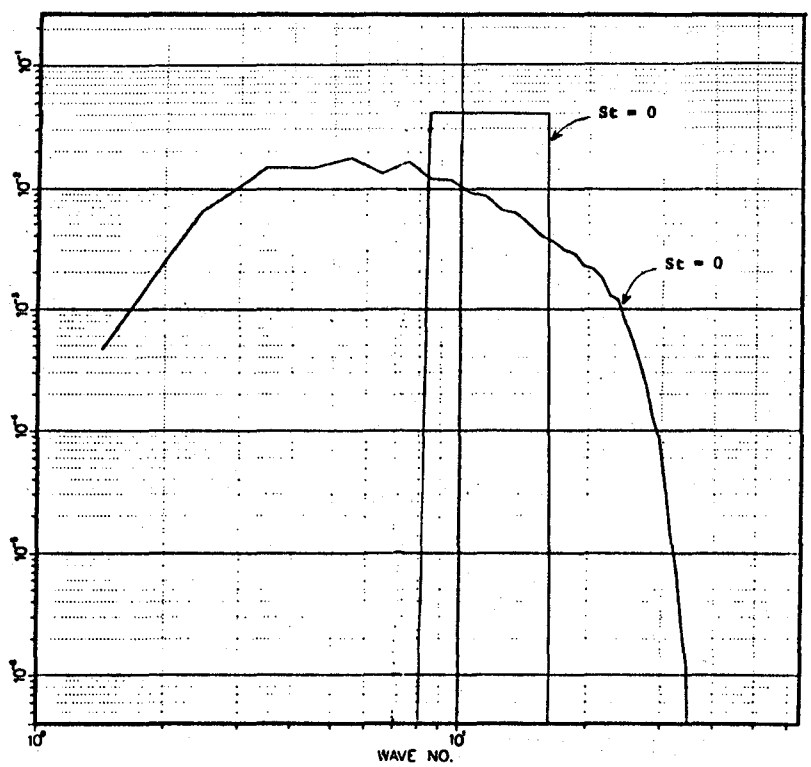

Fig. 6-30. Three-dimensional spectra of the scalar fluctuations at different times.

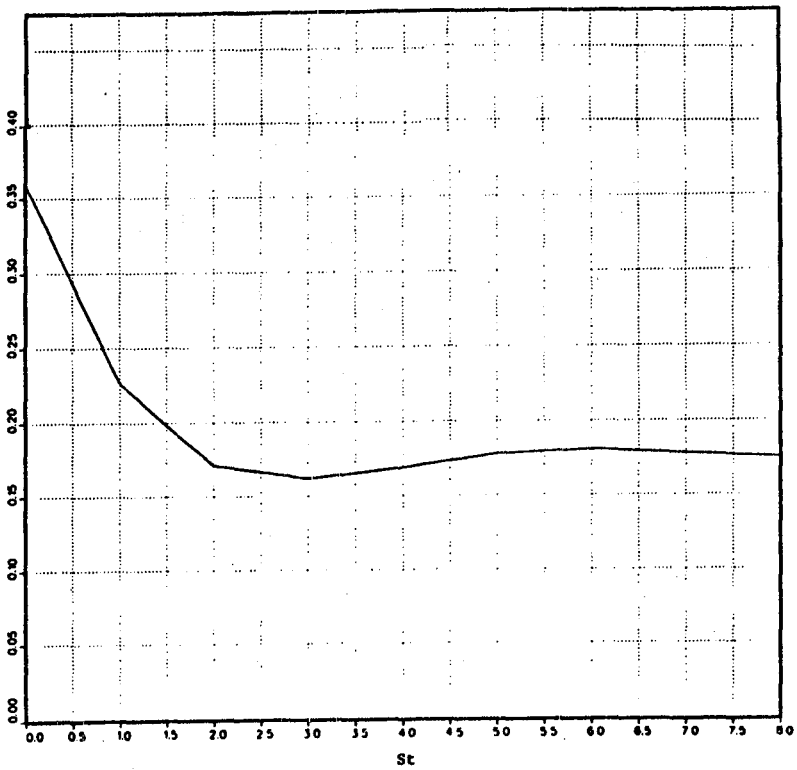

Fig. 6-31. The scalar-fluctuation intensity as a function of time.

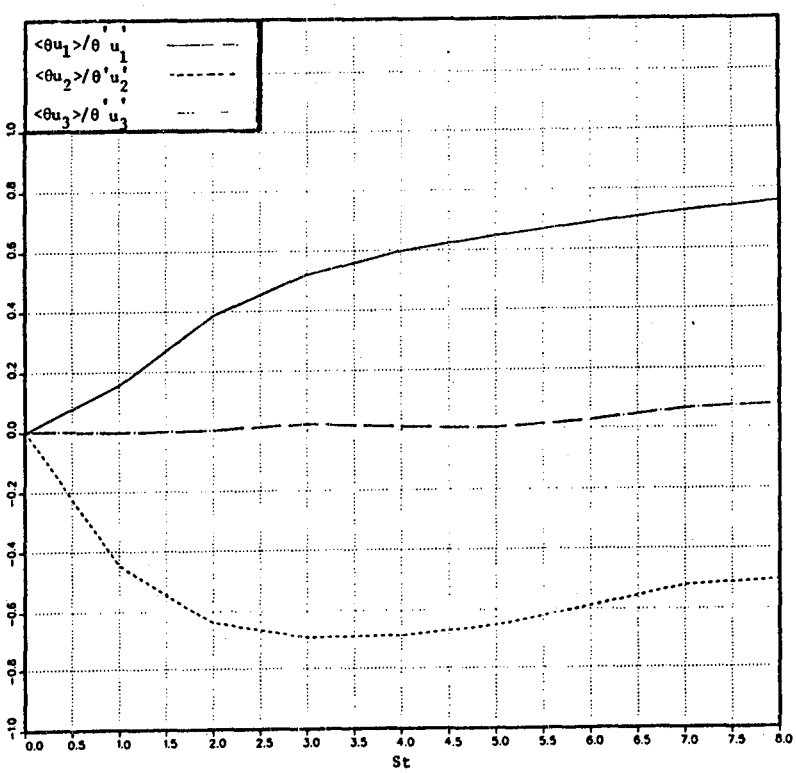

Fig. 6-32. One-point velocity scalar correlations as a function of time.

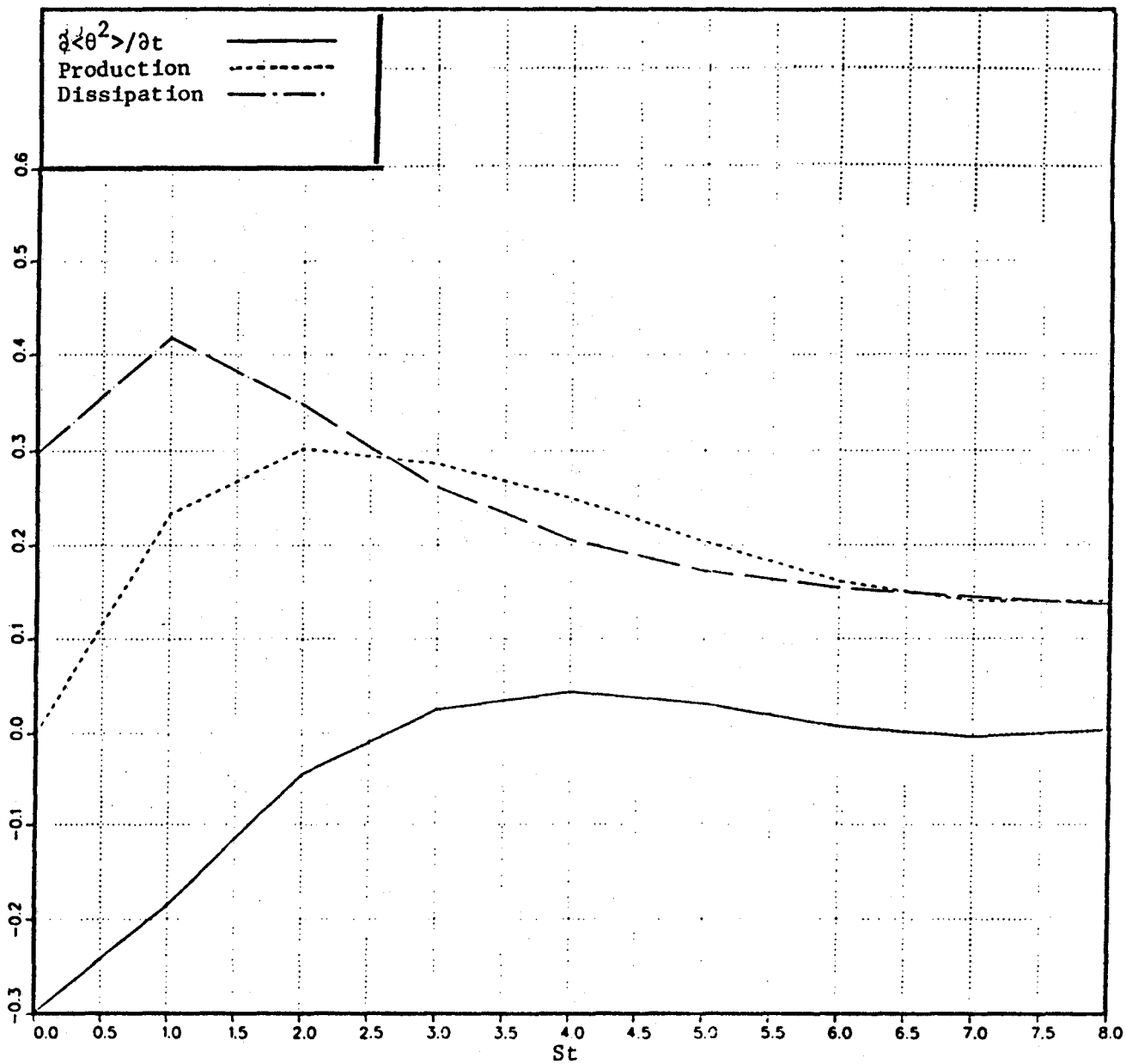

Fig. 6-33. Various terms in the $\langle \theta^2 \rangle$ equation as a function of time.

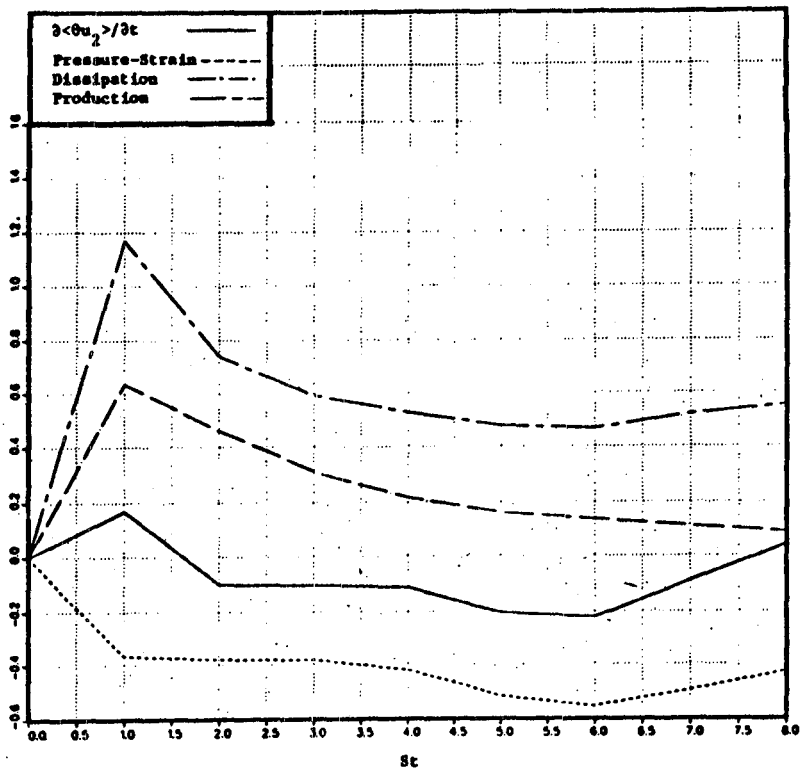

Fig. 6-34. Various terms in the $\langle \theta u_2 \rangle$ equation as a function of time.

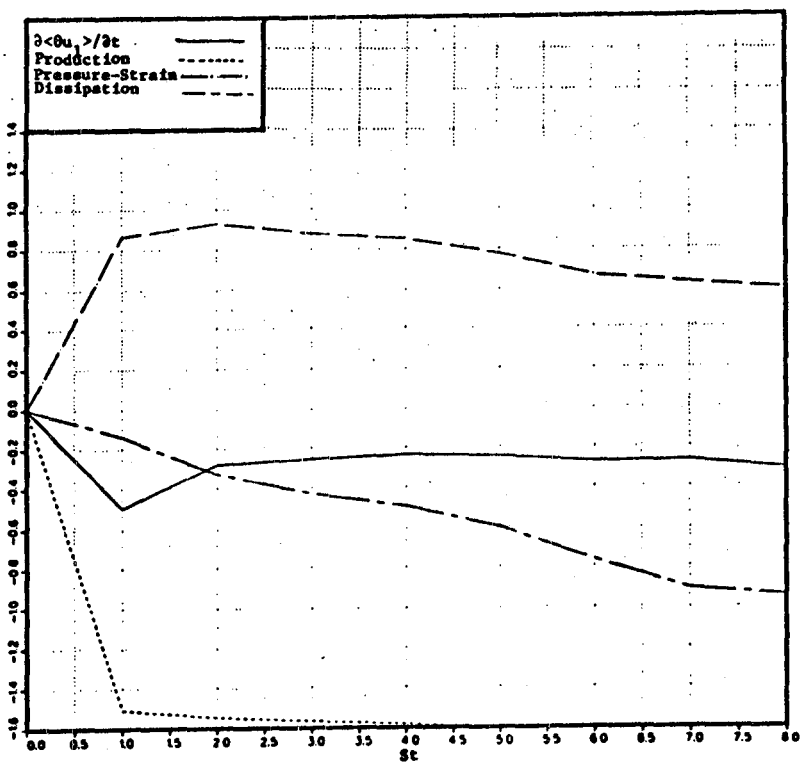

Fig. 6-35. Various terms in the $\langle \theta u_1 \rangle$ equation as a function of time.

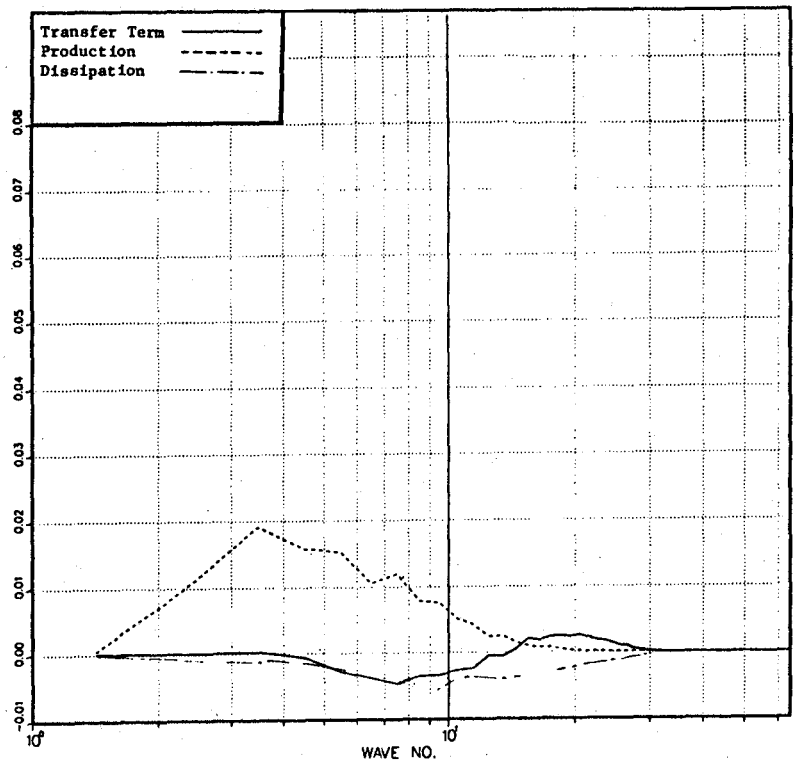

Fig. 6-36. Three-dimensional spectra of various terms in the θ^2 equation.

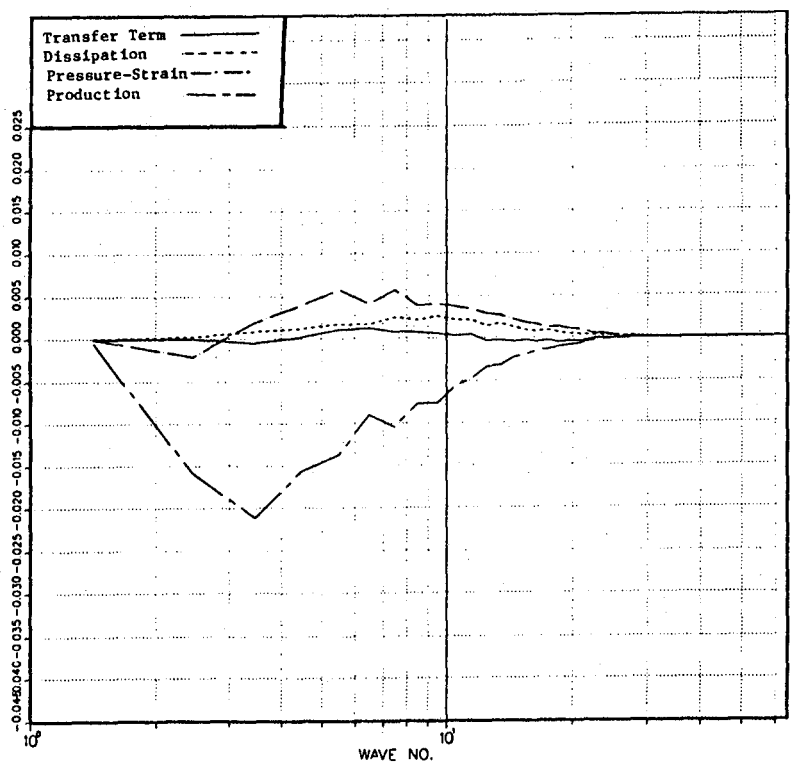

Fig. 6-37. Three-dimensional spectra of various terms in the θu_2 equation.

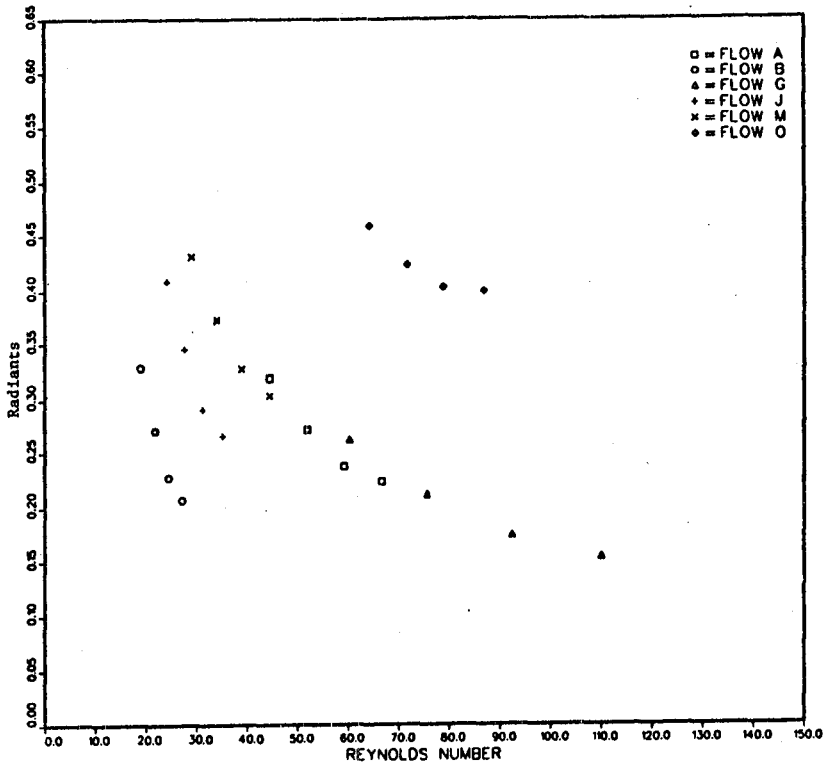

Fig. 6-38. The angle of the principal axis of the Reynolds stress tensor as a function of Reynolds number (Re_λ)

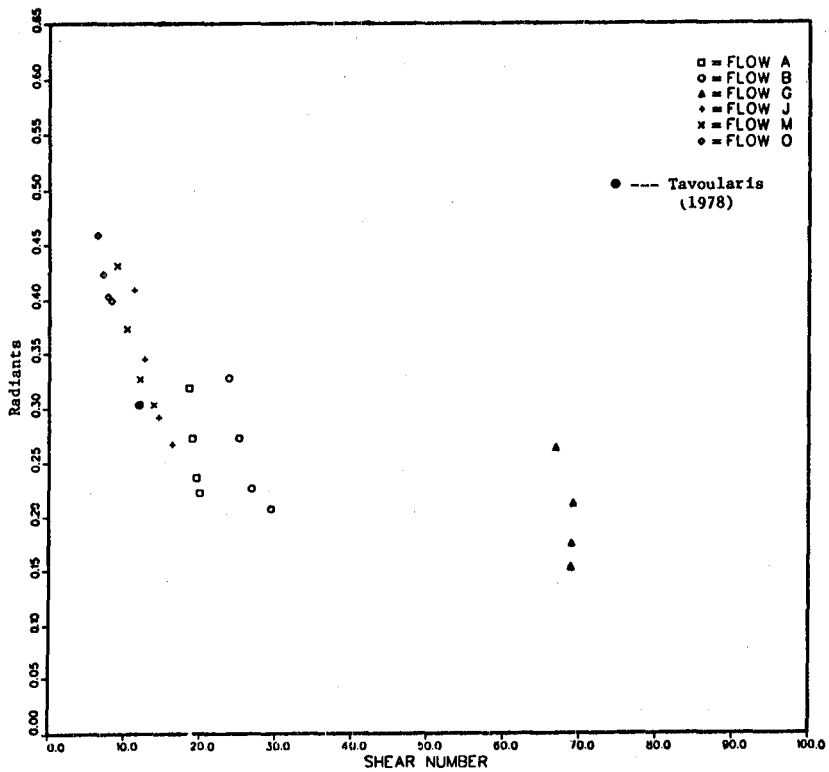

Fig. 6-39. The angle of the principal axis of the Reynolds stress tensor as a function of shear number

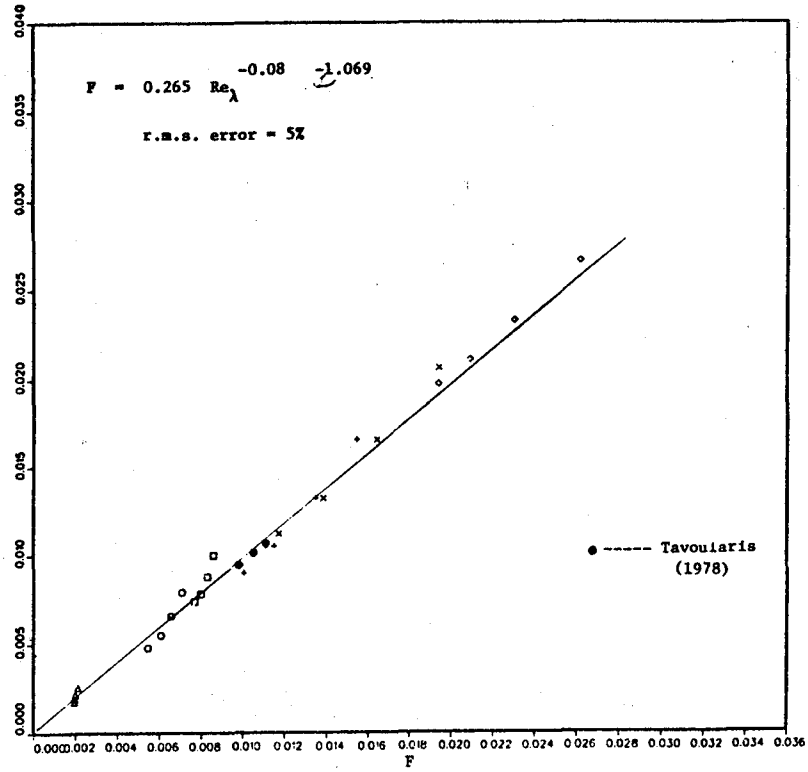

Fig. 6-40. The constant for the eddy viscosity model ($C = \nu_T/qL$) as a function of the fitting function.

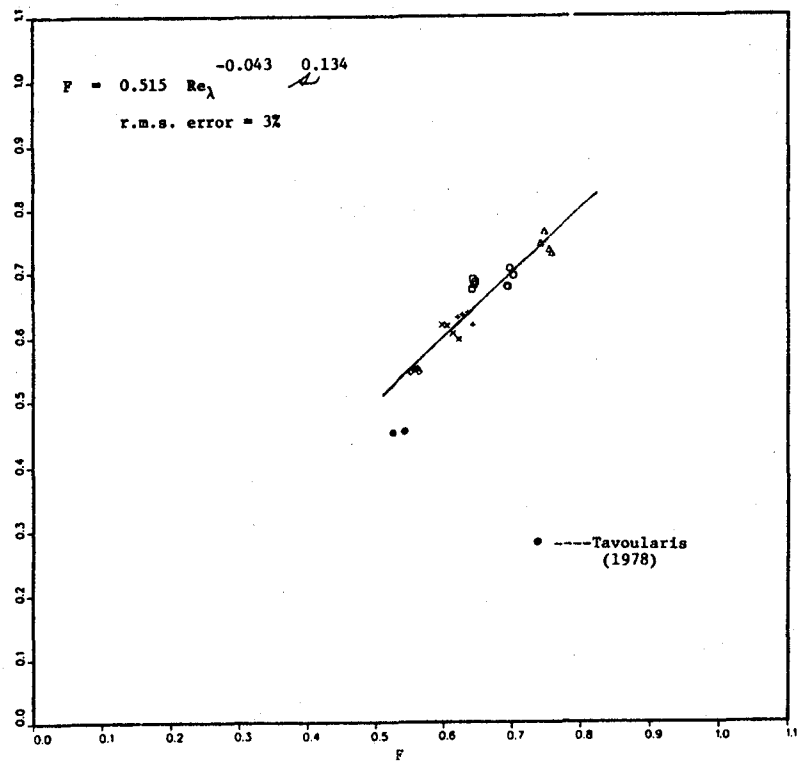

Fig. 6-41. Reynolds shear stress correlation as a function of the fitting function.

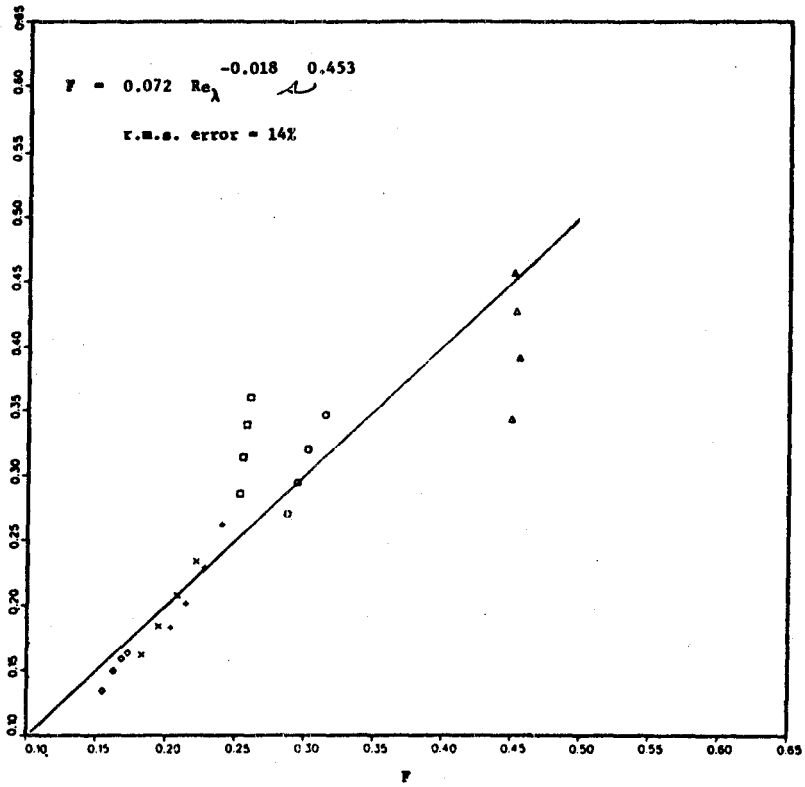

Fig. 6-42. Reynolds stress anisotropy, b_{11}, as a function of the fitting function.

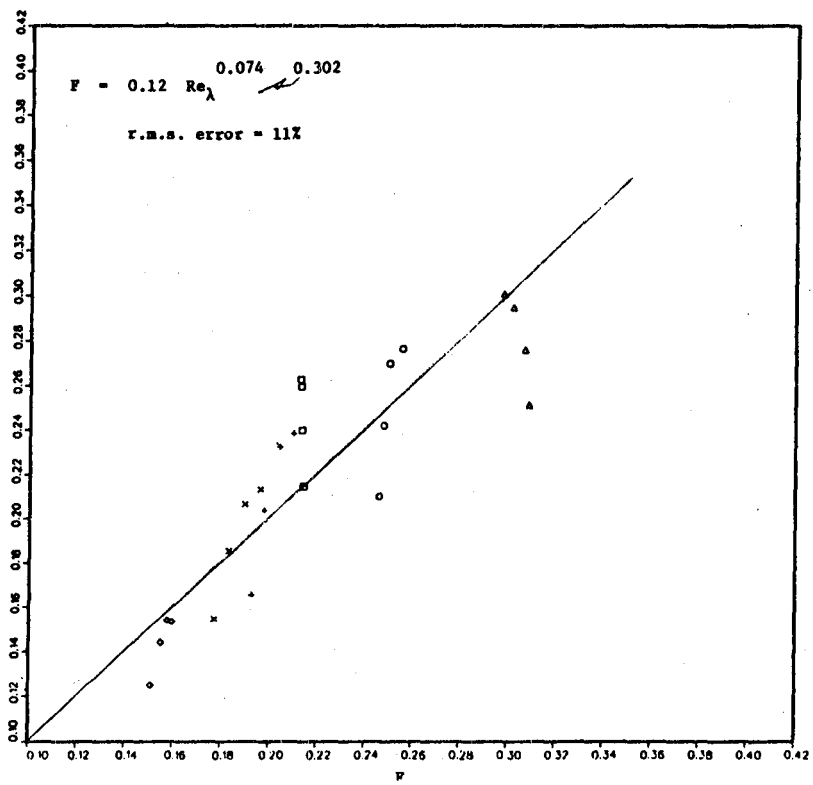

Fig. 6-43. Reynolds stress anisotropy, b_{22}, as a function of the fitting function.

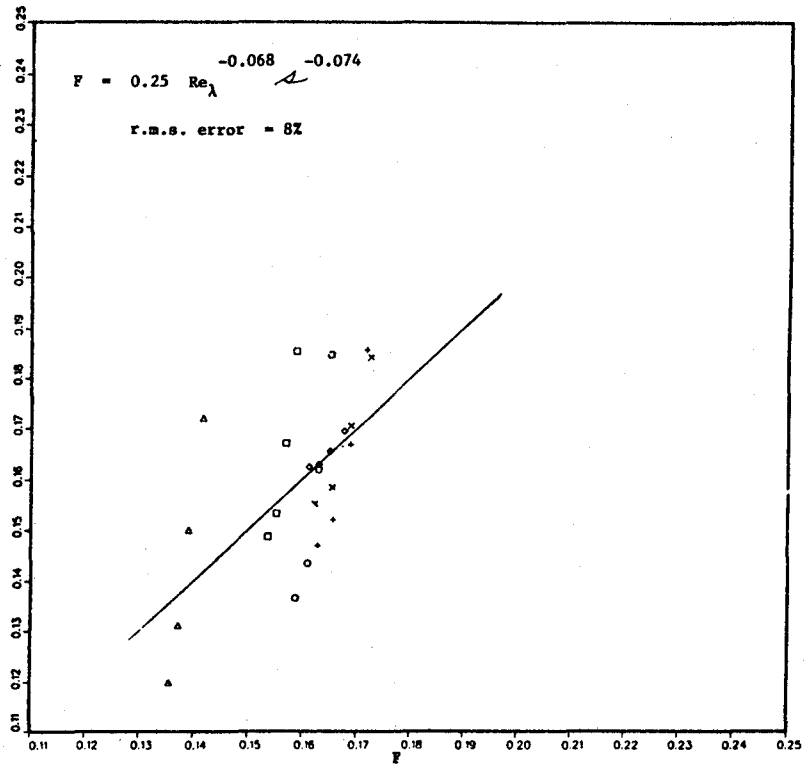

Fig. 6-44. Reynolds stress anisotropy, b_{12}, as a function of the fitting function.

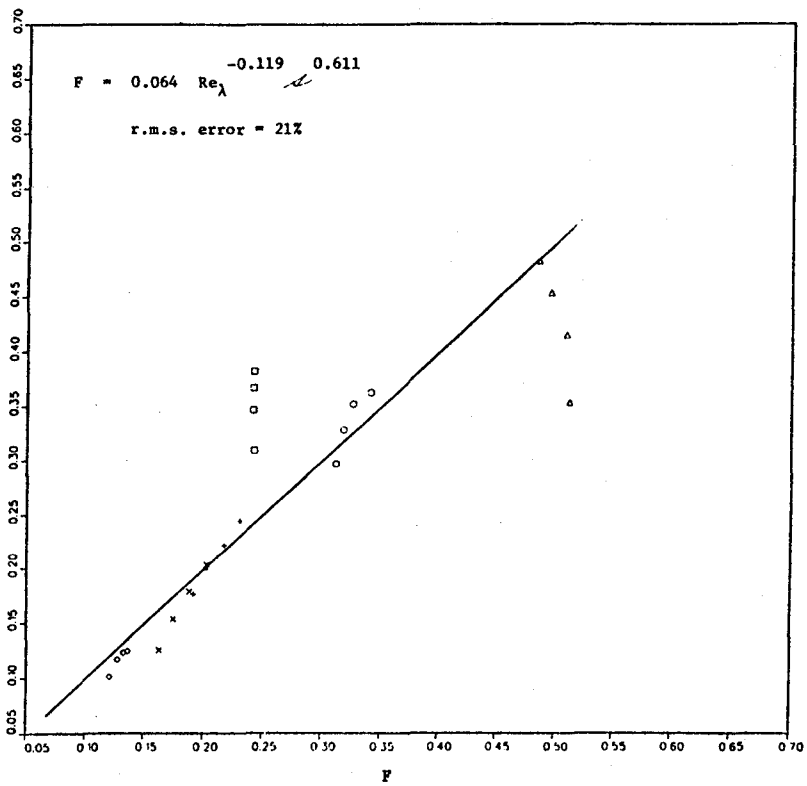

Fig. 6-45. Dissipation anisotropy, d_{11}, as a function of the fitting function.

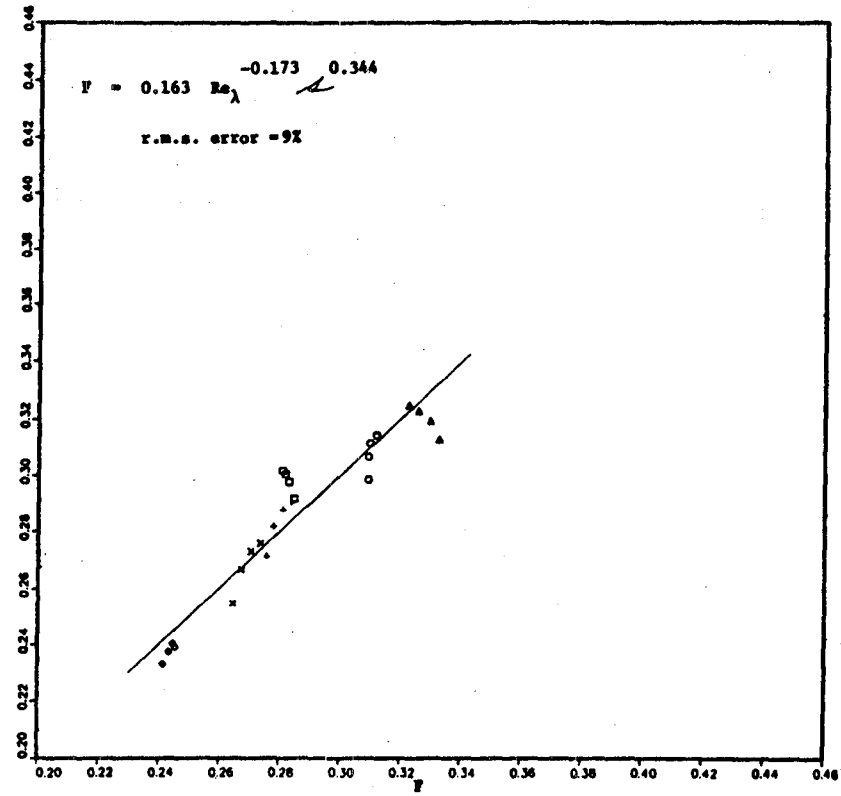

Fig. 6-46. Dissipation anisotropy, d_{22}, as a function of the fitting function.

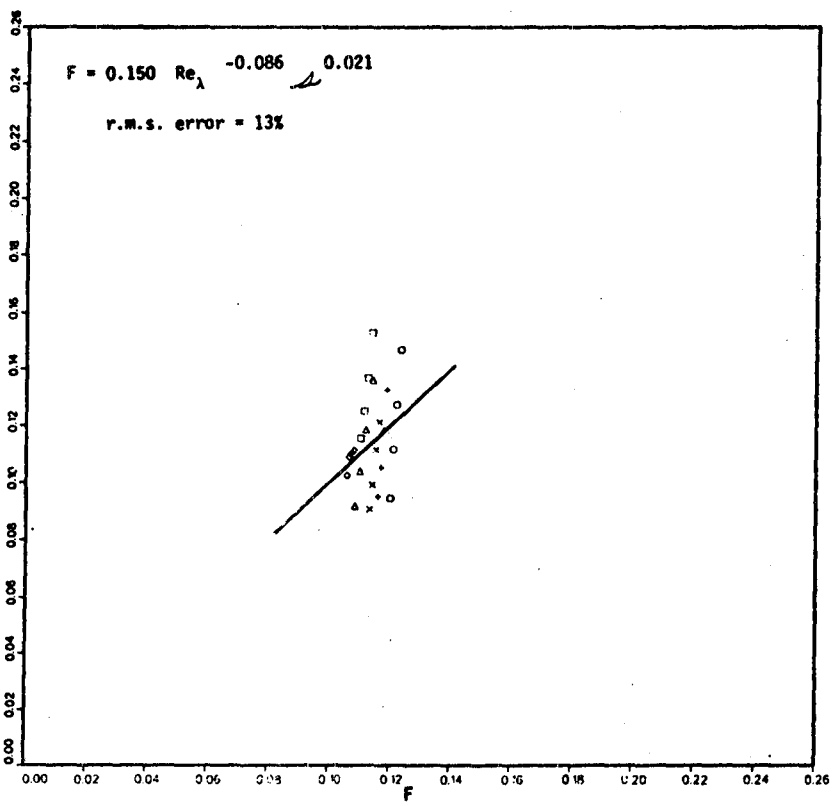

Fig. 6-47. Dissipation anisotropy, d_{12}, as a function of the fitting function.

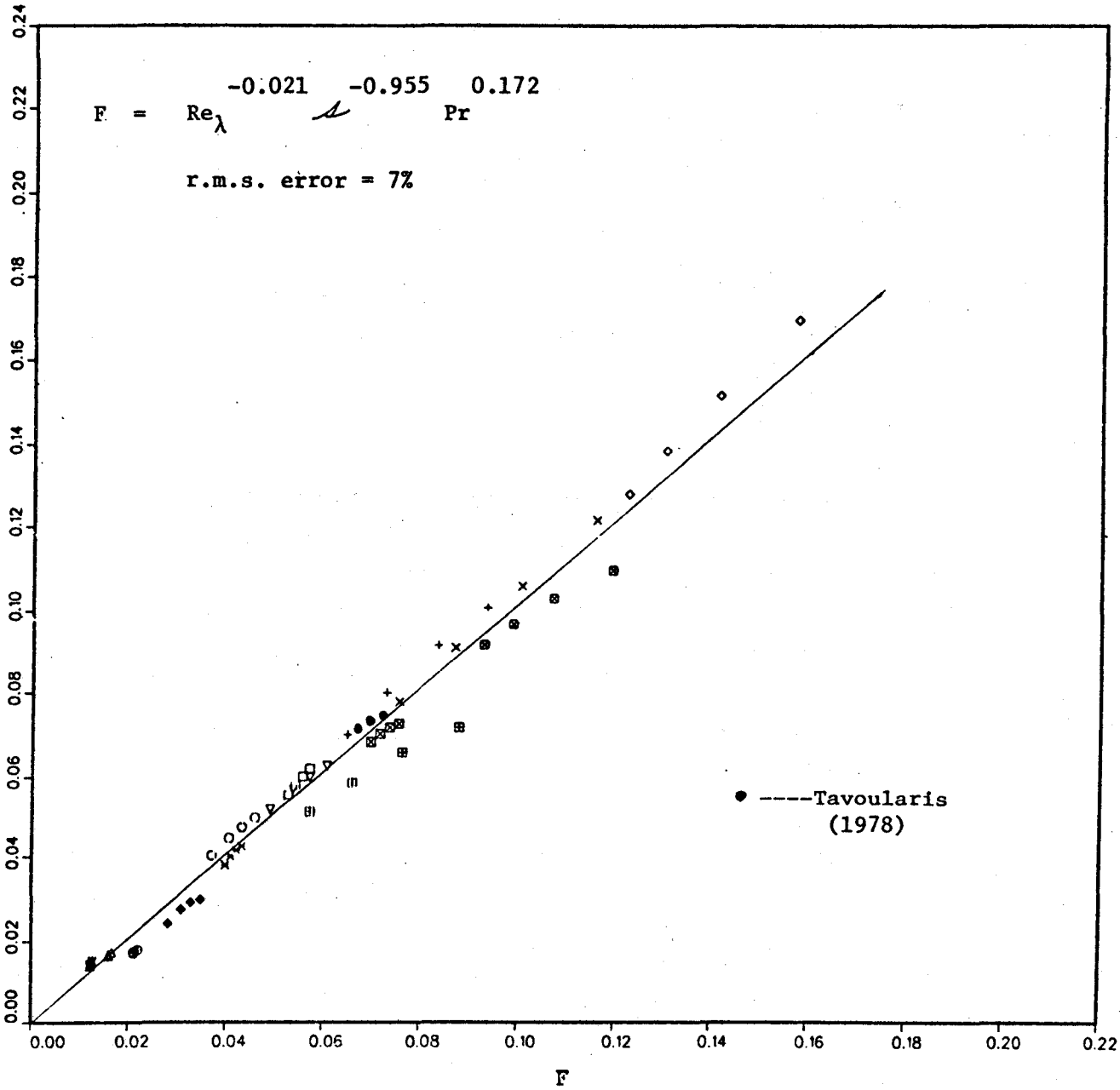

Fig. 6-48. Nondimensional scalar fluctuations as a function of the fitting function.

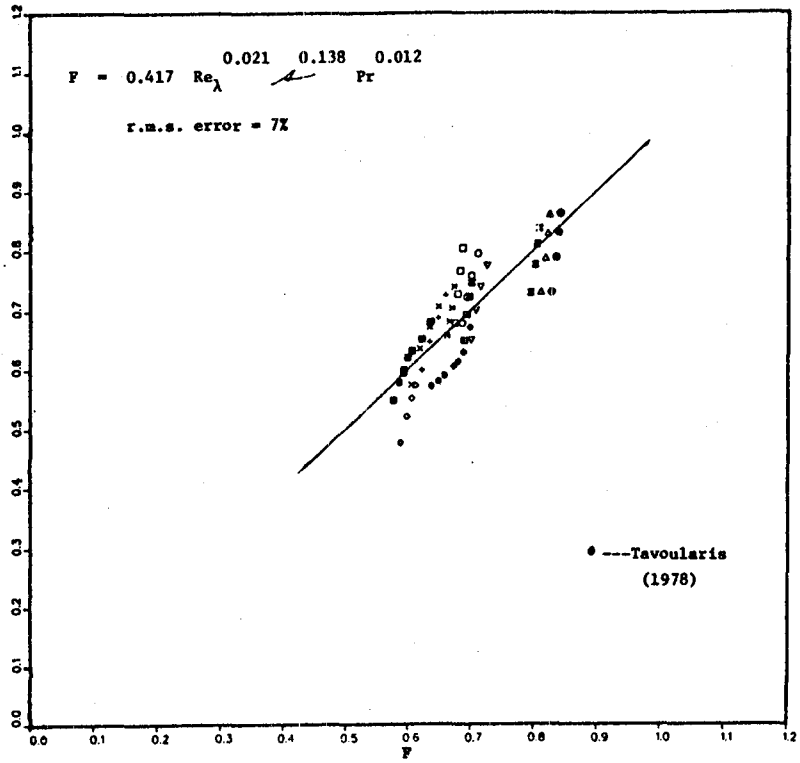

Fig. 6-49. One-point velocity-scalar correlation, $\langle \theta u_1 \rangle / \theta' u_1'$, as a function of the fitting function.

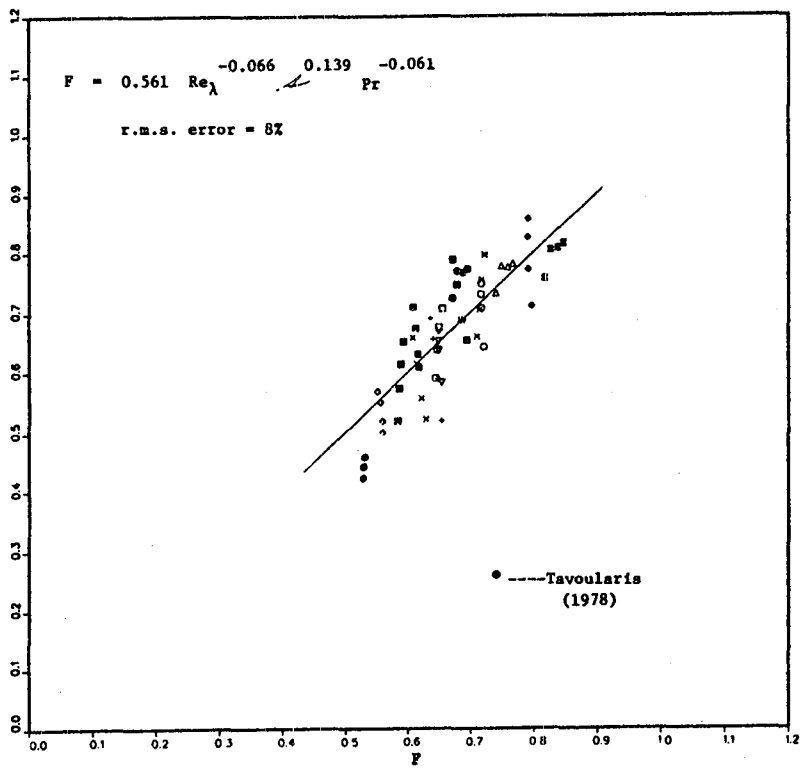

Fig. 6-50. One-point velocity-scalar correlation, $\langle \theta u_2 \rangle / \theta' u_2'$, as a function of the fitting function.

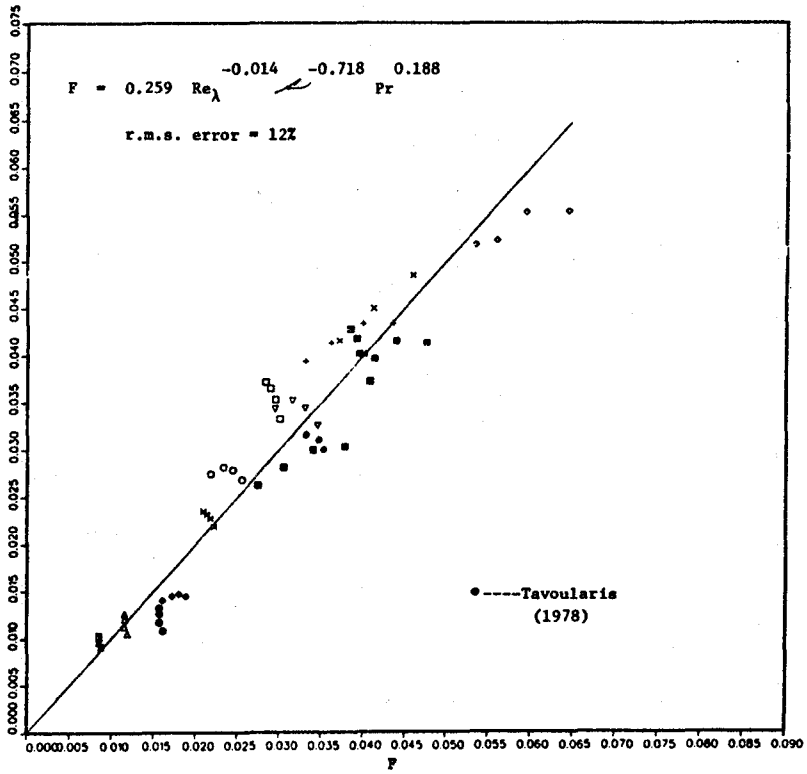

Fig. 6-51. Normalized turbulent eddy diffusivity, D_{12}/qL, as a function of the fitting function.

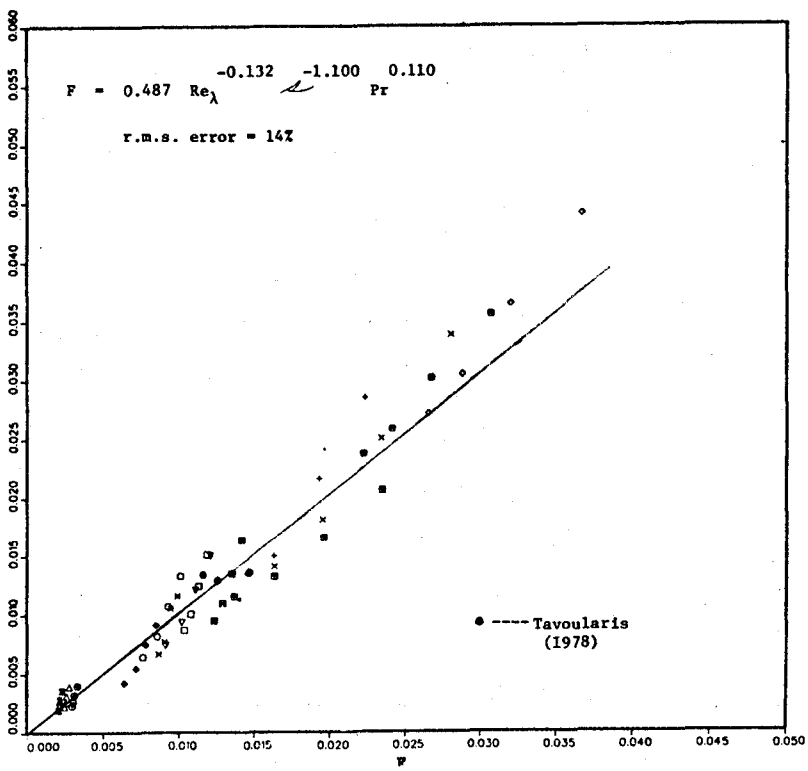

Fig. 6-52. Normalized turbulent eddy diffusivity, D_{22}/qL, as a function of the fitting function.

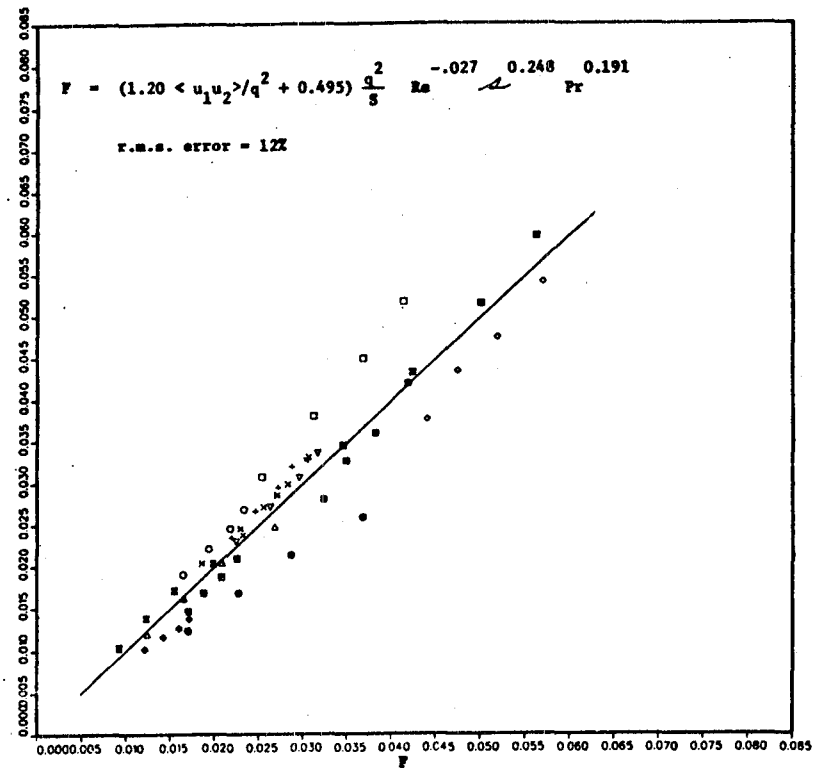

Fig. 6-53. Turbulent eddy diffusivity, D_{12}, as a function of its model.

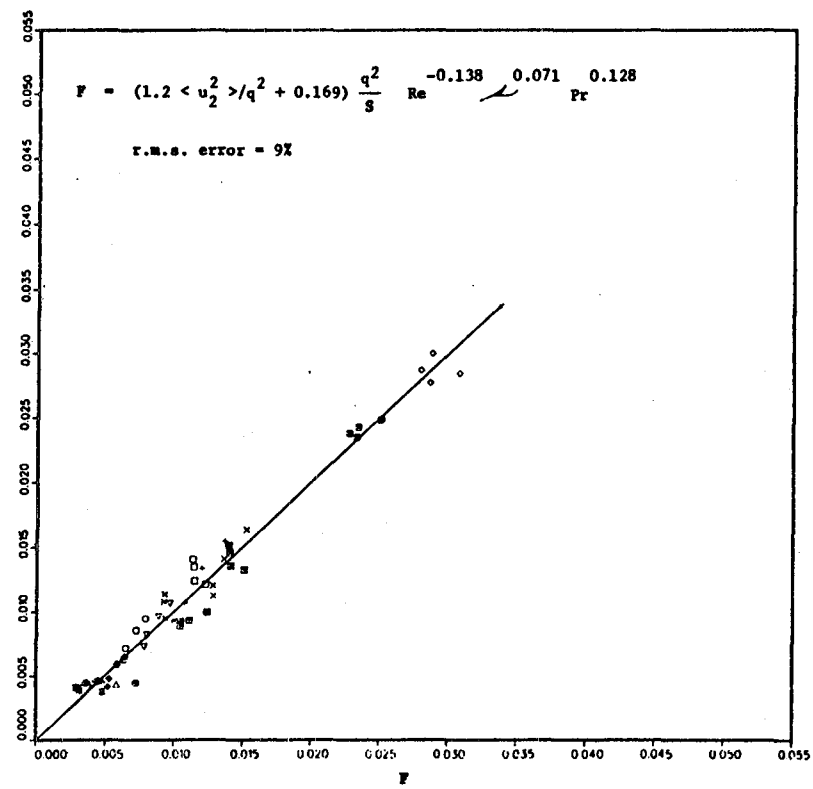

Fig. 6-54. Turbulent eddy diffusivity, D_{22}, as a function of its model.

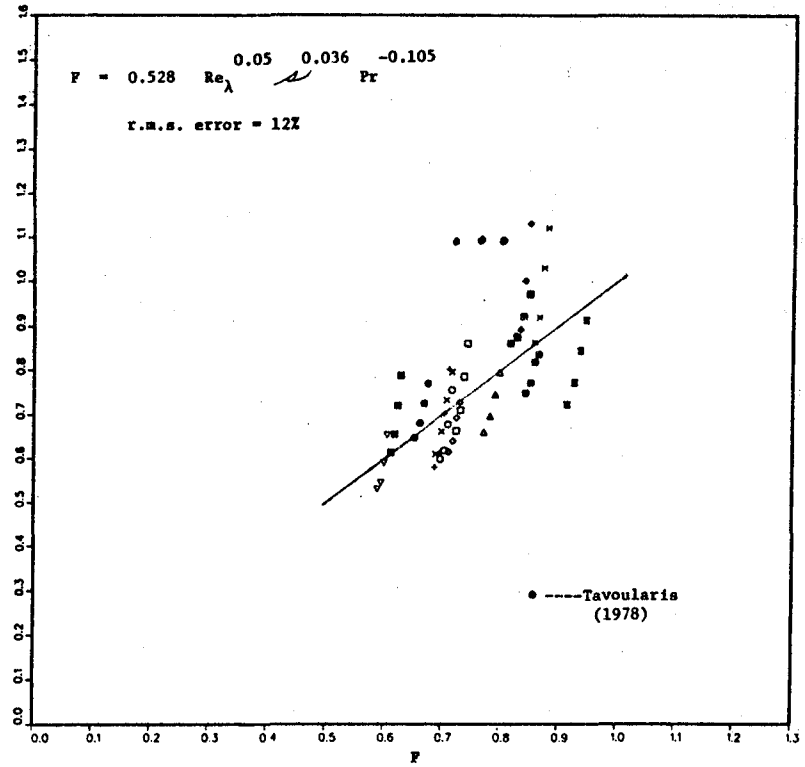

Fig. 6-55. Turbulent Prandtl number as a function of the fitting function.

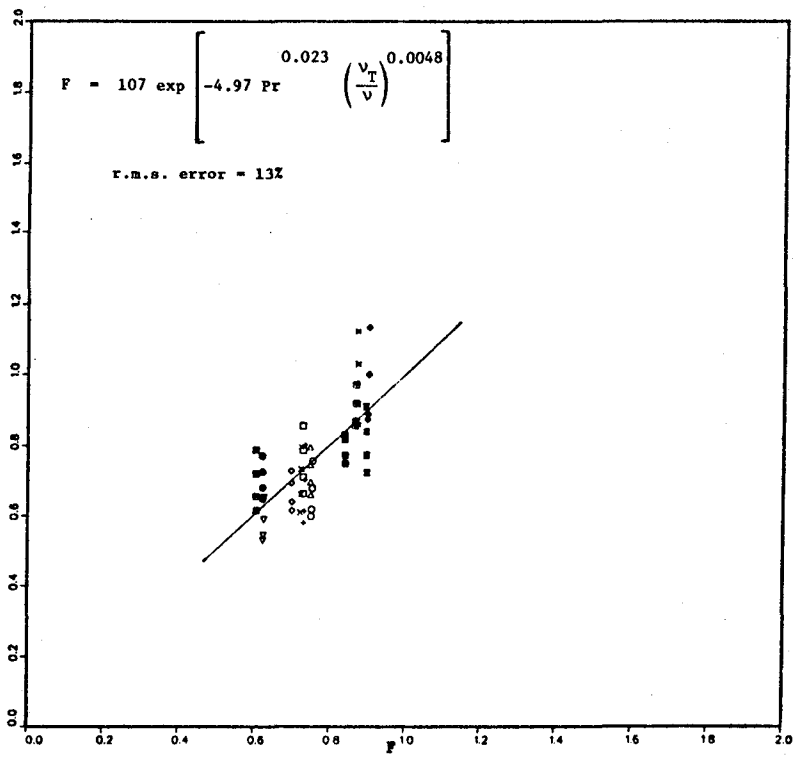

Fig. 6-56. Turbulent Prandtl number as a function of the Reynolds model.

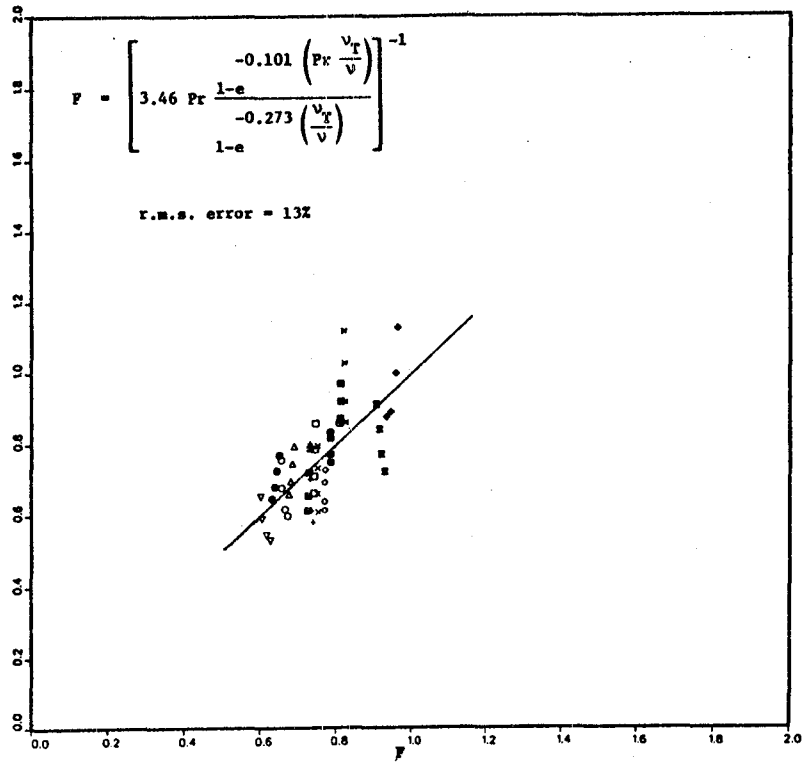

Fig. 6-57. Turbulent Prandtl number as a function of the Wassel model.

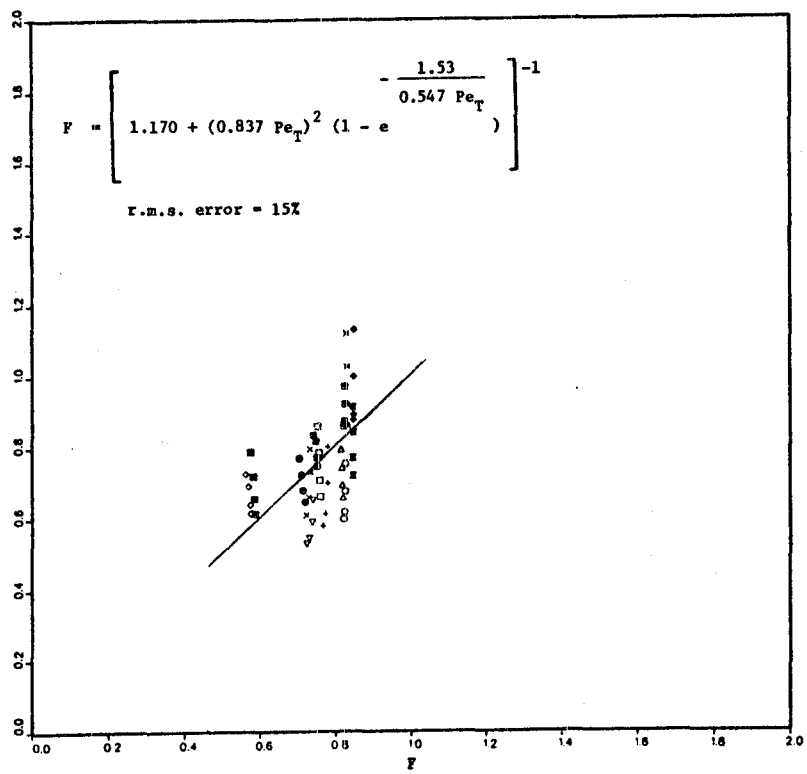

Fig. 6-58. Turbulent Prandtl number as a function of the Crawford model.

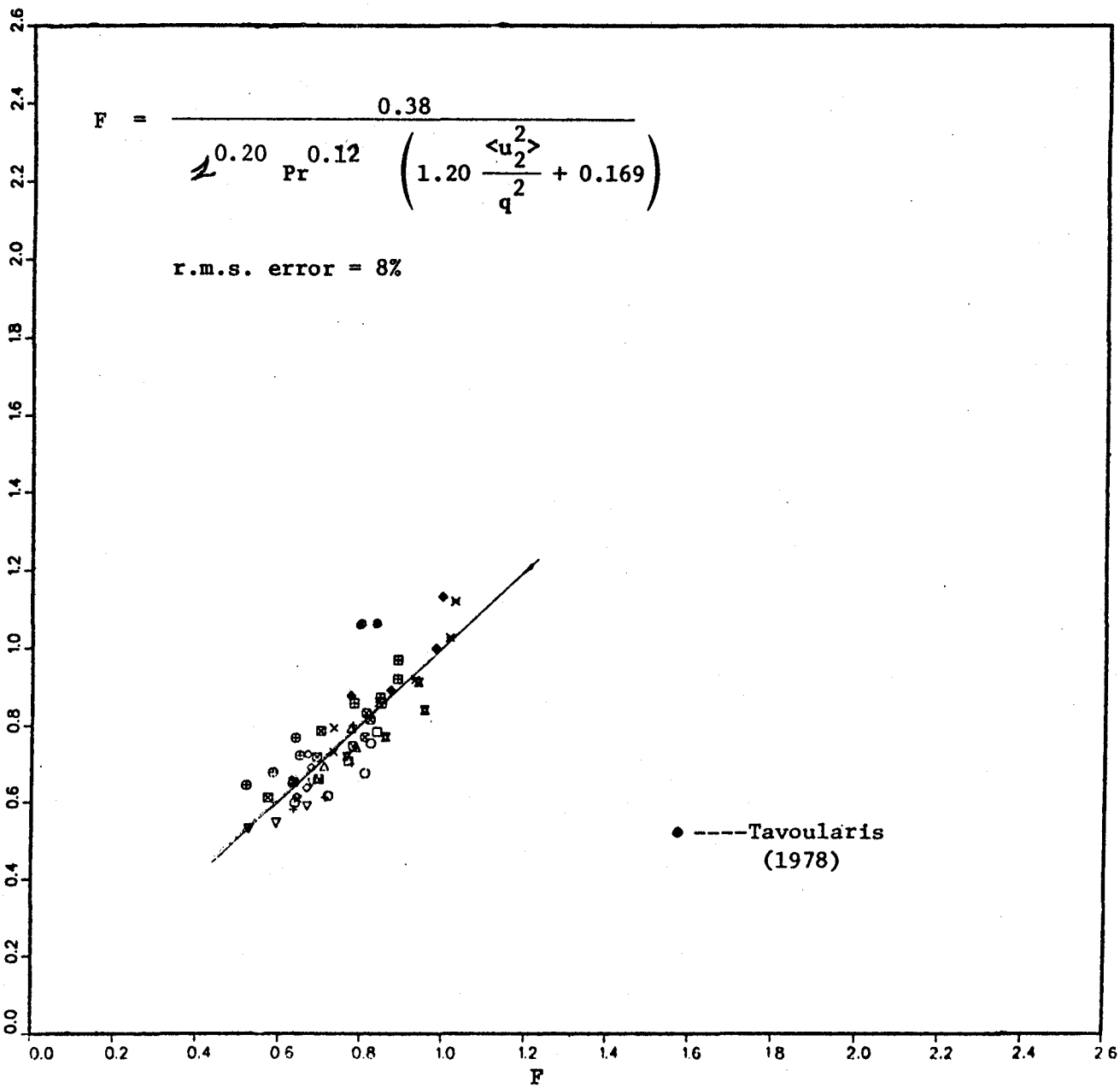

Fig. 6-59. Turbulent Prandtl number as a function of the new model.

Chapter VII

CONCLUSIONS AND RECOMMENDATIONS

7.1 Conclusions

In this work we have numerically solved the three-dimensional, time-dependent equations of motion and the diffusion equation for two cases, homogeneous isotropic turbulence and homogeneous sheared turbulence. In order to do this, we were required to work at rather small Reynolds numbers. The results obtained have been compared with available experimental results, and good agreement was obtained.

For the homogeneous isotropic flows, it has been found that the Reynolds and Prandtl numbers (within the range considered) have strong effects on the decay rates and the length scale ratios. The decay exponent of the turbulent kinetic energy, n, decreases with increasing Reynolds number (from 2.5 at $Re_\lambda = 0$ to 1.2 at $Re_\lambda \sim 25$). The decay exponent of the scalar fluctuation intensity, m, decreases with both Reynolds and Prandtl numbers. Both the decay exponent ratio, R, and the length scale ratio, λ_u/λ_θ, increase with the Reynolds number when $Pr < 1$ and decrease with the Reynolds number when $Pr > 1$. The absolute value of the velocity derivative skewness, Sk, has a maximum value of 0.5 at $Re_\lambda \simeq 20$. Sk is zero at $Re_\lambda = 0$ and reaches an asymptotic value of approximately 0.4 as Re_λ approaches 100.

In homogeneous shear flows, unlike homogeneous isotropic flows, the initial conditions, such as the initial length scale ratio, λ_u/λ_θ, and the initial non-dimensional scalar fluctuation do not affect the scalar field. Many of the turbulence statistics are nearly independent of the Reynolds number. The shear number has the most important influence in this flow. In homogeneous shear flows, the length scales grow faster than in the isotropic flows. The behavior of the dissipation (or transfer) length scale and integral length scales are similar, but the mixing length seems to behave differently. The turbulent kinetic energy first decreases and then increases. Due to the shear, the flow is anisotropic; the streamwise velocity fluctuations are the largest, while the vertical velocity fluctuations are the smallest. The dissipation

tensor is very anisotropic and does not become isotropic even at rather high Reynolds numbers. This is contrary to the assumptions made by many people. The behavior of the scalar fluctuation intensity is very similar to that of the streamwise turbulent kinetic energy components; they are well correlated, and their spectra are similar. It is unclear whether this flow reaches statistical equilibrium. Our results show that $< u_1 u_2 >/q^2$, $< \theta u_1 >/q\theta'$, and $< \theta u_2 >/q\theta'$ are nearly constant in this flow. However, the other components of b_{ij} slightly change with time.

From the three-dimensional spectra of the production, dissipation, pressure-strain, and the transfer terms, it is found that influence of the transfer term is very small compared to that of the other terms. In sheared turbulence, this term, contrary to a common assumption, transfers energy from both large and small eddies to the moderate-sized eddies.

The three-dimensional spectra of the components of pressure field ($p^{(1)}$ and $p^{(2)}$) have been studied. It has been found that the part of pressure which is explicitly associated with the mean flow dominates at the large scales and has a k^{-5} shape at moderate wave numbers. The second part of the pressure is important at the small scales. The relative magnitude of the two parts of the pressure depends on the shear rate.

The turbulent Prandtl number is almost independent of the Reynolds number, and decreases as the molecular Prandtl number increases. A new model for the turbulent Prandtl number seems to correlate the data better than a number of other models.

Several models for various turbulence statistics were tested, and the following conclusions made:

The eddy viscosity model fits the turbulent shear stress quite well, but is incapable of predicting the diagonal components of the Reynolds stress accurately. The parameter in the model is proportional to the inverse of the shear number. Rodi's algebraic model for the Reynolds stress is also incapable of predicting the diagonal components of the Reynolds stress in this flow, but its coefficient is relatively

constant for the turbulent shear stress. Eddy diffusivity models behave similarly to the eddy viscosity model. Their parameters are nearly proportional to the inverse of shear number and depend slightly on Prandtl number.

The Rotta model for the pressure-strain term correlates the data rather well. The modified Rotta model correlates the data even better. The constant for this model is about 2.7. Similarly, the model similar to the modified Rotta model for the pressure-scalar covariance fits the data very well. The models for the fast term are not good and need to be improved.

7.2 Recommendations

In this work, we have assumed the scalar is passive; therefore, we have neglected the effects of buoyancy. It would be interesting to study the effects of buoyancy in these flows. Our simulated flow fields have provided "exact" results for the flow fields. We have used these results to check some of the models for various volume-averaged turbulence statistics. We suggest using the "exact" results to obtain some models for the subgrid scales of the scalar fields.

Finally, it should be possible to extend this work to simulate the reacting flows.

Appendix A

LINEAR STABILITY ANALYSIS

In this section we study the stability and accuracy of numerical methods of solving the equations of motion (2-18) and the diffusion equation (2-20).

For the sake of simplicity, let us assume that the problem is two-dimensional. In two dimensions, the Fourier transform of the linearized equation (2-18) has the form:

$$\frac{\partial \hat{u}_\ell}{\partial t} = - u_{oj} ik_j \hat{u}_\ell + St\, u_{o2} ik_1 \hat{u}_\ell - S\hat{u}_2(k)\, \delta_{\ell 1} - ik_\ell \hat{p} + St\, ik_1 \hat{p} \delta_{\ell 2}$$

$$+ \nu(-k_j k_j + 2St\, k_1 k_2 - S^2 t^2 k_1^2)\, \hat{u}_\ell \qquad \text{(A-1)}$$

where u_{oi} is assumed to be constant. In component form, this becomes:

$$\frac{\partial \hat{u}_1}{\partial t} = \hat{u}_1 \left[(- u_{oj} k_j + St\, u_{o2} k_1)\, i + \nu(-k_j k_j + 2\, St\, k_1 k_2 - S^2 t^2 k_1^2) \right]$$

$$- ik_1 \hat{p} - S\, \hat{u}_2 \qquad \text{(A-2)}$$

$$\frac{\partial \hat{u}_2}{\partial t} = \hat{u}_2 \left[(- u_{oj} k_j + St\, u_{o2} k_1)\, i + \nu(-k_j k_j + 2\, St\, k_1 k_2 - S^2 t^2 k_1^2) \right]$$

$$- ik_2 \hat{p} + St\, ik_1 \hat{p} \qquad \text{(A-3)}$$

Let us define

$$\alpha = (- u_{o1} k_1 - u_{o2} k_2 + St\, u_{o2} k_1)\, i + \nu(-k_1^2 - k_2^2 + 2\, St\, k_1 k_2 - S^2 t^2 k_1^2) \qquad \text{(A-4)}$$

which is simply a known function of the wavenumber. Then the equations (A-2) and (A-3) become

$$\frac{\partial \hat{u}_1}{\partial t} = \hat{u}_1\alpha - ik_1\hat{p} + S\hat{u}_2$$
$$\frac{\partial \hat{u}_2}{\partial t} = \hat{u}_2\alpha - ik_2\hat{p} + St\, k_1\hat{p} \qquad \text{(A-5)}$$

Following the standard linear stability analysis for Navier-Stokes equations, since the dynamics of the pressure is totally dependent on the dynamics of the velocity field, we consider the following equations.

$$\frac{\partial \hat{u}_1}{\partial t} = \alpha\hat{u}_1 + S\hat{u}_2 \qquad \text{(A-6)}$$

$$\frac{\partial \hat{u}_2}{\partial t} = \alpha\hat{u}_2 \qquad \text{(A-7)}$$

The solution of the above equations using the Adams-Bashforth method (2-11) is

$$\hat{u}_2^{n+1} = \hat{u}_2^n + \frac{1}{2}\Delta t(3\alpha\hat{u}_2^n - \alpha\hat{u}_2^{n-1}) + \frac{1}{2}\Delta t\delta_{i1}(3S\hat{u}_2^n - S\hat{u}_2^{n-1}) \qquad \text{(A-8)}$$

Let us assume

$$\hat{u}_2^{n+1} = R\hat{u}_2^n \qquad \text{(A-9)}$$

First let us consider the stability of the $\hat{u}_2$ equation. From (A-9) and (A-8), for $i = 2$, one can get:

$$R = 1 + \frac{1}{2}\Delta t\ 3\alpha - \frac{\alpha}{R} \qquad \text{(A-10)}$$

or

$$R^2 - (1 + \frac{3}{2}\Delta t\alpha)\ R + \frac{\Delta t}{2}\alpha = 0 \qquad \text{(A-11)}$$

or

$$R_{1,2} = \frac{1}{2} - \frac{3\Delta t}{4}\alpha \pm \sqrt{\frac{1}{4} - \frac{9}{16}\Delta t^2\alpha^2 - \alpha\Delta t} \qquad \text{(A-12)}$$

where α is defined in (A-4).

We can write the maximum value of α as

$$\alpha = (iN_C + N_D)/\Delta t \qquad \text{(A-13)}$$

where N_C is the Courant number and is defined as

$$N_C = (|u_j|_{max} k_{j\ max} + St|u_2|_{max} k_{1\ max})\ \Delta t \qquad \text{(A-14)}$$

and N_ν is the viscous stability parameter

$$N_\nu = \left[-k_{j\ max} k_{j\ max} + 2\ St\ k_{1\ max} k_{2\ max} - S^2 t^2 k_{1\ max}^2\right] \nu \Delta t \qquad \text{(A-15)}$$

For our problem the maximum wavenumber is

$$k_{1\ max} = k_{2\ max} = k_{3\ max} = k_{max} = \pi/\Delta$$

where Δ is mesh size. Note that the computational box length is 2π, so $\Delta = 2\pi/(N-1)$, where N is the number of mesh points in each direction. Therefore, k_{max} becomes:

$$k_{max} = \frac{N-1}{2} \qquad \text{(A-16)}$$

From (A-14), (A-15), and (A-16), the values of N_c and N_ν are

$$N_C = \frac{N-1}{2}\left[|u_1|_{max} + (1 + St)|u_2|_{max}\right] \Delta t \qquad \text{(A-17)}$$

and

$$N_\nu = \left(\frac{N-1}{2}\right)^2 \left[-3 + 2\ St - S^2 t^2\right] \nu \Delta t \qquad \text{(A-18)}$$

and are time dependent. (Note that St varies between $-1/2$ and $1/2$).

Following the same procedure, one can set the following N_c and N_ν for the u_1 equation:

$$N_\nu = \nu \Delta t \left[\left(\frac{N-1}{2}\right)^2 (3 - 2\ St - S^2 t^2) + \frac{1}{2} S \left(\frac{u_2}{u_1}\right)_{max}\right] \qquad \text{(A-19)}$$

and N_c is the same as before, Eq. (A-14). The magnitudes of R_1 and R_2 of Eq. (A-12) depend on the magnitudes of N_c and N_ν. R_1 is the physical root and R_2 is the spurious root. It should be noted that the method is stable even if $|R| > 1$, because in shear flows the velocities increase with time. The limit on R is obtained by comparing Eq. (A-9) and the analytical solution of Eqs. (A-6) and (A-7).

The magnitudes of R_1 and R_2 for various N_c and N_ν (Eqs. (A-12) and (A-13)) are given in Table 2-1.

For the diffusion equation (2-20), we follow a similar procedure, and the important parameter governing stability is:

$$N_D = D \frac{(N-1)}{2} (-3 + 2\,St - S^2t^2)\,\Delta t \qquad (A\text{-}20)$$

For the three-dimensional case, the Courant number is defined as

$$N_C = \frac{N-1}{2}\left[|u_1|_{max} + (1 + St)|u_2|_{max} + |u_3|_{max}\right]\Delta t \qquad (A\text{-}21)$$

Stability is affected by St and $S|u_2/u_1|_{max}$, but as we keep $|St| < 0.5$, the effect is small. Also, as we increase S, $|u_2/u_1|$ becomes small and therefore $S|u_2/u_1|_{max}$ is always small compared to the other term in Eq. (A-19).

The time step at which the results are reasonably accurate and stable is chosen by using Table 2-1. We chose $N_c = 0.1$ to 0.3 and $N_\nu = 0.1$. Note that $N_D = N_\nu/Pr$.

Appendix B

COORDINATE TRANSFORMATION

In this section, we consider the coordinate transformation which was used to eliminate the non-periodic terms in the equations of motion and the diffusion equation.

The transformed coordinates are

$$\begin{aligned} x_1 &= X_1 - SX_2T \\ x_2 &= X_2 \\ x_3 &= X_3 \\ t &= T \end{aligned} \qquad \text{(B-1)}$$

where X_1 and T are the physical (laboratory) variables. As shown below, the tranformed coordinate moves with time.

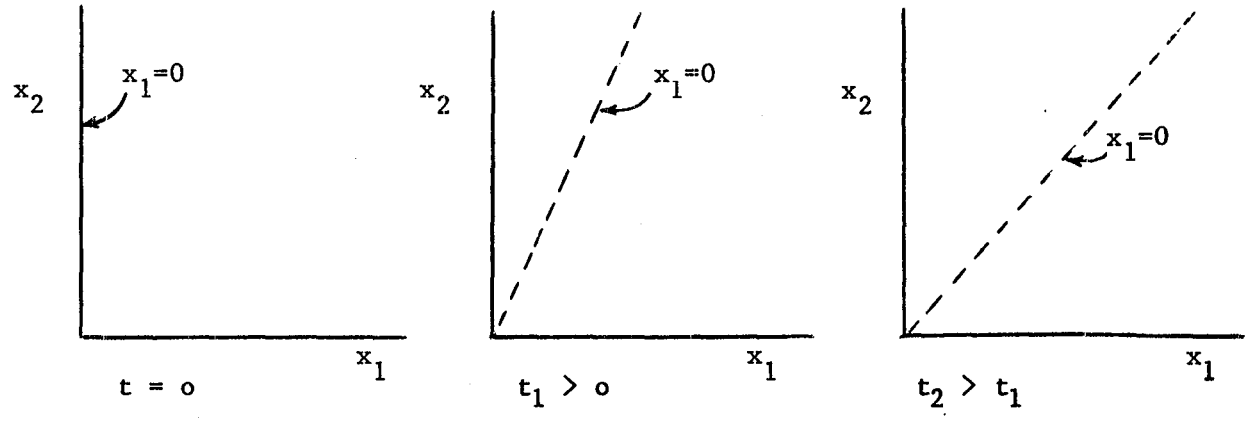

Using the chain rule, the derivative of any function with respect to X_i and T can be obtained as follows:

$$\frac{\partial}{\partial X_1} = \frac{\partial}{\partial x_1} \qquad \text{(B-2)}$$

$$\frac{\partial}{\partial X_2} = \frac{\partial}{\partial x_2} - St\,\frac{\partial}{\partial x_1} \qquad \text{(B-3)}$$

$$\frac{\partial}{\partial X_3} = \frac{\partial}{\partial x_3} \qquad \text{(B-4)}$$

$$\frac{\partial}{\partial T} = \frac{\partial}{\partial t} - Sx_2 \frac{\partial}{\partial x_1} \tag{B-5}$$

$$\frac{\partial^2}{\partial X_1^2} = \frac{\partial^2}{\partial^2 x_1} \tag{B-6}$$

$$\frac{\partial^2}{\partial X_2^2} = \frac{\partial^2}{\partial^2 x_2} - 2\,St\,\frac{\partial^2}{\partial x_1 \partial x_2} + S^2 t^2 \frac{\partial}{\partial x_1^2} \tag{B-7}$$

$$\frac{\partial^2}{\partial X_3^2} = \frac{\partial^2}{\partial^2 x_3} \tag{B-8}$$

The above relations were used to transform the non-periodic equations (Section 2.5b) into Eqs. (2-17) through (2-20).

Appendix C

TABULATED DATA FOR THE SIMULATED FLOW FIELDS

In this appendix, we present a set of tables containing various information, raw data, and turbulence statistics obtained from 24 simulated homogeneous shear flow fields and 56 scalar fields.

The initial values used in all of the simulations are:

Turbulence velocity, $q = 0.600.$

Integral length scale, $L = 0.71.$

Taylor micro-scale, $\lambda = 0.22.$

r.m.s. scalar fluctuations, $\theta' = 0.600.$

Integral length scale of the scalar field, $L_\theta = 0.51.$

Taylor microscale of the scalar field, $\lambda_\theta = 0.17.$

The above parameters are nondimensionalized, as stated in Section 2.3.

The following table shows other parameters used for each simulation.

TABLE C-1

Dimensional Parameters For Each Simulation

Simulation	Shear Rate S	Viscosity ν	Diffusivity D	Mean Scalar Gradient S_2
HS64A	8.851	0.00500	0.00500	8.500
HS64B	8.851	0.01000	0.01000	8.500
HS64G	42.890	0.00500	0.00500	42.500
HS64J	2.860	0.00525	0.00525	2.860
HS64M	1.716	0.00350	0.00350	1.716
HS64O	2.230	0.00175	0.00175	2.230
HS64C	8.851	0.01000	0.00200	8.500
HS64D	8.851	0.00500	0.00100	8.500
HS64E	8.851	0.00500	0.02500	8.500
HS64F	8.851	0.01000	0.05000	8.500
HS64H	42.890	0.00500	0.00100	42.500
HS64I	42.890	0.00500	0.02500	42.500
HS64N	1.716	0.00350	0.01750	1.716
HS64P	2.230	0.00175	0.00875	2.230

TABLE C-2

Components of the Reynolds Stress Tensor

$< u_i \, u_j >$

Simulation	Equation	St=4	St=5	St=6	St=7
HS64A	i=1, j=1	0.27469	0.32620	0.37760	0.42920
	i=2, j=2	0.05271	0.04726	0.04150	0.04369
	i=3, j=3	0.11650	0.13095	0.14270	0.14600
	i=1, j=2	-0.08224	-0.08429	-0.08610	-0.09209
HS64B	i=1, j=1	0.15980	0.17530	0.18870	0.20080
	i=2, j=2	0.03265	0.02558	0.01842	0.01689
	i=3, j=3	0.07240	0.07840	0.08198	0.07798
	i=1, j=2	-0.04889	-0.04524	-0.04150	-0.04038
HS64G	i=1, j=1	0.49410	0.64560	0.80250	0.96740
	i=2, j=2	0.06029	0.05133	0.04100	0.04025
	i=3, j=3	0.17620	0.19430	0.21100	0.21700
	i=1, j=2	-0.12570	-0.13374	-0.13829	-0.14679
HS64J	i=1, j=1	0.07135	0.07475	0.07931	0.08491
	i=2, j=2	0.02326	0.01816	0.01428	0.01361
	i=3, j=3	0.04360	0.04696	0.04753	0.04428
	i=1, j=2	-0.02565	-0.02334	-0.02144	-0.02099
HS64M	i=1, j=1	0.04595	0.04829	0.05160	0.05602
	i=2, j=2	0.01663	0.01380	0.01211	0.01187
	i=3, j=3	0.03022	0.03129	0.03168	0.03097
	i=1, j=2	-0.01708	-0.01592	-0.01512	-0.01535
HS64O	i=1, j=1	0.11160	0.11920	0.12920	0.14100
	i=2, j=2	0.04978	0.04680	0.04717	0.05120
	i=3, j=3	0.07717	0.08100	0.08603	0.09166
	i=1, j=2	-0.04044	-0.04087	-0.04278	-0.04612

TABLE C-3

Dissipation Tensor

Equation (4-7)

Simulation	EQUATION	St=4	St=5	St=6	St=7
HS64A	i=1, j=1	0.43040	0.49920	0.55380	0.60440
	i=2, j=2	0.05560	0.05220	0.05204	0.05352
	i=3, j=3	0.18396	0.18280	0.18514	0.18714
	i=1, j=2	-0.10240	-0.10040	-0.09895	-0.09735
HS64B	i=1, j=1	0.40380	0.41180	0.42000	0.43420
	i=2, j=2	0.04466	0.03322	0.02662	0.02350
	i=3, j=3	0.19286	0.17758	0.16624	0.16634
	i=1, j=2	-0.09403	-0.07925	-0.06819	-0.05889
HS64G	i=1, j=1	0.90380	1.17700	1.44540	1.73120
	i=2, j=2	0.05318	0.04346	0.03804	0.03522
	i=3, j=3	0.35980	0.35300	0.35480	0.35740
	i=1, j=2	-0.17890	-0.18600	-0.19080	-0.19480
HS64J	i=1, j=1	0.07158	0.06688	0.06488	0.06400
	i=2, j=2	0.01742	0.01299	0.01071	0.00953
	i=3, j=3	0.05168	0.04582	0.04146	0.03740
	i=1, j=2	-0.01863	-0.01485	-0.01229	-0.01054
HS64M	i=1, j=1	0.02746	0.02486	0.02398	0.02374
	i=2, j=2	0.00940	0.00680	0.00564	0.00508
	i=3, j=3	0.02304	0.01943	0.01726	0.01545
	i=1, j=2	-0.00725	-0.00568	-0.00465	-0.00401
HS64O	i=1, j=1	0.06126	0.05868	0.05822	0.05858
	i=2, j=2	0.02830	0.02500	0.02374	0.02418
	i=3, j=3	0.05148	0.04666	0.04562	0.04522
	i=1, j=2	-0.01565	-0.01432	-0.01387	-0.01310

TABLE C-4

Pressure-Strain Fast Terms

Equation (4-46)

Simulation	Equation	St=4	St=5	St=6	St=7
HS64A	i =1, j =1	-0.17800	-0.15840	-0.12280	-0.12870
	i =2, j =2	-0.02782	-0.04524	-0.03911	-0.04536
	i =3, j =3	0.20590	0.20370	0.16200	0.13340
	i =1, j =2	0.27786	0.24533	0.16045	0.13980
HS64B	i =1, j =1	-0.12380	-0.10185	-0.06916	-0.06710
	i =2, j =2	-0.01748	-0.03175	-0.02452	0.00236
	i =3, j =3	0.14134	0.13360	0.09368	0.06474
	i =1, j =2	0.20186	0.16937	0.09913	0.07299
HS64G	i =1, j =1	-1.08190	-1.00550	-0.76612	-0.81830
	i =2, j =2	-0.16999	-0.21173	-0.19234	0.06255
	i =3, j =3	1.25190	1.21730	0.95850	0.75580
	i =1, j =2	1.77020	1.61540	1.12534	1.00770
HS64J	i =1, j =1	-0.02569	-0.02006	-0.01378	-0.01316
	i =2, j =2	-0.00394	-0.00732	-0.00458	-0.00070
	i =3, j =3	0.02962	0.02736	0.01835	0.01386
	i =1, j =2	0.04423	0.03468	0.02242	0.01839
HS64M	i =1, j =1	-0.01037	-0.00865	-0.00671	-0.00599
	i =2, j =2	-0.00147	-0.00205	-0.00171	-0.00101
	i =3, j =3	0.01184	0.01070	0.00842	0.00700
	i =1, j =2	0.01707	0.01482	0.01130	0.00960
HS64O	i =1, j =1	-0.03178	-0.03053	-0.03006	-0.03238
	i =2, j =2	-0.00386	-0.00462	-0.00295	-0.00332
	i =3, j =3	0.03565	0.03515	0.03302	0.03570
	i =1, j =2	0.06338	0.05923	0.05570	0.05798

TABLE C-5

Pressure-Strain; Rotta Terms

Equation (4-53)

Simulation	Equation	St=4	St=5	St=6	St=7
HS64A	i=1, j=1	-0.04969	-0.06133	-0.07108	-0.07963
	i=2, j=2	0.03892	0.04890	0.05630	0.06261
	i=3, j=3	0.01073	0.01238	0.01475	0.01699
	i=1, j=2	0.06990	0.08400	0.09830	0.11640
HS64B	i=1, j=1	-0.01629	-0.01727	-0.01722	-0.01736
	i=2, j=2	0.01338	0.01506	0.01543	0.01586
	i=3, j=3	0.00291	0.00221	0.00179	0.00150
	i=1, j=2	0.02320	0.02340	0.02240	0.02330
HS64G	i=1, j=1	-0.03234	-0.04556	-0.05800	-0.06822
	i=2, j=2	0.02912	0.04139	0.05148	0.05567
	i=3, j=3	0.00322	0.00417	0.00651	0.01255
	i=1, j=2	0.05210	0.06800	0.07730	0.08730
HS64J	i=1, j=1	-0.00698	-0.00715	-0.00691	-0.00676
	i=2, j=2	0.00627	0.00688	0.00679	0.00644
	i=3, j=3	0.00072	0.00068	0.00013	0.00013
	i=1, j=2	0.01002	0.00975	0.00992	0.01096
HS64M	i=1, j=1	-0.00348	-0.00369	-0.00378	-0.00396
	i=2, j=2	0.00320	0.00343	0.00373	0.00377
	i=3, j=3	0.00027	0.00025	0.00005	0.00019
	i=1, j=2	0.00587	0.00568	0.00555	0.00620
HS64O	i=1, j=1	-0.01549	-0.01716	-0.02000	-0.02358
	i=2, j=2	0.01393	0.01606	0.01869	0.02144
	i=3, j=3	0.00155	0.0011	0.00130	0.00214
	i=1, j=2	0.03340	0.03152	0.03267	0.03784

TABLE C-6

Scalar Fluctuation Invariance

$<\theta^2>$

Simulation	St=4	St=5	St=6	St=7
HS64A	0.54163	0.60711	0.65946	0.69973
HS64B	0.33816	0.36453	0.37910	0.38215
HS64G	0.97368	1.18150	1.37179	1.55312
HS64J	0.17704	0.18678	0.18985	0.18687
HS64M	0.10957	0.11203	0.11355	0.11522
HS64O	0.27862	0.28854	0.30051	0.31448
HS64C	0.54059	0.58781	0.61802	0.62865
HS64D	0.74447	0.86420	0.97217	1.06741
HS64E	0.25490	0.28871	0.31474	0.32945
HS64F	0.12294	0.13980	0.14577	0.13915
HS64H	1.03400	1.26380	1.47800	1.69150
HS64I	0.76096	0.90115	1.02008	1.12416
HS64N	0.03820	0.04333	0.04716	0.04942
HS64P	0.11670	0.13284	0.14692	0.16191

TABLE C-7

Turbulent Heat Flux

Simulation	I	St=4	St=5	St=6	St=7
HS64A	1	0.3641	0.4099	0.4482	0.4512
	2	0.1688	0.1615	0.1490	0.1457
HS64B	1	0.2138	0.2191	0.2166	0.2036
	2	0.1111	0.0997	0.0836	0.0728
HS64G	1	0.7797	0.9314	1.0448	1.1412
	2	0.2674	0.2698	0.2604	0.2588
HS64J	1	0.1359	0.1376	0.1338	0.1265
	2	0.0625	0.0539	0.0433	0.0371
HS64M	1	0.0775	0.0797	0.0832	0.0823
	2	0.0397	0.0341	0.0292	0.0273
HS64O	1	0.2028	0.2113	0.2238	0.2253
	2	0.0946	0.0905	0.0875	0.0897
HS64C	1	0.3274	0.3388	0.3318	0.3278
	2	0.1254	0.1129	0.0958	0.0848
HS64D	1	0.4534	0.5049	0.5390	0.5818
	2	0.1822	0.1752	0.1627	0.1587
HS64E	1	0.2455	0.2954	0.3438	0.3943
	2	0.1303	0.1246	0.1138	0.1117
HS64F	1	0.1200	0.1357	0.1473	0.1585
	2	0.0766	0.0697	0.0565	0.0487
HS64H	1	0.7394	1.0075	1.2785	1.5583
	2	0.2726	0.2760	0.2676	0.2673
HS64I	1	0.6336	0.8381	1.0363	1.2338
	2	0.2463	0.2451	0.2323	0.2275
HS64N	1	0.0352	0.0408	0.0454	0.0506
	2	0.0281	0.0258	0.0232	0.0223
HS64P	1	0.0887	0.1031	0.1167	0.1324
	2	0.0764	0.0750	0.0741	0.0783

TABLE C-8

Dissipation in the Heat Flux Equations

Equation (4-14)

Simulations	i	St=4	St=5	St=6	St=7
HS64A	1	0.4079	0.4862	0.5546	0.6103
	2	-0.1290	-0.1102	-0.0983	-0.0891
HS64B	1	0.3906	0.4213	0.4421	0.4686
	2	-0.1274	-0.0965	-0.0768	-0.0611
HS64G	1	0.9269	1.2450	1.5495	1.8530
	2	-0.2409	-0.2307	-0.2229	-0.2192
HS64J	1	0.0619	0.0732	0.0661	0.0670
	2	-0.0272	-0.0201	-0.0116	-0.0082
HS64M	1	0.0214	0.0221	0.0227	0.0234
	2	-0.0117	-0.0069	-0.0040	-0.0028
HS64O	1	0.0386	0.0406	0.0431	0.0448
	2	-0.0294	-0.0241	-0.0201	-0.0172
HS64C	1	0.3207	0.3566	0.3829	0.3965
	2	-0.0996	-0.0770	-0.0622	-0.0512
HS64D	1	0.3223	0.4053	0.4426	0.4967
	2	-0.1061	-0.0877	-0.0763	-0.0646
HS64E	1	0.5024	0.5364	0.5924	0.5717
	2	-0.1808	-0.1458	-0.1322	-0.1116
HS64F	1	0.4374	0.4493	0.4537	0.4498
	2	-0.1807	-0.1380	-0.1111	-0.0925
HS64H	1	0.5809	0.7876	0.9889	1.1932
	2	-0.1500	-0.1450	-0.1415	-0.1405
HS64I		2.2700	2.9279	3.5175	4.0632
	2	-0.6073	-0.5607	-0.5225	-0.4965
HS64N	1	0.0264	0.0265	0.0269	0.0280
	2	-0.0192	-0.0137	-0.0106	-0.0092
HS64P	1	0.0645	0.0669	0.0700	0.0737
	2	-0.0571	-0.0489	-0.0431	-0.0407

TABLE C-9

Pressure-Scalar Covariance; Fast Term

Equation (4-60)

Simulation	i	St=4	St=5	St=6	St=7
HS64A	1	-0.5182	-0.4350	-0.2959	-0.2565
	2	0.1842	0.1986	0.1740	0.0768
HS64B	1	-0.3897	-0.3136	-0.1923	-0.1448
	2	0.1414	0.1592	0.1369	0.0597
HS64G	1	-3.2060	-2.8110	-1.9854	-1.7207
	2	1.6390	1.6950	1.5810	0.9050
HS64J	1	-0.0832	-0.0630	-0.0400	-0.0309
	2	0.0227	0.0274	0.0207	0.0096
HS64M	1	-0.0310	-0.0254	-0.0194	-0.0164
	2	0.0078	0.0076	0.0063	0.0042
HS64O	1	-0.1044	-0.0981	-0.0932	-0.0932
	2	0.0188	0.0179	0.0151	0.0145
HS64C	1	-0.3353	-0.2312	-0.1194	-0.0816
	2	0.1297	0.1209	0.0871	0.0333
HS64D	1	-0.5344	-0.4475	-0.3061	-0.2662
	2	0.1938	0.2040	0.1759	0.0751
HS64E	1	-0.4605	-0.3923	-0.2641	-0.2283
	2	0.1501	0.1763	0.1614	0.0741
HS64F	1	-0.3174	-0.2618	-0.1565	-0.1165
	2	0.0966	0.1230	0.1085	0.0442
HS64H	1	-3.2840	-2.8303	-2.0009	-1.7348
	2	1.6716	1.7254	1.6090	0.9296
HS64I	1	-3.1525	-2.7229	-1.9157	-1.6583
	2	1.4977	1.5639	1.4650	0.8042
HS64N	1	-0.0234	-0.0205	-0.0161	-0.0140
	2	0.0055	0.0063	0.0059	0.0042
HS64P	1	-0.0865	-0.0831	-0.0786	-0.0796
	2	0.0155	0.0168	0.0155	0.0144

TABLE C-10

Pressure-Scalar Covariance; Rotta Term

Equation (4-74)

Simulation	i	St=4	St=5	St=6	St=7
HS64A	1	-0.1209	-0.1231	-0.1258	-0.1314
	2	0.1816	0.1936	0.1964	0.2082
HS64B	1	-0.0444	-0.0379	-0.0324	-0.0300
	2	0.0687	0.0635	0.0542	0.0522
HS64G	1	-0.0812	-0.0865	-0.0946	-0.1062
	2	0.1502	0.1664	0.1573	0.1694
HS64J	1	-0.0222	-0.0193	-0.0169	-0.0144
	2	0.0296	0.0281	0.0269	0.0268
HS64M	1	-0.0123	-0.0115	-0.0096	-0.0085
	2	0.0157	0.0158	0.0146	0.0136
HS64O	1	-0.0601	-0.0612	-0.0648	-0.0692
	2	0.0711	0.0696	0.0732	0.0772
HS64C	1	-0.0467	-0.0352	-0.0254	-0.0205
	2	0.0731	0.0590	0.0437	0.0343
HS64D	1	-0.1417	-0.1473	-0.1538	-0.1625
	2	0.2125	0.2303	0.2381	0.2678
HS64E	1	-0.0678	-0.0664	-0.0673	-0.0707
	2	0.0997	0.1010	0.0981	0.1009
HS64F	1	-0.0176	-0.0141	-0.0124	-0.0110
	2	0.0257	0.0217	0.0175	0.0142
HS64H	1	-0.0839	-0.0902	-0.0988	-0.1114
	2	0.1547	0.1727	0.1635	0.1767
HS64I	1	-0.0693	-0.0710	-0.0771	-0.0859
	2	0.1298	0.1383	0.1297	0.1370
HS64N	1	-0.0055	-0.0054	-0.0047	-0.0043
	2	0.0061	0.0065	0.0063	0.0062
HS64P	1	-0.0365	-0.0378	-0.0450	-0.0458
	2	0.0426	0.0425	0.0465	0.0500

References

1. Batchelor, G. K., The Theory of Homogeneous Turbulence, Cambridge University Press (1952).

2. Batchelor, G. K., and Townsend, A. A., "Decay of Turbulence in the Final Period," Proc. Roy. Soc., 194, 527 (1948).

3. Batchelor, G. K., and Stewart, R. W., "Anisotropy of Spectrum of Turbulence at Small Wave Numbers," Quart. F. M. Appl. Math, 3, 1 (1950).

4. Batt, R. G., "Turbulent Mixing of Passive and Chemically Reacting Species in a Low-Speed Shear Layer," J. Fluid Mech., 82, Prt 1, 53-95 (1977).

5. Bennett, J. C., and Corrsin, S., "Decay of Nearly Isotropic, Grid-Generated Turbulence at Small Reynolds Numbers in a Straight Duct and a Slight Contraction," submitted for publication in the Physics of Fluids.

6. Boussinesq, J., "Essai sur la théorie des eaux courants," Mém. Présentés par Divers Savants á l'Acad. des Sciences, 23 (1877).

7. Bracewell, R. Fourier Transform and Its Applications (1965).

8. Bradshaw, P., Ferris, D. H., and Atwell, N. D., J. Fluid Mech., 28, No. 593 (1967).

9. Champagne, F. H., Harris, V. G., and Corrsin, S., "Experiments on Nearly Homogeneous Turbulent Shear Flow," J. Fluid Mech., 41, 81 (1970).

10. Clark, R. A., Ferziger, J. H., and Reynolds, W. C., "Evaluation of Subgrid-Scale Turbulence Models Using a Fully Simulated Turbulent Flow," Report TF-9, Mech. Engrg. Dept., Stanford Univ. (1977). Also, J. Fluid Mech., 91, 1 (1979).

11. Collis, D. C., "The Diffusion Process in Turbulent Flow," Rept. A55, Aero Div., Australian Council Sci. and Indus. Res. (1948).

12. Comte-Bellot, G., and Corrsin, S., "Simple Eulerian Line Correlation of Full- and Narrow-Band Velocity Signals in Grid-Generated 'Isotropic' Turbulence," J. Fluid Mech., 48, 273 (1971).

13. Cooley, J. W., and Tukey, J. W., "An Algorithm for the Machine Calculation of Complex Fourier Series," Math. Comput., 19, 90, 297-301 (1965).

14. Corrsin, S., private communication (1980).

15. Crawford, M. E., and Kays, W. M., "STAN5--A Program for Numerical Computation of Two-Dimensional Internal and Extenal Boundary Layer Flows," NASA CR-2742 (1976).

16. Domis, M. A., "Large Eddy Simulation of a Passive Scalar in Isotropic Turbulence," QMC P 6037, Imperial College, London, England (1979).

17. Feiereisen, W. J., Ph.D. thesis, Mechanical Engrg. Dept., Stanford University (1981).

18. Fox, J., "Turbulent Temperature Fluctuations and Two-Dimensional Heat Transfer in a Uniform Shear Flow," NASA Tech. Note D-2511 (1964).

19. Frenkiel, F. N., "On Turbulent Diffusion," Rep. 1136, 67, Symp. on Turbulence, Naval Ord. Lab (June 1949).

20. Frenkiel, F. N., Klebanoff, P. S., ~~Kuang~~ Hwang, T. T., "Grid Turbulence in Air and Water," Phys. Fluids, 22, No. 9 (Sept. 1979).

21. Harris, V. G., Graham, J. A., and Corrsin, S., "Further Experiments in Nearly Homogeneous Turbulent Shear Flow," J. Fluid Mech., 81, 657 (1977).

22. Herring, R., Orszag, S. A., Krachman, R. H ., and Fox, D. G., "Decay of Two-Dimensional Homogeneous Turbulent Flow," J. Fluid Mech., 66, P3, 417-444 (1974).

23. Hwang, W. S., "Experimental Investigation of Turbulent Shear Flows," Ph.D. dissertation, Univ. of Virginia (1971).

24. Johnson, D. S., "Velocity and Temperature Fluctuation Measurements in a Turbulent Boundary Layer Downstream of a Stepwise Discontinuity in Wall Temperature," J. Applied Mechanics, Sept. 1959, 325-336.

25. Kármán, T. von, "The Fundamentals of the Statistical Theory of Turbulence," J. Aero. Sci., 4, 131 (1937).

26. Kármán, T. von, and Howarth, L., "On the Statistical Theory of Isotropic Turbulence," Proc. Roy. Soc. London A, 164, 192 (1938).

27. Kistler, A. L., O'Brien, V., and Corrsin, S., "Double and Triple Correlations Behind a Heated Grid," J. Aeronaut. Sci., 23, 96 (1956).

28. Klebanoff, P. S., "Characteristics of Turbulence in a Boundary Layer with Zero Pressure Gradient," NACA Report 1247 (1955).

29. Kolmogoroff, A. N., "Energy Dissipation in Locally Isotropic Turbulence," Duklady AN SSSR, 32 (1), 19 (1941).

30. Kreiss, H. O., and Oliger, S., "Methods for Approximate Solution of Time-Dependent Problems," GARP Publications, Series No. 10, WMO, Geneva (1973).

31. Kwak, D., Reynolds, W. C., and Ferziger, J. H., "Three-Dimensional Time-Dependent Computation of Turbulent Flows," Report No. TF-5, Mech. Engrg. Dept., Stanford Univ. (1975).

32. Lee, D. A., "Spectrum of Homogeneous Turbulence in the Final Stage of Decay," Phys. of Fluids, 8, 1911 (1965).

33. Libby, P. A., "Duffusion of Heat Downstream of a Turbulence Grid," Acta Astronautica, 2, 867-878 (1975).

34. Lilley, D. K., "On the Computational Stability of Numerical Solutions of Time-Dependent Nonlinear Geophysical Fluid Dynamics Problems," Monthly Weather Review, 93, No. 1, 11-26 (1965).

35. Lomax, H., "An Operational Unification of the Finite Difference Method for the Numerical Integration of Ordinary Differential Equations," NAS TR-R-262 (1967).

36. Lumley, J. L., "Computational Modeling of Turbulent Flows," Advances in Appl. Mech., 18, 123-176 (1978).

37. Lumley, J. L., and Khajeh-Nouri, B., "Modeling Homogeneous Deformation of Turbulence" (1974). Unpublished; superseded by Lumley (1975).

38. Mansour, N. N., Moin, P., Reynolds, W. C., and Ferziger, J. H., "Improved Methods for Large Eddy Simulation of Turbulence," Proc. Symp. on Turbulent Shear Flows, Penn. State Univ. (1977).

39. Mills, R. R., and Corrsin, S., "Effect of Contraction on Turbulence and Temperature Fluctuations Generated by a Warm Grid," NASA Memo 5-5-59W (1959).

40. Moin, P., private communication (1981).

41. Mulhearn, P. J., and Luxton, R. E., "The Development of Turbulence Structure in a Uniform Shear Flow," J. Fluid Mech., 68, 577 (1975).

42. Orszag, S. A., and Patterson, G. S., "Numerical Simulation of Three-Dimensional Homogeneous Isotropic Turbulence," Phys. Rev. Lett., 28, Part 2, 76 (1972).

43. Poisson, S. D., Mémoire sur les équations générales de l'équilibre et du mouvement des corps solides elastiques et des fluides, Journal de l'Ecole Polytechnique, 13 (1831).

44. Prandtl, I., "Bericht über Untersuchungen zur ausgebildeten Turbulenz, "Zs. angew. Math. Mech., 5, 136 (1925).

45. Reis, F. B., "Studies of Correlation and Spectra in Homogeneous Turbulence," Ph.D. dissertation, MIT, Cambridge, Mass. (1952).

46. Reynolds, A. J., "The Prediction of Turbulent Prandtl and Schmidt Numbers," Int. J. Heat Mass Transfer," 18, 1055-1069 (1974).

47. Reynolds, O., "An Experimental Investigation of the Circumstances Which Determine Whether the Motion of Water Should Be Direct or Sinuous and of the Law of Resistance in Parallel Channels," Phil. Trans. Roy. Soc., London, 174, 935 (1883).

48. Reynolds, W. C., "Computation of Turbulent Flows," Ann. Rev. Fluid Mech., 8, 183-208 (1976).

49. Rodi, W., "A New Algebraic Relation for Calculating the Reynolds Shear Strsses," Mechanics of Fluids, SAMM 56, T-219-T-221 (1976).

50. Rogallo, R. S., "An ILLIAC Program for the Numerical Simulation of Homogeneous Incompressible Turbulence," NASA TM-73, 203 (1977).

51. Rogallo, R. S., private communication (1981).

52. Rose, W. G., "Results of an Attempt to Generate a Homoteneous Turbulent Shear Flow," J. Fluid Mech., 25, 97 (1966).

53. Rose, W. G., "Interaction of Grid Turbulence with a Uniform Mean Shear," J. Fluid Mech., 44, 767 (1970).

54. Saint-Venant, B. de, "Note á joindre au Mémoire sur la dynamique des fluides," Comptes Rendus des Séances de l'Academie des Sciences, 17 (1843).

55. Schubauer, G. B., "A Turbulence Indicator Utilizing the Diffusion of Heat," NACA Rep. 524 (1935).

56. Schumann, U., and Patterson, G. S., "Numerical Study of Pressure and Velocity Fluctuations in Nearly Isotropic Turbulence," J. Fluid Mech., (1975).

57. Sepri, P., "Two-Point Turbulence Measurements Downstream of a Heated Grid," Phys. of Fluid, 19, 1876-1884 (1976).

58. Shaanan, S., Ferziger, J. H., and Reynolds, W. C., "Numerical Simulation of Turbulence in the Presence of Shear," Rep. No. TF-6, Mech. Engrg. Dept., Stanford Univ. (1975).

59. Schlien, D. J., and Corrsin, S., "A Measurement of Lagrangian Velocity Autocorrelation in Approximately Isotropic Turbulence," J. Fluid Mech., 62, 255 (1974).

60. Simmons, L. F. G., and Salter, C. "Experimental Investigation and Analysis of the Velocity Variations in Turbulent Flow," Proc. Roy. Soc., London A, 145, 212 (1934).

61. Stokes, G. G., "On the Theories of the Internal Friction of Fluids in Motion, and of the Equilibrium and Motion of Elastic Solids," Trans. Cambridge Philos. Soc., 8 (1845).

62. Tan, H. S., and Ling, S. C., "Final Stage Decay of Grid-Product Turbulence," Phys. Fluids, 6 (12), (1963).

63. Tavoularis, S., "Experiments in Turbulent Transport and Mixing," Ph.D. dissertation, Johns Hopkins Univ. (1978).

64. Tavoularis, S., Bennett, J. C., Corrsin, S., "Velocity-Derivative Skewness in Small Reynolds Number in Nearly Isotropic Turbulent Flow," J. Fluid Mech., 88, Part 1, 63-69 (1978).

65. Townsend, A. A., "The Structure of the Turbulent Boundary Layer," Proc. Cambridge Phil. Soc., 47, 375 (1951).

66. Uberoi, M. S., and Corrsin, S., "Diffusion of Heat from a Line Source in Isotropic Turbulence," NACA Tech. Note 2710; also NACA Rep. 1142 (1952).

67. Venkataramani, K. S., and Chevray, R., paper submitted for publication (1977).

68. Warhaft, Z., and Lumley, J. L., "Study of the Decay of Temperature Fluctuations in Grid-Generated Turbulence," J. Fluid Mech., 88, Pt. 4, 659-684 (1978).

69. Wassel, A. T., and Catton, I., "Calculation of Turbulent Boundary Layers over Flat Plates with Different Phenomenological Theories of Turbulence and Variable Turbulent Prandtl Number," Int. J. Heat Mass Transfer, 16, 1547-1563 (1973).

70. Wilcox, D. C., and Rubesin, M. W., "Progress in Turbulence Modeling for Complex Flow Fields, Including Effects of Compressibility," NASA Technical Paper 1517, April, 1980.

71. Wiskind, H. K., "A Uniform Gradient Turbulent Transport Experiment," J. Geo. Res., 67, 3033 (1962).

72. Yeh, I. I., and Van Atta, C. W., "Spectral Transfer of Scalar and Velocity Fields in Heated-Grid Turbulence," J. Fluid Mech., 58, 233 (1973).

End of Document